HAL
open science

Misfit dislocation and strain relaxation at large lattice mismatched III-V semiconductor interfaces

Y. Wang

To cite this version:

Y. Wang. Misfit dislocation and strain relaxation at large lattice mismatched III-V semiconductor interfaces. Materials Science [cond-mat.mtrl-sci]. Université de Caen, 2012. English. NNT : . tel-00779457

HAL Id: tel-00779457

https://theses.hal.science/tel-00779457v1

Submitted on 22 Jan 2013

HAL is a multi-disciplinary open access archive for the deposit and dissemination of scientific research documents, whether they are published or not. The documents may come from teaching and research institutions in France or abroad, or from public or private research centers.

L'archive ouverte pluridisciplinaire **HAL**, est destinée au dépôt et à la diffusion de documents scientifiques de niveau recherche, publiés ou non, émanant des établissements d'enseignement et de recherche français ou étrangers, des laboratoires publics ou privés.

UNIVERSITE DE CAEN /BASSE-NORMANDIE

U.F.R.: Sciences

ECOLE DOCTORALE: SIMEM

THESE

Présentée par

M. Yi WANG

Et soutenue le 20 juin 2012

En vue de l'obtention du

DOCTORAT de L'UNIVERISTE DE CAEN

Spécialité: Milieux denses, matériaux et composants

(Arrêté du 07 août 2006)

Titre :

Dislocation et relaxation des contraintes aux interfaces entre semiconducteurs III-V à large différence de paramètres de maille

MEMBRES du JURY

M. Eric Tournié	Professeur, Université de Montpellier II	Rapporteur
M. Martin Hÿtch	Directeur de Recherche CNRS, CEMES, Toulouse	Rapporteur
M. Ludovic Desplanque	Maître de conférences, Université de Lille I	
M. Slawomir Kret	Chercheur, Institut de Physique, Varsovie, Pologne	
M. Richard Rizk	Directeur de Recherche CNRS, CIMAP, Caen	
M. Jun Chen	Maître de conférences, Université de Caen	Co-dicteur de thèse
M. Pierre Ruterana	Directeur de Recherche CNRS, CIMAP	Dicteur de thèse

Acknowledgements

Along these three years in CIMAP, I have come across a number of people who gave me support, help, and inspiration. It is impossible to mention everyone and I therefore would like to start by thanking all of you for contributing to my thesis.

However, I would like to mention my supervisor **Dr. Pierre Ruterana** for giving me the opportunity to carry out my PhD Research work in the scope of the ANR project MOS35 and for leading me into the field of electron microscopy and dislocations. Along these three years, he has given me guidance, support, and encouragements for my research, and helped to keep my curiosity always alert; **Dr. Jun Chen**, my co-supervisor for teaching me molecular dynamics and ab initio simulations, and also for the numerous and fruitful discussions.

Indeed, I'd like to thank **Dr. Slawomir Kret** for teaching me strain mapping analysis by GPA and hosting me for experiments with his Titan microscope. I have always enjoyed the visits to IFPAN and hope that we can continue such a fruitful collaboration.

Of course, I owe very much to our MOS35 project partner, the MBE growth group of IEMN Lille: **Dr. Ludovic Desplanque**, **Selim El Kazzi**, and **Dr. Xavier Wallart** for providing me with samples as well as for all the interesting discussions during and outside the project meetings.

I am highly grateful to **Prof. Eric Tournié, Dr. Martin Hÿtch,** for having reviewed this manuscript and allowed me to present my results in front of the PhD examination committee. Thank you also **Dr. Ludovic Desplanque, Dr. Slawomir Kret,** and **Dr. Richard Rizk** for kindly having accepted to take part in the committee of my examination.

My colleagues, **Marie-Pierre Chauvat** for teaching and helping me with sample preparation; **Dr. Bertrand Lacroix**, **Arantxa Vilalta-Clemente** and **Geeta Rani Mutta** for all the good discussions in research and life.

And all my friends in Caen for making my life colorful all along these years.

My wife, Yi JIANG, and my parents, for endless love and support.

Dislocation et relaxation des contraintes aux interfaces entre semiconducteurs III-V à large différence de paramètres de maille

Les semiconducteurs III-V antimoniés suscitent un intérêt grandissant pour les applications en électronique rapide et pour les faibles consommations. Ces matériaux de paramètre de maille supérieur à 6.1 Å se caractérisent par des mobilités élevées et offrent une souplesse inégalée pour l'ingénierie des bandes. Ils ont une large plage de la bande d'énergies qui peut être ajustée dans une gamme de longueur d'onde du proche infrarouge (AlSb, 0.78 µm) à l'infrarouge lointain (InAsSb, 12 µm). Leurs hétérostructures peuvent présenter des alignement des bandes de type I (la bande interdite de plus faible largeur est inclue dans cellede plus grande largeur), alignement de type II (alignement en escalier), et alignement de type III (alignement continu sur l'une des bandes (conduction ou valence) répercutant l'intégralité de l'écart de largeur de bande interdite sur l'autre bande). Outre la structure de bande unique, les propriétés physiques, en particulier la mobilité des porteurs, constituent la distinction entre les antimoniures et les autres semiconducteurs III-V. GaSb est particulièrement intéressant en tant que couche de tampon pour la croissance des autres III-V composés de la famille 6.1 Å.

Toutefois, la croissance des III-V antimoniés sur des substrats disponibles dans le commerce (Si, GaAs, et GaP) posent des problèmes à cause des larges désaccords de paramètres de maille, différence des coefficients de dilatation thermique ainsi que des changements dans la structure chimique et polaire / non polaire décalage (sur substrat Si) à l'interface. En raison de ces problèmes d'incompatibilité, les tentatives pour déposer III-V antimoniés directement sur la GaAs (ou Si ou GaP) conduisent à des couches avec de fortes densités de dislocations émergeantes de l'ordre de 10^{-9}-10^{10} cm^{-2}. Ces dislocations peuvent se propager à la couche active et entraver considérablement la fiabilité des dispositifs.

En général, dans les hétéro-structures de structure cubique, deux types des dislocations d'interface: les dislocations à 90° et les dislocations à $60^{o,}$ peuvent se former aux interfaces. Les dislocations à 90° sont aussi appelées 'dislocations de Lomer' du fait qu'elles jouent un rôle de barrière dans les plans {111} à cause de leur nature sessile. Les dislocations à 60° sont caractérisées par leur vecteur de Burgers incliné par rapport à l'interface avec un angle de 60° avec la ligne de dislocation; elles sont glissiles dans un des plans {111}. Les dislocations à 60° qui se propagent dans le volume, dislocation émergentes, sont aussi appelées 'threading dislocations'. Récemment, il a été proposé que des conditions particulières de croissance pourraient conduire à une formation exclusive des dislocations de Lomer aux hétérointerfaces. Un tel réseau hautement périodique des dislocations de Lomer dans la croissance de GaSb sur GaAs donnerait alors des couches très relaxées (~ 98%) avec une très faible densité de dislocations émergentes ($\sim 10^5$ cm^{-2}). L'objectif scientifique de ce travail a été d'abord de comprendre les problèmes de croissance associés à la différence des paramètres cristallins, le mécanisme de formation des dislocations d'interface dans les hétéro-structures semiconducteurs, et finalement cerner les condition pour obtenir une bonne qualité des couches épitaxiale de GaSb. Le manuscrit est divisé en cinq chapitres :

Chapitre 1 Semiconducteurs III-V antimoniés

Dan le premier chapitre nous donnons une introduction sur les propriétés des semiconducteurs III-V antimoniés, leur avantages et applications. Puis, nous présentons les problèmes associés à leur croissance, et un résumé de l'art sur leur croissance.

Chapitre 2 Des outils

Dans une première partie, nous avons décrit la technique de croissance (Molecular Beam Epitaxy) qui a été employées par nos collaborateurs (IEMN, Lille) pour réaliser toutes les couches que nous avons analysées dans ce travail. La deuxième partie de ce chapitre est dédiée à la description du principe de microscope électronique en transmission et la préparation des lames minces. L'état de l'art de la microscopie haute résolution avec correction l'aberration sphérique et l'aberration chromatique (C_s et C_c) est discutée. Puis, nous introduisons les différents modes de fonctionnement du microscope utilisés dans

ce travail. Sont ensuite introduits deux de méthodes de traitement d'images : l'analyse de phase géométrique et le tenseur densité dislocation, pour l'analyse des contraintes et la détermination des vecteurs de Burgers des dislocations, respectivement. Finalement, nous rappelons des notion de la théorie de l'élasticité appliquée aux dislocations et leur interaction élastique; et la modélisation par dynamique moléculaire utilisant le potentiel empirique de Stillinger-Weber est au aussi introduite.

Chapitre 3 L'optimisation de la croissance de GaSb sur GaAs et GaP

Dan ce chapitre, nous avons fait une étude systématique de la relation entre les paramètres de croissance et les dislocations d'interface est présentée. Pour ce faire, nous avons d'abord réalisé des couches de GaSb sur le substrat de GaAs en utilisant de fines intercouches d'AlSb d'épaisseur variable pour étudier leur effets sur la densité de dislocation émergentes, les dislocations d'interface, et la relaxation des contraintes. Outre l'intercouche AlSb, l'influence de la reconstruction de la surface du substrat a été également étudiée. Sur substrat GaP, nous avons analysé la relaxation des contraintes, les dislocations d'interface à l'étape initiale de croissance, ainsi que l'optimisation de la croissance. Outre le rôle du traitement de surface du substrat et l'influence de la vitesse de croissance, la température de croissance sur la relaxation des contraintes d'îlôts de GaSb a été aussi étudiée. En utilisant les condition de croissances optimisées, des hétérostructures AlSb/InAs a été fabriquée sur les substrats GaAs et GaP avec une couche tampon de 600 nm de GaSb conduisant à de très bonnes propriétés de transport.

Chapitre 4 Le mécanisme de formation de la dislocation d'interface

Dans ce chapitre, nous avons procédé à une étude extensive de la croissance de GaSb sur GaAs, les paramètres étudiés ont été la reconstructions de surface du substrat, les traitement chimique et la température de croissance (460°C- 530°C). Dans les conditions de croissance utilisées, bien que la relaxation des contraintes soit maximisée à 510°C, le mode de croissance correspondant est trois dimensions (3D), et jusqu'à 40-50 monocouches, la coalescence de film n'est pas encore terminée. Nous avons alors proposé un modèle de relaxation capable de rendre compte de la formation de dislocation d'interface dans les hétéro-structures indépendamment de la différence des paramètres. En plus de

HRTEM, la microscopie électronique en transmission à balayage en mode champ sombre annulaire à grand angle (HAADF-STEM) et la simulation de dynamique moléculaire ont été appliquées pour déterminer la configuration atomique de dislocation d'interface. L'analyse de tenseur densité de dislocation a été ensuite utilisée pour quantifier le vecteur de Burgers des dislocations. Cette mesure précise confirme le mécanisme de formation des dislocations d'interface à GaSb/GaAs interface, qui est en accord avec le modèle que nous avons proposé.

Chapitre 4 Conclusions et Perspectives

Dans le dernier chapitre, nous résumons les conclusions de ce travail et proposons des suggestions pour poursuivre ce type de travail. Dans le cadre de projet MOS35, ce travail a participé à comprendre la formation des dislocations d'interface, et ouvert la voie pour croitre des couches GaSb de qualité électronique vers la fabrication de dispositifs performants.

En résume, les principaux résultats obtenus sont les suivants :

1. Nous avons démontré que le traitement de surface riche en Sb favorise la formation des dislocations de Lomer aux interfaces GaSb/GaAs, et GaSb/GaP.

2. Les couches ultrafines d'AlSb améliore la qualité des interfaces qui deviennent très planes. La combinaison du traitement de substrat riche-Sb et 4 monocouches d'AlSb a conduit à une relaxation mesurée de 100% de la contrainte dans les couches de GaSb sur GaAs et à densité de dislocations émergentes de 10^7 cm^{-2}.

3. L'analyse de la relaxation des contraintes et de l'espacement des dislocations d'interface en fonction de la température et la vitesse de croissance, prédit une fenêtre optimale pour la croissance de couches de GaSb/ GaP avec une relaxation de l'ordre de 95% de la contrainte.

4. Avec ces paramètres optimisés, des hétéro-structures de AlSb/InAs à haute mobilité de 30000 $cm^2V^{-1}s^{-1}$ (25500 $cm^2V^{-1}s^{-1}$) à température ambiante sur GaAs (GaP) ont été obtenues après une couche tampon GaSb de 600nm d'épaisseur.

5. Nous avons mis en évidence qu'un mode de croissance 2D conduit à la formation de dislocation de Lomer, tandis le mode 3D résulte en une formation systématique de paires de dislocations 60° aux interfaces.

6. La configuration atomique des dislocations a été étudiée par HAADF avec une résolution atomique et simulation de l'image. Les cœurs arsenic shuffle de dislocations Lomer se constituent la plus forte densité de dislocation d'interface en accord avec nos simulations numériques.

7. L'analyse du tenseur densité de dislocations montre que dans l'interface GaSb/GaAs, le mécanisme dominant pour la formation des dislocations d'interface est le glissement et la réaction des dislocations à 60°.

Suggestions pour poursuivre ce travail :

1. Une étude approfondie de l'effet de la reconstruction de surface sur la relaxation des contraintes et le mode de croissance est encore nécessaire.

2. Une deuxième préoccupation est la source des dislocations émergentes. Il sera important de comprendre comment la dislocation d'interface se transforme en dislocation émergente.

3. Théoriquement, deux types de dislocations de Lomer sont à l'interface: les configurations "shuffle" devraient se former dans l'interface (1-10) et les "glide" dans (110). Toutefois, dans l'observation expérimentale, à la fois, les configurations "shuffle" et "glide" ont été observées à l'interface (1-10). Il donc sera intéressant de déterminer les raisons de cet écart entre l'observation expérimentale et la modélisation.

Introduction

The misfit dislocations play a critical role in growth of high quality Sb-based III-V hetero-structures, which is of great interest for applications in the near- and far-infrared optoelectronics and ultra-high speed low-power consumption electronics. Due to the large lattice mismatch between the III-Sb and the substrate, large number of defects generate in the epitaxial layer. For instance, the threading dislocations originated in the hetero-interface could propagate to the surface (or active layer) thus damaging the devices. Given the large lattice mismatch, the misfit dislocations form rapidly during the growth. Both 90° Lomer and 60° dislocations are known to form at the interface, and the 60° dislocations are considered as the source of the threading dislocations. Recently, it was reported that one may find growth conditions to form a pure periodical Lomer dislocation network which releases all the misfit strain in the interface thereby obtaining high quality Antimonide based III-V semiconductors.

The aim of this work was to carry out an extensive TEM investigation of Sb-based III-V layer on the GaAs (or GaP) substrates and especially try to point out the relationship between the misfit dislocations types, strain relaxation, and the misfit dislocation formation mechanism.

In Chapter 1, the motivation for this research, the advantage of Sb based III-V semiconductors and the state of art of the MBE epitaxy of GaSb are presented.

The facilities as well as the theoretical tools used in this thesis are introduced in Chapter 2.

The Chapter 3 is an account of our growth optimization of highly lattice mismatched GaSb on two substrates (GaAs and GaP). The epitaxy of GaSb on GaAs substrate with 7.8% lattice mismatch, the influence of the surface treatment and AlSb interlayer thickness on the threading dislocation density, the fine structure of misfit dislocations, and the strain relaxation at the interface region was investigated. The epitaxy of GaSb on GaP substrate with 11.8% lattice mismatch, the strain relaxation and misfit dislocations at initial growth step (10 MLs GaSb) were studied versus substrate surface treatment, growth

rate, and growth temperature. This optimization process predicted an optimal window for the growth relaxed GaSb epitaxial layers on GaP.

Chapter 4 discusses our experimental and theoretical work to investigate the misfit dislocation formation mechanism. With typical (1x4) substrate surface reconstruction, a growth mode transition from 2D to 3D when the growth temperature increasing from 465°C to 510°C was observed. Most interestingly, a dependence of the misfit dislocation configuration was noticed. Based on the conventional 60° dislocation glide model, a misfit dislocation formation model was proposed. This model indicates that the misfit dislocation configurations are determined by the initial growth mode. Moreover, this developed 60° dislocation glide model is able to account for the formation of Lomer, 60°, and 60° dislocation pairs at binary zinc-blende hetero-interfaces for low as well as high lattice mismatch. Then with atomic resolution HAADF along with molecular dynamic simulation, the core structures of the misfit dislocations and their energetic stability were determined. In addition, dislocation density tensor analysis was applied on the identified misfit dislocations to quantify their Burgers vector. This precise method confirms the formation mechanism of the misfit dislocations which is in good agreement with misfit dislocation formation model we proposed.

Finally, we summarize the general conclusion of this work as well as the open questions in Chapter 5.

Contents

Acknowledgments i

Introduction ii

Contents iv

Chapter 1 Antimony based III-V semiconductors 1

1.1 Antimony based compound semiconductor 1

1.2 Why ABCS 1

1.3 Overview of the Sb-based III-V semiconductors technology 5

1.4 Objective of this work 12

References 12

Chapter 2 Tools and facilities 16

2. 1 Molecular beam epitaxy 16

2.1.1 Introduction of the molecular beam epitaxy system 16

2.1.2 Specific growth 17

2.2 Microscopy 18

2.2.1 Principle 18

2.2.2 TEM sample preparation 23

2.3 Modes of operation and theoretical background 23

2.3.1 Diffraction 23

2.3.2 Bright, dark and weak beam images 25

2.3.3 HRTEM 27

2.3.4 Z-contrast imaging or STEM 31

2.4 Geometrical phase analysis and dislocation density tensor 34

2.5 A summary of the theory of simple dislocations 38

2.5.1 Dislocations: edge and screw configurations 38

2.5.2 Burgers vector 39

2.5.3 The stress field of a straight dislocation 40

2.5.4 The strain energy of a dislocation 42

2.5.5 Elastic interaction between dislocation 44

2.6 The Molecular dynamics simulation 45

References 47

Chapter 3 The growth optimization of GaSb on GaAs and GaP substrates 50

3.1Threading dislocation density and strain relief in GaSb/GaAs versus substrate treatment and AlSb thickness 51

3.1.1 Introduction 51

3.1.2 Samples 52

3.1.3 Results 53

3.1.4 Discussion 62

3.2 Strain relief and growth optimization of GaSb on (001) GaP 63

3.2.1 Introduction 63

3.2.2 Samples 64

3.2.3 Surface treatment 65

3.2.4 Optimization of the growth rate and growth temperature 68

3.2.5 The threading dislocation density and strain relaxation in the GaSb buffer layer 70

3.3 The AlSb/InAs hertero-structure on the relaxed buffer layer 71

3.4 Conclusion 73

References 74

Chapter 4 The formation mechanism of misfit dislocations 76

4.1 Introduction 76

4.2 Growth mode dependence of misfit dislocation types and misfit dislocation formation model 78

4.2.1 Samples 78

4.2.2 Misfit dislocation types versus growth mode 79

4.2.3 Misfit dislocation formation model 82

4.3 The atomic configuration of the misfit dislocations 87

4.3.1 Samples 87

4.3.2 The atomic configuration of misfit dislocation 88

4.3.3 The configuration stability of the misfit dislocation 90

4.3.4 The Burgers vector of the misfit dislocations and their formation mechanism 92

4.4 Conclusion 96

References 96

Chapter 5 General conclusions and Perspectives 99

5.1 Conclusions 99

5.2 Perspectives 100

References 104

Appendix I 105

Chapter 1

Antimony based III-V semiconductors

1.1 Antimony based compound semiconductor

In recent years, the narrow band gap antimony based compound semiconductors (ABCS) have been widely investigated as the first candidate materials for fabrication of the third generation infrared photon detectors and integrated circuits with ultra-high speed and ultra-low power consumption [1, 2]. Their applications shall include high-speed analog and digital systems for data processing, communication, imaging, and sensing, particularly in portable equipment such as handheld devices and satellites. The development of Sb-based transistors for use in low-noise high-frequency amplifiers, digital circuits, and mixed-signal circuits may provide the technology needed to address these rapidly expanding needs [2]. Generally, the ABCS refers to the Sb based binary, ternary and quaternary compound semiconductor materials, which consist of III-group elements (Ga, In, Al), Sb, and other V-group elements; such as GaSb, AlSb, InSb, AlGaSb, InAsSb, AlGaAsSb, InGaAsSb and so on. Among them, GaSb and AlSb together with InAs have been routinely called the "6.1 Å III-V family materials" in the literature due to their lattice constant of around 6.1 Å [3]. Like other compound semiconductors, they are of interest principally for their hetero-structures. GaSb is particularly interesting as an important template layer for device growth of other 6.1 Å lattice constant family of compounds.

1.2 Why ABCS?

As shown in Fig. 1.1, band gaps of ABCS can be adjusted in a wide range from near-infrared wavelength (AlSb, 0.78 μm) to far-infrared spectra regions (InAsSb, 12 μm). Their hetero-junctions can have straddling gaps (type-I), staggered gaps (type-II), and broken gaps (type III) [4, 5], as schematically

shown in Fig. 1.2. In a Type-I hetero-junction, one material has both lower conduction band (E_c) and higher valence band (E_v) and naturally, it must have a smaller energy gap, in which electrons and holes are confined in one type of the constituent semiconductor layer with ground electron state belonging to the direct-gap Γ minimum of the conduction band. In a Type-II hetero-junction, the locations of lower E_c and higher E_v are displaced, so the electrons being collected at lower E_c and the holes being collected at

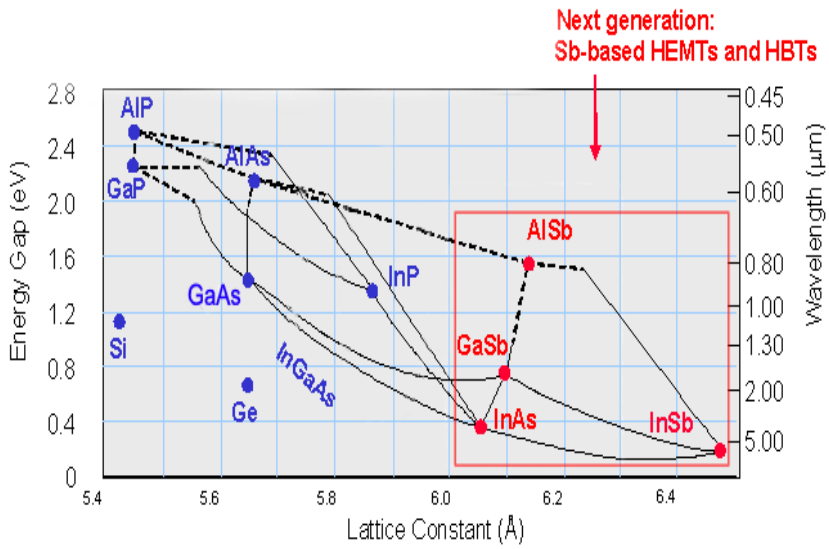

Figure 1. 1 Energy band gap and wavelength versus lattice constant [1].

higher E_v are separated in the real space and confined in the layers of different semiconductors with the ground electron state belonging to (a) the indirect-gap (X or L) minimums of the conduction band or the direct-gap Γ minimum of the conduction band. A Type-III hetero-junction is a special case of Type-II, but the E_c of one side is lower than the E_v of the other. The conduction band thus overlaps the valence band at the interface, hence the name broken gap. Their variant groups of the band alignments lead to many interesting device structures which can be exploited using various combinations of these materials and their band alignments [6]. For instance, the InAs/AlSb quantum wells with type II band alignment for high mobility transistor applications [7, 8]; hetero-structures consisting of InAs contact layer, AlSb barriers, and InAs well for resonant tunneling diodes [9], and hetero-structures consisting of InAs contact layer, AlSb barriers, and GaSb well for resonant interband tunneling diode [10].

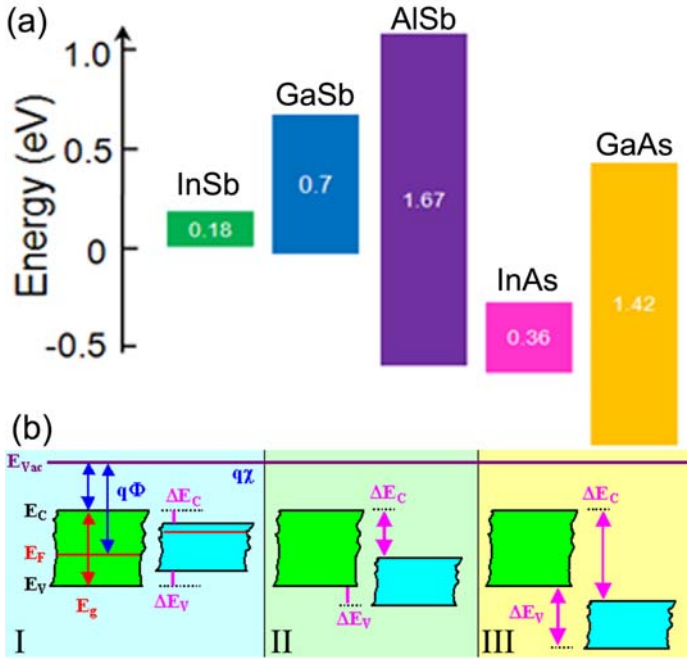

Figure 1. 2 Relative band alignments of narrow band gap III-V semiconductors in comparison with GaAs, along with the three types of band alignment. (b) Three types of semiconductor hetero-junctions organized by band alignments.

Besides the unique band structure, the physical properties, particularly the carrier mobility, distinguish the ABCS from others III-V semiconductors. The comparison of ABCS's bulk properties with those of GaAs at room temperature is summarized in Table 1.1, as can be seen; Sb-based III-V semiconductors have larger carrier mobility and smaller effective mass in comparison with those of GaAs. Indeed, the trend toward higher mobility with smaller band gap has made them a route to achieving higher speed at lower voltage and power dissipation for a given geometry as illustrated in Fig. 1.3.

Table 1. 1 Bulk properties of narrow band gap III-V semiconductors at room temperature (RT) in comparison with GaAs.

		InSb	**GaSb**	**AlSb**	**InAs**	**GaAs**
Lattice constant (Å)		6.4794	6.0959	6.1356	6.0584	5.6533
Mobility at RT ($cm^2V^{-1}s^{-1}$)	Electron	$8x10^4$	500	200	$3\ x10^4$	8500
	Hole	1250	880	375	480	400
Effective mass	Electron	0.018 m_o	0.42 m_o	0.12 m_o	0.023 m_o	0.082 m_o
	Hole	0.4 m_o	0.4 m_o	0.098 m_o	0.42 m_o	0.45 m_o

Regarding the relatively poor hole transport properties, researchers are trying to push the hole mobility to higher values via three strategies: (i) improving material quality, (ii) imposing strong confinement, and (iii) employing high levels of strain [11]. The best quality materials are largely the products of long-standing programs on antimonide growth by molecular beam epitaxy at the QinetiQ Corp. (for InSb) and at Naval Research Laboratory (for GaSb and InGaSb). Similar to Si and SiGe, when confinement and strain act on ABCS, the hole mobilities are enhanced because the degeneracy of light- and heavy- hole band is split, thereby raising the proportion of carriers in the higher mobility heavy-hole band and lowering the density of final states for scattering [12]. Using these strategies with quantum well thickness

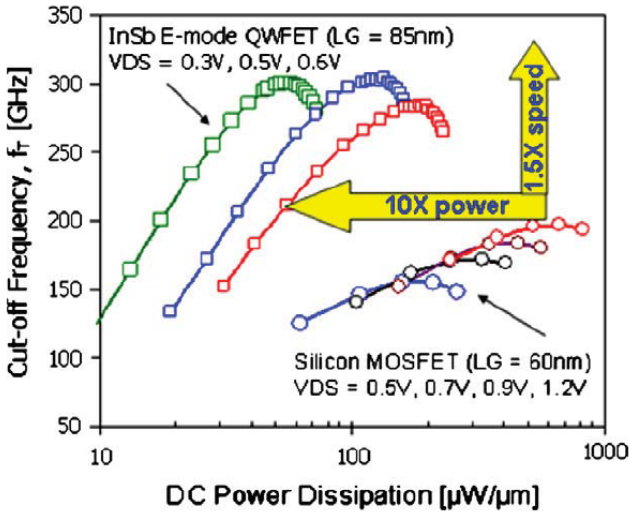

Figure 1. 3 Plot of cut-off frequency versus dc power dissipation form [17] that compares the rf performance of scaled n-channel InSb and Si devices.

in the range of 5-10 nm and biaxial compressive strains of 1-2%, p-channel mobility have been raised to into range of 1200-1500 $cm^2V^{-1}s^{-1}$ [13, 14]. Moreover, there is potential for further increase, particularly if one could reach higher strain (especially in GaSb where the best result to date has been a strain of only 0.8-1.2%), or could exert uniaxial strains as has been shown in SiGe [15] and explored theoretically for the antimonides in Ref. [16]. And even the present mobility levels, which are better than the best results in Si (though not Ge), could be sufficient for a future III-V CMOS technology. Another advantage of the antimonides is that, as in Si technology, the same material can serve as both n-channel and p-channel [7].

As shown in Fig. 1.3, a visual comparison of the cut-off frequency versus dc power of n-channel InSb and Si devices [17]. The InSb is better than Si in terms of both speed and power.

Table 1. 2 Lattice mismatch and linear thermal expansion of binary ABCS with different substrates at 300K.

	Lattice constant (Å)	Thermal expansion Coefficient (10^{-6} K^{-1})	Lattice mismatch (%)			Thermal expansion coefficient of substrates (10^{-6} K^{-1})	
			GaAs	Si	GaP		
GaSb	6.0959	6.35	7.8	12.2	11.8		
AlSb	6.1355	4.2	8.5	13.0	12.6	GaAs	6.03
InSb	6.4794	5.04	14.6	19.3	18.9	Si	2.616
InAs	6.0584	4.28	7.2	11.6	11.1	GaP	4.89

1.3 Overview of the Sb-based III-V semiconductor technology

As discussed above, ABCS are of great interest for applications in the near- and far-infrared optoelectronics and ultra-high speed low-power consumption electronics. However, ABCS on

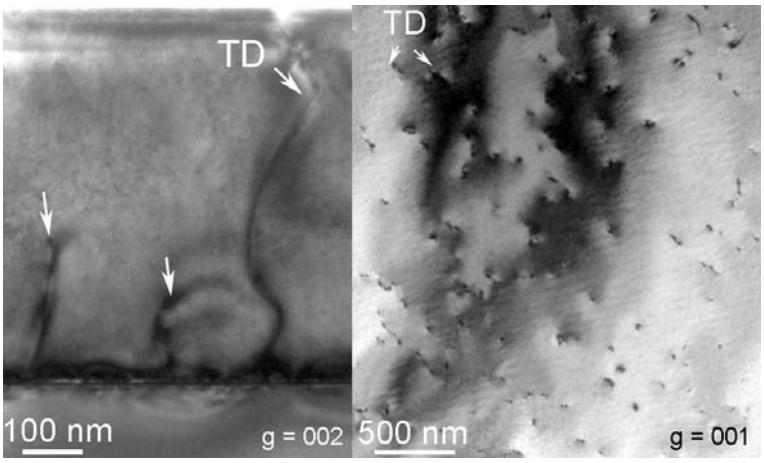

Figure 1. 4 Growth of GaSb on GaAs substrate yielding a high TDs density, 10^9-10^{10} cm^{-2} estimates form the plan-view.

commercially available substrates (Si, GaAs, and GaP) pose challenges to these applications in the form of a large lattice mismatch, difference in the thermal expansion coefficients as well as variations in

chemical and polar / non-polar mismatch (on Si substrate) at the interface. Due to these mismatch issues, attempts to deposit ABCS directly on GaAs (or Si or GaP) yield high threading dislocations (TDs) density of 10^9-10^{10} cm^{-2}, see Fig. 1.4. The TDs can propagate to the active layer and greatly hamper the reliability of the devices [18]. In the past ten years, the antimony based compound semiconductors program (ABCS program) was launched by Defense Advanced Research Projects Agency of USA in 2001 [19]. As a consequence, the study of antimony based semiconductor materials and devices were rapidly developed. And series of important development and breakthroughs have been made in the study of antimony based microstructure materials and device applications.

The epitaxy GaSb has three main objectives. (1) Understanding the fundamental issues involved in the growth of high lattice mismatched and polar on nonpolar (if on Si) semiconductor hetero-structures. An understanding of the structure of the surface, the kinetics of the initial nucleation, surface energy, how the difference in the inherent material properties of the constituents are accommodated etc., are necessary to ensure the growth of high-quality hetero-epitaxial layers. The knowledge gained from studying this system will aid the conception and optimization of the other hetero-epitaxial systems. (2) Serve as a materials system by itself, i.e., GaSb/InAs superlattices type-II photodectors [20, 21]. (3) As mentioned in the first section, serve as a base system (template) for other ABCSs (or 6.1 Å III-V) [22]. In this section, we review the recent progress on the epitaxy of GaSb as well as their applications classified according to the substrate.

(a) GaSb on Si substrate

The first attempt to growth GaSb on Si was reported by Malik et al in Bell Lab [23]. With a 600 nm AlSb buffer layer, they fabricated GaSb/AlSb optical device layers with pumped pulsed lasers emitting at 1.8 μm as well as photoconductive detectors with responsivities of 0.18 A/W. After that, epitaxial growth and characterization of GaSb layers on Si with thin AlSb inter layers have been reported by several workers [24-33]. Akahane et al. [24-26] reported the heteroepitaxial growth of GaSb films on Si substrates by

introducing an AlSb initiation layer. Using AFM, they showed that when small AlSb islands were formed on the Si substrate before the growth of GaSb, two-dimensional GaSb growth occurred. In contrast, without the growth of AlSb small islands, large GaSb islands were formed on the Si substrate. And they proposed that the AlSb interlayer plays two roles in improving crystal quality; i.e., it acts as a surfactant and as a buffer layer preventing generation and propagation dislocation [24]. The transformation of the growth mode for a three dimensional island to a layer by layer due to the inserting of AlSb interlayer has been confirmed by Kim et al. using transmission electron microscope (TEM) [27-29]. The growth mechanism of highly mismatched defect-free AlSb on Si substrates was studied by Balakrishnan et al. [31] who showed that the AlSb layer provides a template for GaSb layers on Si substrates. They reported that 13% mismatch between the AlSb interlayer layer an Si is accommodated by a spontaneously formed 2D array of 90° dislocations (or Lomer dislocations) and their growth condition produced very low defect density (~ 8×10^5 cm^{-2}) and relaxed (98 %) epitaxial layer [32, 33]. Besides effect discussed above, the gradient effect of AlSb layer on the thermal expansion may also play a role in ameliorating the GaSb quality. As can be seen from Tab. 1.2, an AlSb interlayer (4.2×10^{-6} K^{-1}) shall compensate the large discrepancy of thermal expansion coefficient between the GaSb (6.35×10^{-6} K^{-1}) and Si (2.616×10^{-6} K^{-1}) substrate.

Another barrier to growing high quality GaSb on Si is the presence of inversion domain boundaries (IDBs) commonly called anti-phase boundaries (APBs), due to the discrepancy of polarity between the epitaxial layer and substrate [34, 35]. With the established success in epitaxy of GaAs on Si [36, 37] as well as on Ge [38], miscut Si substrate was adopted in epitaxial growth of GaSb [39, 40] as well as AlSb [41] to suppress the APB. It is proposed that (001) silicon substrates with 2.5^o-5° are characterized by a double atomic step height [42] that facilitates registration of the III and V sub-lattices on the (001) plane thus suppressing the APD formation [39].

Integrating the AlSb interlayer and the miscut substrate strategies, Huffaker's group [32] has demonstrate a novel growth technique involving 90° interfacial misfit (so called IMF) arrays formed during the growth

of AlSb on Si (001) which enables a bulk GaSb epitaxy with a low defect density (~ 10^6 cm^{-2}). With novel growth technique, III-Sb based laser monolithically was grown on 5° miscut Si (001), at an emission wavelength of 1.54 μm. The device schematics, the IMF model, and electrical properties of the device are shown in Fig. 1.5. The GaSb quantum well laser diode operates under pulsed conditions at 77 K with a

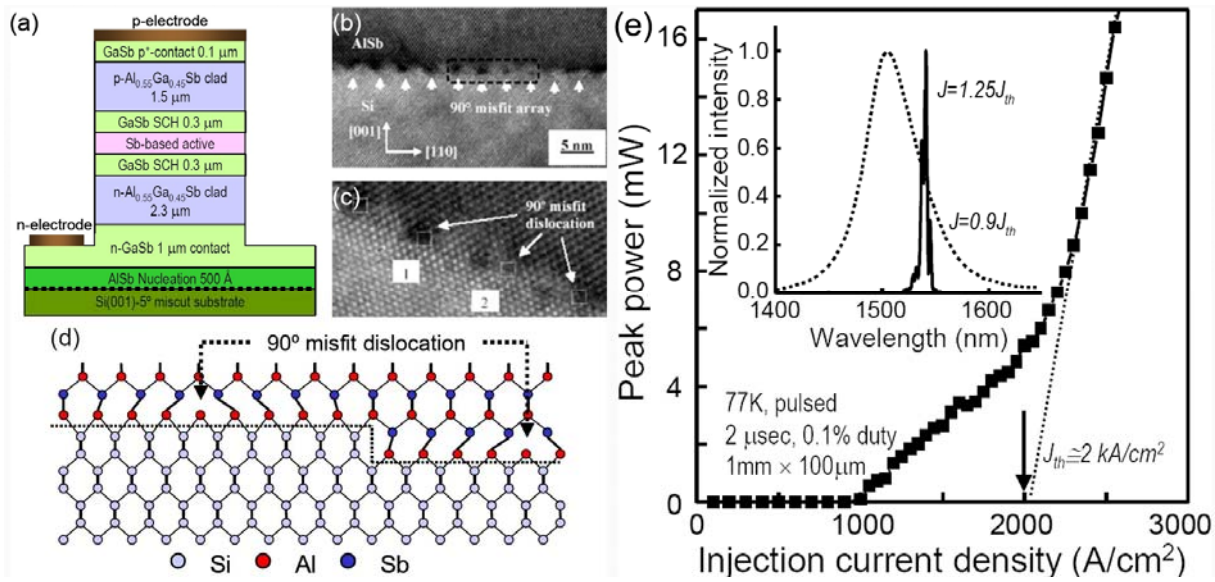

Figure 1.5 (a) Illustration of the III-Sb based laser [44]. The positive and negative electrodes are labeled p and n, respectively. (b) and (c) Cross-sectional transmission electron microscope images of the interface between AlSb and Si. (d) IMF interface between AlSb and Si. (e) output power-current curve of the laser devices at 77K under pulsed operation; inset: EL spectra above and below the threshold current density, J_{th} ≈2 kA/cm^2 [39][44].

threshold current density of 2 kA/cm^2 and a maximum peak power of ~20 mW [39, 43, 44].

(b) GaSb on GaAs

In this case, as demonstrated in epitaxy GaSb on Si, the AlSb interlayer has also been investigated extensively. Brar et al. [45] and Brown et al. [46] reported that an AlSb nucleation layer could help smooth growth at lattice mismatched interface, due to the short diffusion length of the Al adatom. Qian et al. investigated the effectiveness of several buffer layer schemes including GaSb/AlSb strained layer and

$In_{0.11}Ga_{0.99}Sb$/GaAs buffers for TDs suppression [47]. Using the most effective configuration: 1.1 µm GaSb grown on GaAs with a five periods of 100 nm GaSb/100 nm AlSb, the TDs density in the epitaxial layer was reduced to 5.0 x 10^7 cm^{-2}. Kim et al. [48] have analyzed the impact of AlSb interlayer thicknesses on the strain relief and structure properties of GaSb layer. They concluded that the smallest roughness and best interface structure were connected with the smallest AlSb interlayer (1.2 nm). Using TEM, we [49] have also investigated the influence of AlSb monolayers and substrate surface preparation on the microstructure of GaSb grown on GaAs (001) by MBE as will be discussed in Chapter 3.

Besides the AlSb interlayer, a number of classical methods which are efficient in the low mismatched system, for instance, constant composition filter layers [47], strained superlattice layers [47], compositional graded (linear or step) metamorphic layer [50], patterned substrate [51, 52], and thermal annealing [53] have proved to be partially effective for reducing the threading dislocation density in GaSb on GaAs.

In fact the work of Kang et al. [54, 55] and Rocher et al. [56-59] on the misfit dislocation network and imperfection could be at the basis of what has been known as the IMF growth technique later proposed by Huffaker's group [32, 60]. They studied the impact of growth temperature on the interface misfit dislocations [54, 59]: at low temperature (420 ^oC) a Lomer dislocation arrays were formed; at high temperature (520 ^oC) the lattice mismatch was partly accommodated by 60° dislocation array which

Table 1. 3 Defect density of different thickness of GaSb on GaAs at various growth temperatures from Huang et al. [62]

GaSb thickness / Growth Temperature	100 nm	1000 nm	3000 nm
	(/cm^2)	(/cm^2)	(/cm^2)
480 °C	5×10^9	2×10^9	2×10^9
510 °C	8.5×10^5	7.4×10^5	5×10^5
540 °C	9×10^7	3×10^7	2.8×10^7

induce a local tilt of GaSb film respect to substrate [55]. They put forward that threading dislocations originate from the imperfection of interface misfit dislocation due to the coalescence of the islands [58]. Moreover, they pointed out that towards the goal of reducing the defect density to 10^6 cm^{-2}, a perfect and

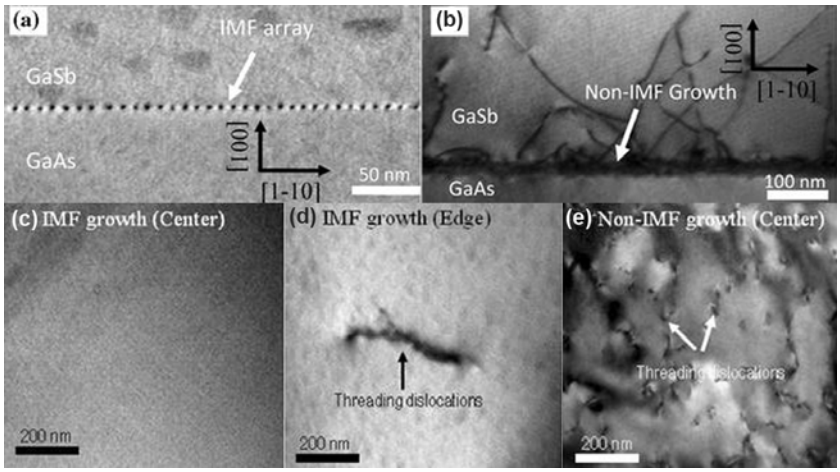

Figure 1. 6 (a) XTEM showing a periodic IMF array with a periodicity of 5.6 nm, at the GaSb/GaAs interface. (b) XTEM of non-IMF growth mode with high threading dislocation density compared to the IMF growth mode. Plan-view TEM showing TDs from (c) center, (d) edge of the IMF sample, and (e) center of the non-IMF sample for a 5 µm GaSb epilayer on a GaAs substrate [61].

uniform initial surface and interface are needed to minimize the coalescence effect [58].

Subsequently, Huang et al. and Jallipalli et al. have reported an interfacial misfit dislocation (IMF) array growth mode (Fig. 1.6) where a periodic array of Lomer misfit dislocations was assumed to form at the GaSb/GaAs interface to yield almost completely (~98%) relaxed GaSb layers with a very low TDs density (~10^6 cm^{-2}) [60-63]. It was reported that a careful monitoring of the GaAs reconstruction and initial Sb rich growth may lead to direct nucleation of a Lomer dislocations network at the interface and a two dimensional (2D) almost defect free GaSb layers at 510 ^oC by molecular beam epitaxy (MBE). Using this optimized growth mode, laser emission in the infrared has been recently demonstrated [64, 65]. The six-layer $Ga_{0.9}In_{0.1}Sb/Al_{0.35}Ga_{0.65}Sb$ quantum well (QW) has an emission wavelength of 1.816 µm with a threshold current density of 1.265 kA/cm^2, as shown in Fig. 1.7. More recently, using MOCVD Zhou et al. [66, 67] also reported a IMF epitaxy of 300 nm GaSb on GaAs, with hole density and mobility of 300 nm

GaSb epilayer are 5.27x10^6 cm^{-3} (1.20x10^6 cm^{-3}) and 553 m^{2}V^{-1}s^{-1} (2340 m^{2}V^{-1}s^{-1}) at RT (77 K), respectively. However, they didn't report the TDs density of the epitaxial layer.

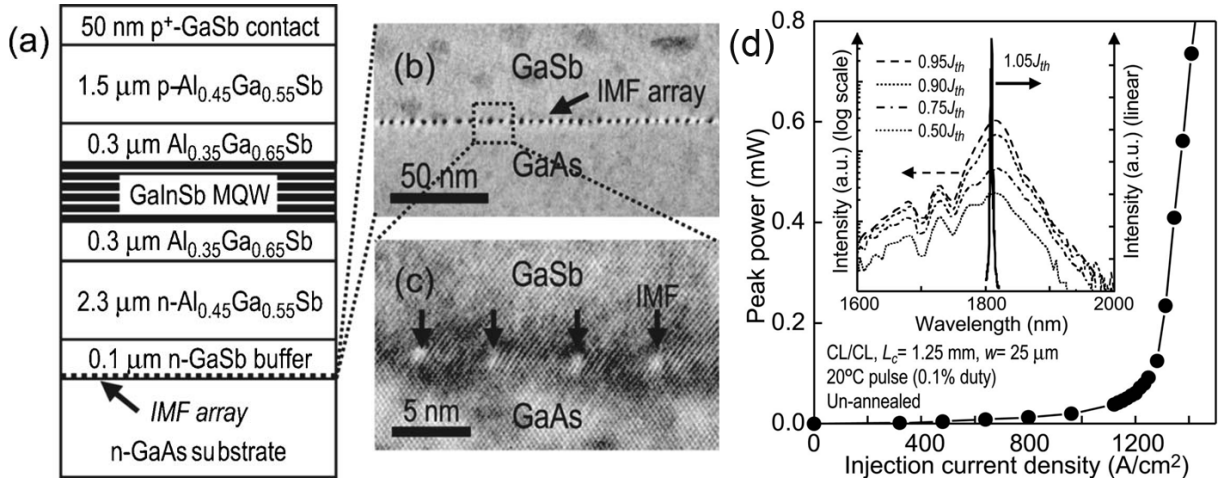

Figure 1. 7 *(a) Schematic illustration of the fabricated six-layer $Ga_{0.9}In_{0.1}Sb/Al_{0.35}Ga_{0.65}Sb$ QW laser structure. (b) and (c) cross section TEM images of the IMF array between GaAs and GaSb. (d) output power-current characteristics of the laser with Lc=1.25 mm at 20 °C under a pulsed condition (0.1% duty cycle); inset is EL spectra with different J ranging from $0.5J_{th}$ to $1.05J_{th}$ [64].*

(c) GaSb on GaP

In contrast to the extensive reports on the epitaxy GaSb on Si (GaAs) substrate, the epitaxy GaSb on GaP substrate has been hardly reported. A recent report [68] showed that APB free pseudomorphic GaP layers could be achieved on exactly oriented (001) Si substrates. These high quality GaP templates provide an alternative way for subsequent growth of antimonides on Si, due to the almost equal lattice constant (GaP: 5.4512 Å Si: 5.43095 Å). In this vein, we have investigated the influence of the surface preparation and growth temperature on the relaxation of GaSb islands on GaP [69, 70]. We will discuss this growth optimization processs in Chaper 3. With this optimized growth conditions, a high mobility (25500 cm^{2}V^{-1}s^{-1} at room temperature and 108 000 cm^{2}V^{-1}s^{-1} at 77 K) AlSb/InAs hetero-structure on a semi-insulating (001) GaP substrate with a 600 nm thick GaSb buffer layer has been achieved [69].

1.4 Objective of this work

The reports of Huffaker's group in the IMF growth constitute a significant millstone in epitaxy of Sb based III-V semiconductors. With their growth conditions, various devices have been fabricated. As their works were more focused on the growth and devices, it is clear that detailed analysis of the misfit dislocations and strain relaxation is needed. Given that the initial growth step plays a critical role in the formation of the misfit dislocation and the epitaxial layer quality, we have to address several issues. First, what's the strain relaxation state at the initial growth step and its relationship with the misfit dislocations? Second, how do these misfit dislocations form at the hetero-interface?

With these questions, this work focused on investigation of the strain relaxation and misfit dislocations at the GaSb/GaAs (GaP) interface. During the growth optimization, the microstructure of GaSb epitaxial layer, misfit dislocations, and strain relaxation were characterized by transmission electron microscopy. We have investigated the atomic structure of the misfit dislocations and their formation mechanism.

References

[1]B. Robert M, Mater. Sci. Eng. R Rep. **36**, 105 (2002).

[2] B.R. Bennett, R. Magno, J.B. Boos, W. Kruppa, and M.G. Ancona, Solid-State Electron. **49**, 1875 (2005).

[3] K. Herbert, Physica E **20**, 196 (2004).

[4] T.S. Shamirzaev, Semiconductors **45**, 96 (2011).

[5] S.M. Sze and K.K. Ng, *Physics of Semiconductor Devices* (John Wiley and Sons, 2007).

[6] M.O. Manasreh, *Antimonide-related Strained-layer Heterostructures* (Gordon and Breach, 1997).

[7]G. Tuttle, H. Kroemer, and J.H. English, J. Appl. Phys. **65**, 5239 (1989).

[8]G. Tuttle, H. Kroemer, and J.H. English, J. Appl. Phys. **67**, 3032 (1990).

[9] L.F. Luo, R. Beresford, and W.I. Wang, Appl. Phys. Lett. **53**, 2320 (1988).

[10] J.R. Söderström, D.H. Chow, and T.C. McGill, Appl. Phys. Lett. **55**, 1094 (1989).

[11] M.G. Ancona, B.R. Bennett, and J.B. Boos, Solid-State Electron. **54**, 1349 (2010).

[12]M.L. Lee, E.A. Fitzgerald, M.T. Bulsara, M.T. Currie, and A. Lochtefeld, J. Appl. Phys. **97**(1) 011101 (2004).

[13]B.R. Bennett, M.G. Ancona, J.B. Boos, C.B. Canedy, and S.A. Khan, J. Cryst. Growth **311**, 47 (2008).

[14]B.R. Bennett, M.G. Ancona, J.B. Boos, and B.V. Shanabrook, Appl. Phys. Lett. **91**, 042104 (2007).

[15]S.E. Thompson, Guangyu Sun, Youn Sung Choi, and T. Nishida, IEEE Trans. Electron Devices **53**, 1010 (2006).

[16]A. Nainani, S. Raghunathan, D. Witte, M. Kobayashi, T. Irisawa, T. Krishnamohan, K. Saraswat, B.R. Bennett, M.G. Ancona, and J.B. Boos, in *Electron Devices Meeting (IEDM), 2009 IEEE International* (IEEE, 2009), pp. 1–4.

[17]S. Datta, T. Ashley, J. Brask, L. Buckle, M. Doczy, M. Emeny, D. Hayes, K. Hilton, R. Jefferies, T. Martin, T.J. Phillips, D. Wallis, P. Wilding, and R. Chau, in *Electron Devices Meeting, 2005. IEDM Technical Digest. IEEE International* (IEEE, 2005), pp. 763–766.

[18]P.J. Taylor, W.A. Jesser, J.D. Benson, M. Martinka, J.H. Dinan, J. Bradshaw, M. Lara-Taysing, R.P. Leavitt, G. Simonis, W. Chang, W.W. Clark, and K.A. Bertness, J. Appl. Phys. **89**, 4365 (2001).

[19]M. Rosker and J. Shah, in *IEEE Gallium Arsenide Integrated Circuit (GaAs IC) Symposium, 2003. 25th Annual Technical Digest 2003* (IEEE, 2003).

[20]H. Mohseni, E. Michel, J. Sandoen, M. Razeghi, W. Mitchel, and G. Brown, Appl. Phys. Lett. **71**, 1403 (1997).

[21]B.-M. Nguyen, D. Hoffman, E.K. Huang, S. Bogdanov, P.-Y. Delaunay, M. Razeghi, and M.Z. Tidrow, Appl. Phys. Lett. **94**, 223506 (2009).

[22] P.S. Dutta, H.L. Bhat, and V. Kumar, J. Appl. Phys. **81**, 5821 (1997).

[23]R.J. Malik, J.P. van der Ziel, B.F. Levine, C.G. Bethea, and J. Walker, J. Appl. Phys. **59**, 3909 (1986).

[24] K. Akahane, N. Yamamoto, S. Gozu, and N. Ohtani, J. Cryst. Growth **264**, 21 (2004).

[25] K. Akahane, N. Yamamoto, S. Gozu, A. Ueta, and N. Ohtani, J. Cryst. Growth **283**, 297 (2005).

[26] K. Akahane, N. Yamamoto, S. Gozu, A. Ueta, and N. Ohtani, Thin Solid Films **515**, 4467 (2007).

[27]Y.H. Kim, J.Y. Lee, Y.G. Noh, M.D. Kim, S.M. Cho, Y.J. Kwon, and J.E. Oh, Appl. Phys. Lett. **88**, 241907 (2006).

[28]Y.K. Noh, S.R. Park, M.D. Kim, Y.J. Kwon, J.E. Oh, Y.H. Kim, J.Y. Lee, S.G. Kim, K.S. Chung, and T.G. Kim, J. Cryst. Growth **301–302**, 244 (2007).

[29]Y.H. Kim, Y.K. Noh, M.D. Kim, J.E. Oh, and K.S. Chung, Thin Solid Films **518**, 2280 (2010).

[30]T. Toda, Y. Jinbo, and N. Uchitomi, Phys. Status Solidi C **3**, 2693 (2006).

[31]G. Balakrishnan, S. Huang, L.R. Dawson, Y.-C. Xin, P. Conlin, and D.L. Huffaker, Appl. Phys. Lett. **86**, 034105 (2005).

[32]G. Balakrishnan, S.H. Huang, A. Khoshakhlagh, A. Jallipalli, P. Rotella, A. Amtout, S. Krishna, C.P. Haines, L.R. Dawson, and D.L. Huffaker, Electron. Lett. **42**, 350 (2006).

[33]G. Balakrishnan, S.H. Huang, A. Khoshakhlagh, P. Hill, A. Amtout, S. Krishna, G.P. Donati, L.R. Dawson, and D.L. Huffaker, Electron. Lett. **41**, 531 (2005).

[34]Z. Liliental-Weber, M.A. O'Keefe, and J. Washburn, Ultramicroscopy **30**, 20 (1989).

[35]H.K. Choi and M.R. Society, *Heteroepitaxy on Silicon: Fundamentals, Structure, and Devices: Symposium Held April 5-8, 1988, Reno, Nevada, U.S.A.* (Materials Research Society, 1988).

[36]T. Ueda, S. Nishi, Y. Kawarada, M. Akiyama, and K. Kaminishi, Jpn. J. Appl. Phys. **25**, L789 (1986).

[37]O. Ueda, T. Soga, T. Jimbo, and M. Umeno, Appl. Phys. Lett. **55**, 445 (1989).

[38]H. Tanoto, S.F. Yoon, W.K. Loke, E.A. Fitzgerald, C. Dohrman, B. Narayanan, and C.H. Tung, MRS Online Proceedings Library **891**, EE03 (2005).

[39]A. Jallipalli, M.N. Kutty, G. Balakrishnan, J. Tatebayashi, N. Nuntawong, S.H. Huang, L.R. Dawson, D.L. Huffaker, Z. Mi, and P. Bhattacharya, Electron. Lett. **43**, (2007).

[40]J. Tatebayashi, A. Jallipalli, M.N. Kutty, Shenghong Huang, K. Nunna, G. Balakrishnan, L.R. Dawson, and D.L. Huffaker, IEEE J. Sel. Topics Quantum Electron. **15**, 716 (2009).

[41]S.H. Huang, G. Balakrishnan, A. Khoshakhlagh, L.R. Dawson, and D.L. Huffaker, Appl. Phys. Lett. **93**, 071102 (2008).

[42]L. Barbier, A. Khater, B. Salanon, and J. Lapujoulade, Phys. Rev. B **43**, 14730 (1991).

[43]D.L. Huffaker, G. Balakrishnan, A. Jallipalli, M.N. Kutty, J. Tatebayashi, S.H. Huang, L.R. Dawson, Z. Mi, and P. Bhattacharya, in (IEEE, Nano-Optoelectronics Workshop, 2007. i-NOW'07. International, 2007), pp. 16–17.

[44]D. Huffaker, *Novel monolithic integration of III-Sb materials on Si substrates,* SPIE Newsroom *DOI: 10.1117/2.1200801.1002*, (2008).

[45] B. Brar and D. Leonard, Appl. Phys. Lett. **66**, 463 (1995).

[46] S.J. Brown, M.P. Grimshaw, D.A. Ritchie, and G.A.C. Jones, Appl. Phys. Lett. **69**, 1468 (1996).

[47] W. Qian, M. Skowronski, and R. Kaspi, J. Electrochem. Soc. **144**, 1430 (1997).

[48]H.S. Kim, Y.K. Noh, M.D. Kim, Y.J. Kwon, J.E. Oh, Y.H. Kim, J.Y. Lee, S.G. Kim, and K.S. Chung, J. Cryst. Growth **301–302**, 230 (2007).

[49]Y. Wang, P. Ruterana, L. Desplanque, S. El Kazzi, and X. Wallart, J. Appl. Phys. **109**, 023509 (2011).

[50] X. Weng, N.G. Rudawski, P.T. Wang, R.S. Goldman, D.L. Partin, and J. Heremans, J. Appl. Phys. **97**, 043713 (2005).

[51]S. Jha, C.-C. Liu, T.S. Kuan, S.E. Babcock, P.F. Nealey, J.H. Park, L.J. Mawst, and T.F. Kuech, Appl. Phys. Lett. **95**, 062104 (2009).

[52] S. Jha, M.K. Wiedmann, T.S. Kuan, X. Song, S.E. Babcock, and T.F. Kuech, J. Cryst. Growth **315**, 91 (2011).

[53] J.W. Lee, H. Shichijo, H.L. Tsai, and R.J. Matyi, Appl. Phys. Lett. **50**, 31 (1987).

[54] J.M. Kang, M. Nouaoura, L. Lassabatère, and A. Rocher, J. Cryst. Growth **143**, 115 (1994).

[55] J.M. Kang, S. Min, and A. Rocher, Appl. Phys. Lett. **65**, 2954 (1994).

[56] A. Rocher, M.N. Charasse, B. Bartenlian, and J. Chazelas, Le Journal De Physique Colloques **51**, C1 (1990).

[57]A. Rocher and E. Snoeck, Mater. Sci. Eng. B **67**, 62 (1999).

[58]A.Rocher and J.M.Kang, Microscopy of semiconducting Materials **146**, 135 (1995).

[59] A. Rocher and E. Snoeck, MRS Online Proceedings Library **594**, 169 (1999).

[60] S.H. Huang, G. Balakrishnan, A. Khoshakhlagh, A. Jallipalli, L.R. Dawson, and D.L. Huffaker, Appl. Phys. Lett. **88**, 131911 (2006).

[61] A. Jallipalli, G. Balakrishnan, S.H. Huang, T.J. Rotter, K. Nunna, B.L. Liang, L.R. Dawson, and D.L. Huffaker, Nanoscale Res. Lett. **4**, 1458 (2009).

[62]S. Huang, *Microscopy Study of Extreme Lattice Mismatched Heteroepitaxy Using Interfacial Misfit Arrays*, The University of New Mexico, 2007.

[63] S. Huang, G. Balakrishnan, and D.L. Huffaker, J. Appl. Phys. **105**, 103104 (2009).

[64]J. Tatebayashi, A. Jallipalli, M.N. Kutty, S.H. Huang, G. Balakrishnan, L.R. Dawson, and D.L. Huffaker, Appl. Phys. Lett. **91**, 141102 (2007).

[65]J. Tatebayashi, A. Jallipalli, M.N. Kutty, Shenghong Huang, K. Nunna, G. Balakrishnan, L.R. Dawson, and D.L. Huffaker, IEEE J. Sel. Topics Quantum Electron. **15**, 716 (2009).

[66] W. Zhou, W. Tang, and K.M. Lau, Appl. Phys. Lett. **99**, 221917 (2011).

[67] W. Zhou, X. Li, S. Xia, J. Yang, W. Tang, and K.M. Lau, J. Mater. Sci. Tech. **28**, 132 (2012).

[68] I. Németh, B. Kunert, W. Stolz, and K. Volz, J. Cryst. Growth **310**, 1595 (2008).

[69] S. El Kazzi, L. Desplanque, C. Coinon, Y. Wang, P. Ruterana, and X. Wallart, Appl. Phys. Lett. **97**, 192111 (2010).

[70] S. El Kazzi, L. Desplanque, C. Coinon, Y. Wang, P. Ruterana, and X. Wallart, Adv. Mater. Res. **324**, 85 (2011).

Chapter 2

Tools and facilities

2.1 Molecular beam epitaxy

2.1.1 Introduction of the molecular beam epitaxy system

Since A.Y.Cho and J. R. Arthur first used molecular beam epitaxy (MBE) in the late 1960s to growth GaAs epilayers [1], the high vacuum epitaxial growth techniques using particle beams have developed rapidly. MBE is used to denote the epitaxial growth of thin films by a process involving the reaction of molecular beams with a crystalline surface under ultra high vacuum conditions [2]. It is distinguished from other thin film technologies, such as liquid phase epitaxy, chemical vapor deposition, sputtering and vacuum evaporation, by its precise control of the beam fluxes and deposition conditions. Because of the vacuum deposition, MBE growth is carried out under the condition that is far from the thermodynamic equilibrium. The growth is mainly controlled by the kinetics of the surface processes occurring when the impinging beams react with the outermost atomic layers of the substrate [2]. A detailed knowledge of surface physics and the observation of surface reconstruction allow high-quality thin films to be fabricated on an atomic layer scale. This precise control makes MBE an important technique to achieve self-organized growth. It is essentially a two step process carried out in an ultra-high vacuum environment [2]. As shown in Fig. 2.1, the first step is the evaporation of atoms which are the constituents of the growing materials (e.g. Ga and Sb for GaSb) from solid sources in heated cells. The evaporated particles are then collimated into beams and directed toward a heated substrate. The particles in the beams are not allowed to collide or react with one another, they are made to behave as a molecular flow (thus the name “molecular beam epitaxy”) depositing on a substrate surface. The substrate is rotated to obtain uniform deposition. The second step is the migration of the deposited species on the surface prior to their incorporation to the crystal lattice of the substrate or the growing epitaxial layer. This step determines the morphology of the film, which depends on factors

such as the substrate surface reconstruction, the deposition rate, the surface temperature, and the crystallographic orientation.

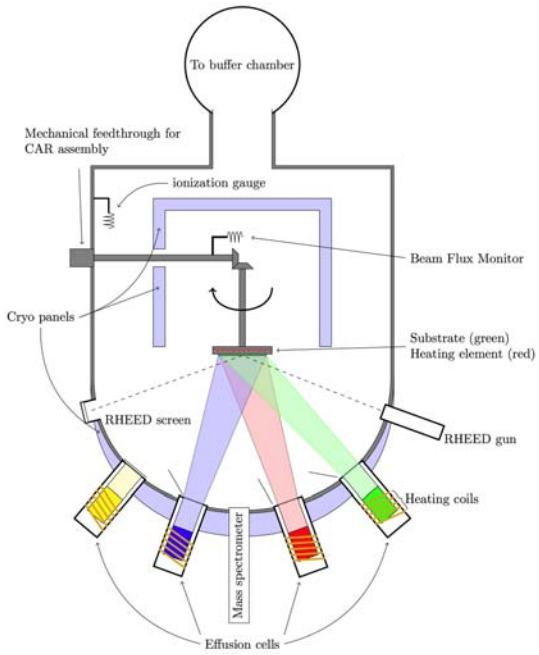

Figure 2.1 A simple sketch showing the main components and rough layout and concept of MBE growth chamber [3].

2.1.2 Specific growth

In this work, the GaSb epitaxial layer and islands were growth by 3-inch Riber Compact 21TM MBE system with a base pressure better than 1×10^{-10}Torr at IEMN Lille. In this MBE system, several solid sources such as As, P, Sb, Ga, Al, and In were available. Two substrates were used, GaAs semi-insulating substrates oriented along (001) $\pm0.5^{o}$ and GaP substrate oriented along (001) $\pm0.1^{o}$. The GaAs (GaP) substrate is first de-oxidized at 625°C (625°C) under an As (P) flux, and then several hundred nm GaAs layer was growth at 580°C (610°C) to smooth the surface. Then, the Ga and As (P) valves were closed and the sample temperature is decreased to the growth temperature. Before GaSb layer growth, a number of surface reconstructions were fixed as starting conditions. According to the sample involved, we will give detailed information for surface reconstruction and growth parameters in the results section. The surface reconstruction and the growth process were monitored by in situ reflection high-energy electron diffraction (RHEED). For all the samples, during the initial steps, the

RHEED pattern turned rapidly to a 3D RHEED pattern indicative of a Volmer Weber mode when GaSb growth began. After a few nanometers, a 2D RHEED pattern with 1x3 surface reconstructions appeared.

2.2 Microscopy

2.2.1 Principle

The main working principle of a transmission electron microscope is similar to an optical microscope. Schematic image cross-sectional images of TEM and an optical microscope can be seen in Fig. 2.2. But for TEM one uses electrons which are manipulated by magnetic lenses instead of light.

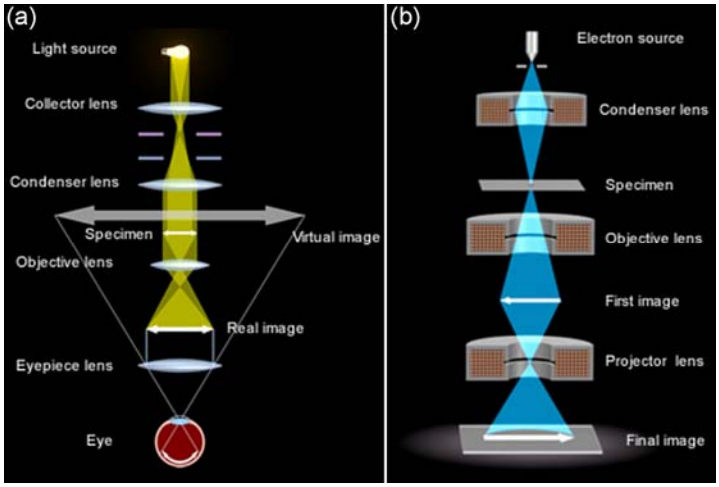

Figure 2.2 The schematic comparison of a optical (a) and electron (b) microscopy [4].

To be able to control the electron beam the electron microscope consists of a column with an electron gun at the top followed by a series of magnetic lenses and the electron beam propagate in vacuum. The main features of a modern microscope are shown in Fig. 2.3. The electron gun generates the electron by exposing a fine tip of ZrO_2 coated W (Schottky emitter) to an intense electric field (field emission gun: FEG). Earlier instruments were equipped with electrically heated filament [5], so called thermionic guns, where heat was used to overcome the work function (Φ) of a fine tip of LaB_6 or W by a selected negative potential ≥ 100 kV. Then, the emitted electrons are accelerated to earth and are

focused, via a double condenser lens system with field limiting apertures referred to as the condenser system, onto the specimen. Two operational modes can be chosen for this system: a parallel beam for the formation of a projected image or a condensed beam to probe the sample point by point. The former is used in conventional TEM and high-resolution TEM (HRTEM) and latter in scanning TEM (STEM). These methods generate a representative image of the sample by slightly different processes. The image or diffraction pattern from the specimen is obtained on fluorescent screen or CCD camera via a three- or a four- lens magnification system. Image contrast may be enhanced by the use of an objective aperture, and the area for diffraction may be selected by a selected area aperture. The image is focused with the objective lens and magnification is controlled by the use of the projector system.

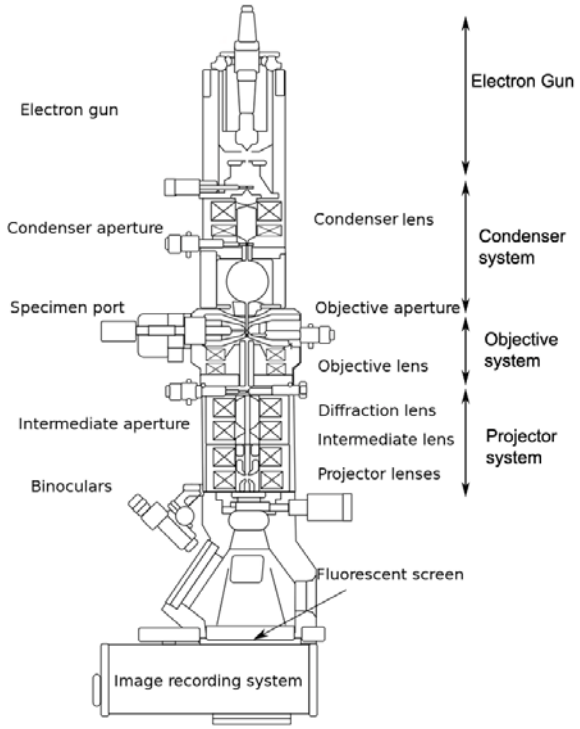

Figure 2.3 A cross-section of a TEM column. In principle the TEM is built up by electron gun, condenser system, objective system, and projector system [6].

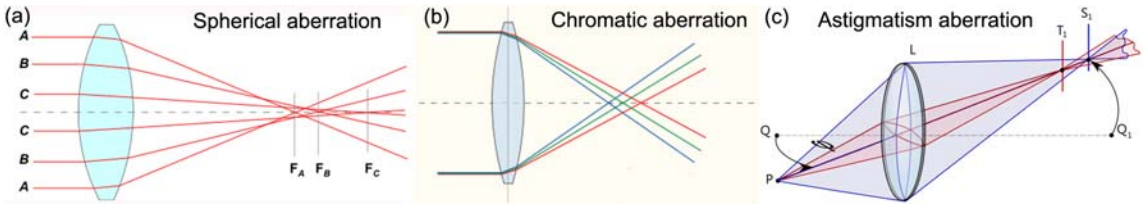

Figure 2.4 Objective lens aberrations: (a) spherical, (b) chromatic, (c) astigmatism

Like optical lenses, all electromagnetic lenses suffer from the aberrations such as coma, astigmatism, chromatic and spherical aberration which are discussed in detail by Haine and Cosslett [7]. From the operator's standpoint the last three are the most important in relation to the objective lens because they determine the resolution of the electron microscope. These defects are shown schematically in Fig. 2.4. Spherical aberration is particularly important because there is no convenient way of correcting it. It causes an image to be blurred because points are imaged as discs; its radius r_s is given by $r_s = C_s\beta^3$, where C_s is the spherical aberration constant, β is the lens aperture. The chromatic aberration arises because of the energy, and therefore wavelength, spread of the electron beam. It leads to a rainbow distribution at the edge of an image because light of different color is refracted at different angles. A disc of confusion, radius r_c is produced, given by $r_c = C_c\beta\frac{\Delta E}{E}$, where C_c is the chromatic aberration constant of the lens, ΔE is the deviation of the electron energy from its mean value E. Astigmatism occurs when the lens exhibits different focal lengths, depending upon the plane of the ray paths. Thus, again a point on the object is imaged as a disc of confusion, radius r_A, given by $r_A = \Delta f_A\beta$, where Δf_A is the maximum difference in focal length from astigmatism. This defect may be corrected using electromagnetic astigmators that produce a small controllable magnetic field.

The mechanism for aberration correction was suggested more than fifty years ago by Scherzer [8] with pioneering attempts to reduce it to practice by Crewe [9], Rose [10], Haider [11], Krivanek [12] and others over the last thirty years. Essential to successful C_s correction is precise control the corrector alignment, which finally is possible today also because of advances in computer technology. Two distinct paths have been and are being pursued for C_s correction hardware: for TEM, systems of hexapoles [11] and for STEM, systems of quadrupoles and octupoles [7]. While the hexapole design exhibits relative simplicity, it is not simply extendable for C_c correction and has larger intrinsic C_c. The quadrupole/octupole design can be extended to C_c correction with addition of electrostatic elements (Wien Filter, a device consists of perpendicular electric and magnetic fields that can be used as a velocity filter for charged particles [13].), but the configuration is much more complex and

exhibits large off-axis aberrations; the latter is more suitable for STEM for which the effects of C_c are mitigated by high angle annular dark field imaging.

Combining these C_s and C_c correctors the 0.5 Å information limit has been recently achieved in both TEM and STEM mode by the so-called TEAM I [14, 15] and PICO [16] microscope. For instance the PICO microscope has information limits of < 0.50 Å, < 0.58 Å, and < 0.80 Å operated at 300 kV, 200 kV, and 80 kV for the TEM mode, and resolution of < 0.50 Å and < 0.80 Å operated at 300 kV and 80 kV for STEM mode, respectively. Both TEAM I and PICO are based on a commercial FEI Titan electron microscope, which can be operated at voltage between 80 and 300 kV. To minimize the mechanical vibrations, the microscope is separated from its surroundings by a vibration free (or isolation) system and is operated remotely. The energy spread of electron source is reduced by a Wien-filter type monochromator, in order to reduce the chromatic aberrations. Furthermore, the condenser lens and the objective lens are equipped with CEOS hexapole spherical aberration corrector and C_s-C_c achro-aplanat corrector [17], respectively. The illumination aberration corrector corrects coherent axial aberration up to 4th order, as well as 5th order spherical aberration and six-fold astigmatism. The imaging aberration corrector fully corrects for coherent axial aberrations up to 3rd order and partially compensates for 4th and 5th order spherical aberration, as well as the chromatic aberrations (typically residual chromatic aberration less than 10 µm [15, 17]).

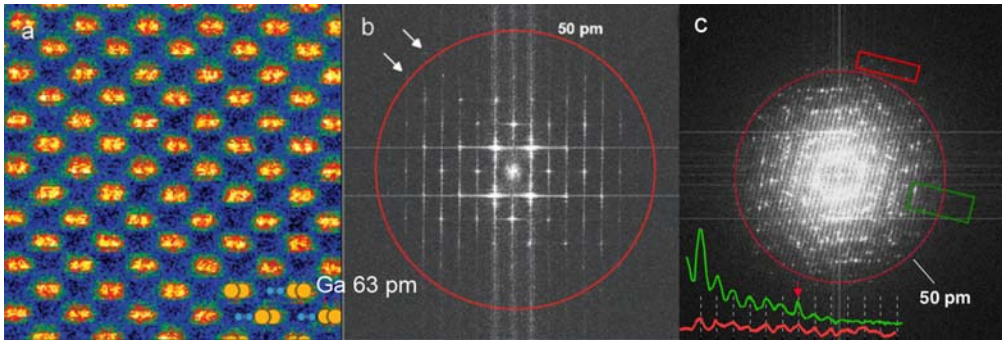

Figure 2.5 TEAM 0.5 STEM and TEM performance [18]. (a) HAADF image of wurtzite GaN [211]; crystal structure shown in the inset indicates Ga dumbbell spacing of 63 pm in this projection. (b)The corresponding diffractogram shows Fourier Fourier components below 50 pm marker indicated by the circle. (c) The Fourier diffractogram from HRTEM images shows Young's fringes extending beyond the 50 pm marker indicated by the circle.

The performance of the initial version TEAM 0.5 without C_c correction is illustrated in Fig. 2.5. A STEM image of GaN in [211] orientation shows the 63 pm distance Ga dumbbells clearly resolved. Tab. 2.1 gives a list of the typical residual aberration coefficients of TEAM 0.5 for operation at 300 kV from Kisielowski et al. [18]. A detailed account of the aberration coefficients and the aberration function can be found in Ref. [17].

Table 2.1 Typical residual axial aberration coefficient of the illumination aberration corrector and the imaging aberration corrector of TEAM 0.5 for operation at 300 kV. First-order aberrations, C1,and A1 are manually optimized (Kisielowski et al. [18])

Aberration coefficient	**Illumination (nm)**	**Imaging (nm)**
Defocus C1	NA	NA
Twofold astigmatism A1	NA	NA
Threefold astigmatism A2	24	43
2nd-order coma B2	8	38
3rd-order spherical aberration C3	-150	-341
Fourfold astigmatism A3	97	1.0×10^{3}
3rd-order star aberration S3	90	921
Fivefold astigmatism A4	10.2×10^{3}	13.4×10^{3}
4th-order three -lobe aberration D4	7.2×10^{3}	3.3×10^{3}
4th-order coma B4	5.5×10^{3}	8.0×10^{3}
5th-order spherical aberration C5	508×10^{3}	5.1×10^{6}
Sixfold astigmatism A5	220×10^{3}	1.4×10^{6}
5th-order rosette aberration R5	24×10^{6}	153×10^{3}
5th-order star aberration S5	6.6×10^{6}	430×10^{3}

In this study, I have used three transmission electron microscopes:

- JEOL 2010 LaB_6: Operated at 200 kV, mainly used for conventional observation, such as low magnification in plan-view, two beam and weak beam observation.
- JEOL 2010 FEG: 200 kV High Resolution TEM with a maximum point resolution of 0.19 nm (the C_s=1.4 mm for HRTEM), coherent illumination due to the FEG. This microscope was used in this work for high resolution imaging.
- Titan 80-300 cubed: 300 kV High Resolution TEM equipped with an objective spherical aberration corrector at Institute of Physics of the Polish Academy of Sciences, Warsaw. This microscope was used for imaging the atomic structure of the misfit dislocation by HRTEM and HAADF (the C_s=0.001 mm for HRTEM, C_s=1.2 mm for HAADF, and C_c =1.4 mm).

2.2.2 TEM sample preparation

Plane-view and cross-sectional samples were prepared for TEM, HRTEM, and HAADF investigations. For the cross-sectional samples, slices of (1.5~2) x 5 mm^2 were cut from the substrate side along the [110] and $[1\bar{1}0]$ directions. Two slices were glued face to face and packed in copper tube of 3 mm in diameter with the epoxy glue, and then the tubes were cut into disks of about 800 μm in thickness. The procedures are illustrated in Fig. 2.6. The disks were then mechanically polished and dimpled from both sides until the thickness of the central area was about 10 μm. The final thinning was performed by argon ion milling at -150 ^{o}C in order to minimize ion beam damage. For the plane-view observation, samples were cut into 3x3 mm^2 and polished, dimpled and ion milled from the substrate side.

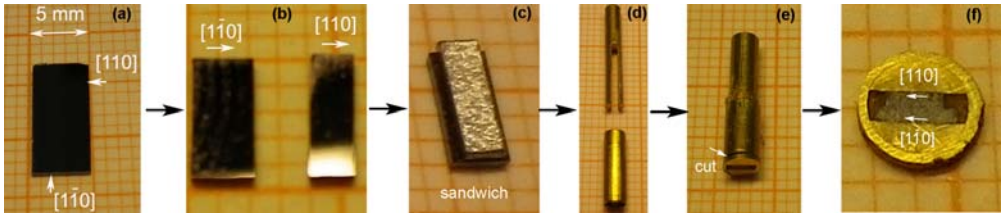

Figure 2.6 Procedure for preparing 3 mm disks of cross-sectional samples: (a) and (b) cut the sample into slices along [110] and $[1\bar{1}0]$ directions; (c) glue the slices face to face and form a sandwich structure; (d) and (e) pack the sandwich structure in the copper tube; (f) cut the tube into 3mm disks of 0.8 mm thickness.

2.3. Modes of operation and theoretical background

In this section some of the general techniques of electron microscopy as well as their theoretical background used in this work are summarized.

2.3.1 Diffraction

When it comes to diffraction, two concepts need to be considered: kinematical and dynamical diffraction. In kinematical diffraction single scattering is dominating; this is valid for very thin samples only. For dynamical diffraction, multiple scattering events occur as the electron pass through the sample. In this case, some electrons are even said to be absorbed due to repeated inelastic scattering events which send those electrons out of the main beam. Also, the incident and scattered

beams are coupled as multiple diffraction can contribute to the incident beam. The distribution of diffracted electrons in reciprocal space is referred to as the diffraction pattern and can be analyzed to determine the crystallinity and structure of the sample. When it comes to dynamical diffraction the relative intensity of the diffraction spots will change with sample thickness and atomic number, Z. For diffraction due to crystalline, the Bragg condition [19] must be fulfilled. This means that constructive interference of diffracted electron waves occurs at the Bragg angle, θ_B.

Another specific case of diffraction observed in this work is double diffraction, as shown in Fig. 2.7. This process occurs when the electron beam is rediffracted by a second crystal of different orientation and/or structure than the first crystal. This generates satellite spots in the diffraction pattern since the resultant diffraction vector depends on the combination of vectors from the two crystals. The relative position of the two crystals can be determined based on the appearance of the diffraction pattern. In so-called crystal-2 patterns the upper crystal gives the main diffraction spots while the lower crystal corresponds to the satellite spots [20]. But the opposite relationship has also been found [21]. The latter case is referred to as the top-bottom effect and can be attributed to dynamical diffraction effects, where the size of the deviation parameter causes the strongest diffracting spots to be arranged around the spot of the lower crystal.

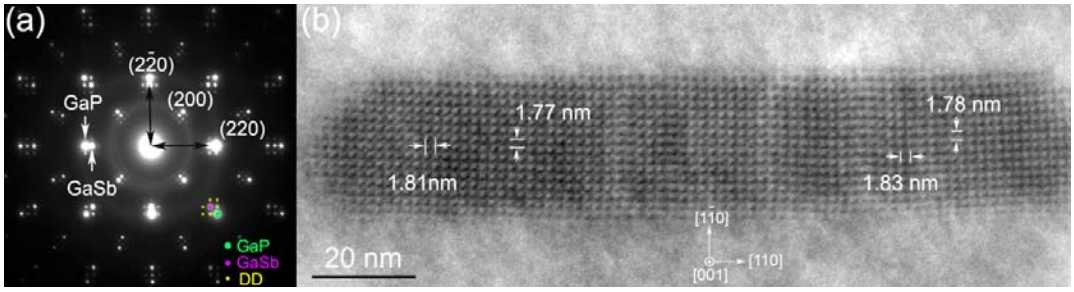

Figure 2.7 (a) The selected area electron diffraction (SAED) pattern of GaSb island on GaP substrate. The different color spots show classification of the ($2\bar{2}0$) diffraction, green, red and yellow spots are corresponding to GaP, GaSb, and double diffraction (DD), respectively. (b) [001] bright field image showing the (220) and ($2\bar{2}0$) moiré fringes [22].

Double diffraction is very often accompanied by Moiré fringes in the corresponding TEM image as a consequence of interference between two different periodically spaced structures [20]. Depending on

the relative orientation of the spacings different Moiré fringes types are observed. Parallel fringes of two overlapping structures cause translational Moire fringes where the new spacing, d_{tm} is related to the respective spacings d_e and d_s of the epitaxial material and substrate.

$$d_{tm} = \frac{d_e d_s}{d_e - d_s} \tag{2.1}$$

Here I show an example that the moiré fringe patterns is applied to investigate the strain relaxation of an individual island. Applying this equation to a relaxed GaSb on GaP, the ideal spacing $D_{\{110\}}$ is 1.83 nm. As shown in the Fig. 2.7 (b), the [110] and $[1\bar{1}0]$ direction show different Moiré fringe spacing, indicating an anisotropic strain relaxation in the two directions [22].

2.3.2 Bright, dark and weak beam images

In the bright field (BF) mode of the TEM, as shown in Fig. 2.8 (a), an aperture is placed in the back focal plane of the objective lens which allows only the direct beam to pass. In this case, the image results from a weakening of the direct beam by its interaction with the sample. Therefore, mass-thickness and diffraction contrast contribute to image formation: thick areas, in which heavy atoms are enriched, and crystalline areas appear with dark contrast. In dark field (DF) images (Fig. 2.8 (b)), the direct beam is blocked by the aperture while one or more diffracted beams are allowed through the objective aperture. Since diffracted beams have strongly interacted with the specimen, very useful information is present in DF images, e.g., about dislocations, stacking faults or particle size.

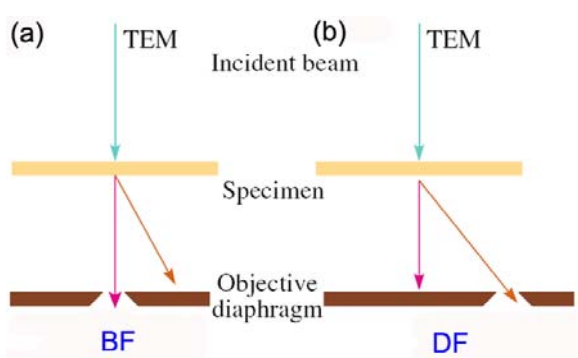

Figure 2.8 Comparison of the use of an objective aperture in TEM to select (a) the direct and (b) the scattered electrons forming BF and DF images, respectively.

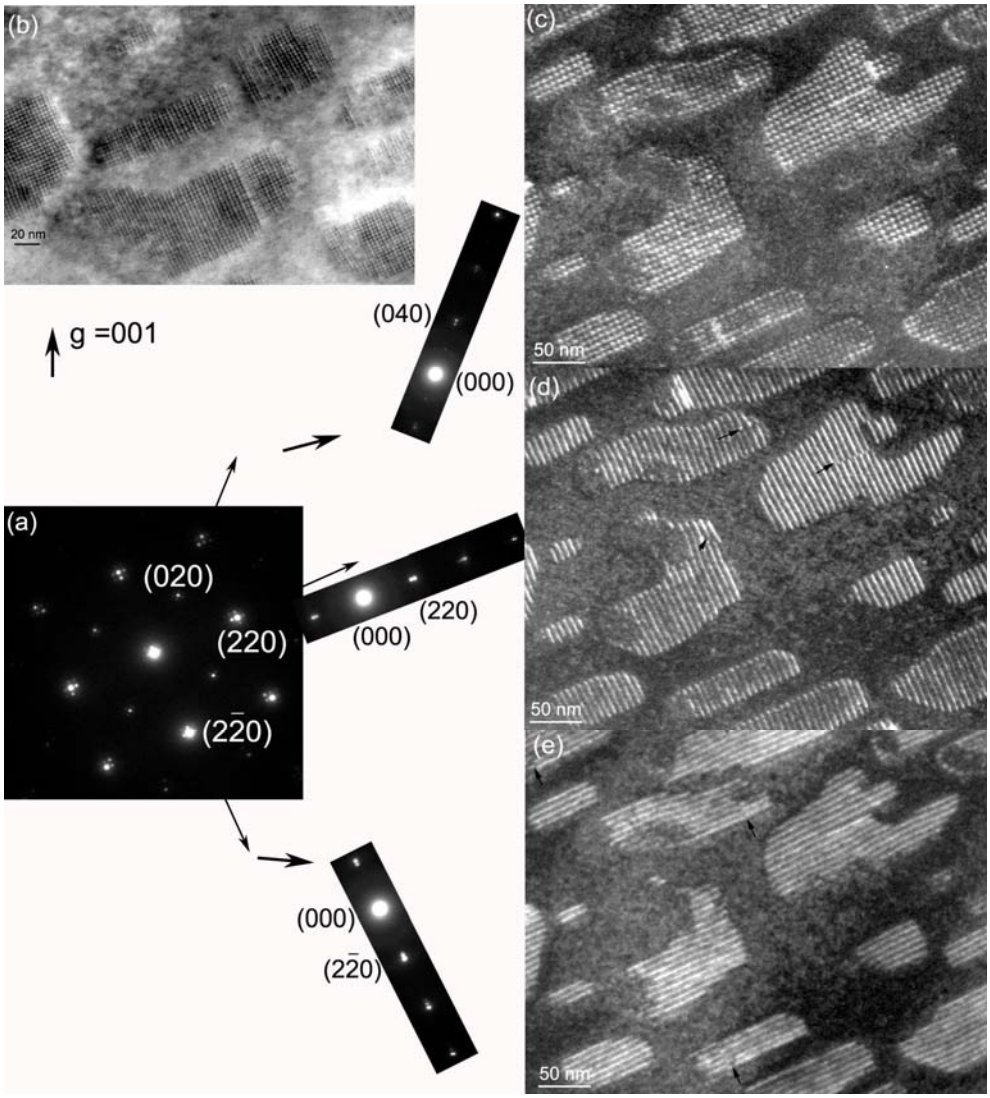

Figure 2.9 (a) The [001] zone axis diffraction patterns of GaSb islands on GaAs. (b) [001] bright field image showing the (220) and ($2\bar{2}0$) moiré fringes. WBDF images of the same area recorded with different reflections of : (c) g = 040, (d) g= 220, and (e) g= $2\bar{2}0$.

Weak beam (WB) images refer to formation of a diffraction-contrast image in either BF or dark field (DF) where the useful information is transferred by weakly excited beams. The DF approach has been more widely used; because it gives strong contrast of the defects. In principle, the WBDF technique is an on-axis dark field imaging method by using a diffracted beam with large excitation error for the defect-free sample area. Thus, the defect free sample area appears dark because of the weak diffraction intensity. However, close to the dislocation core the hkl planes are bended back into the Bragg condition, which gives rise to a bright intensity peak (the dislocation line). The main challenge is to

adjust the tilt conditions in the way that the excitation error of the *g* reflection used is close to zero only near the dislocation core where the bending of the hkl plane is most prominent. Then a very sharp dislocation line near the dislocation core becomes visible in the WBDF image.

Here we show an example; we use WBDF technique to image the misfit dislocation arrays formed at the GaSb/GaAs interface. As the dislocation has <110> type Burgers vector, one can use *g* = 040 WBDF reflection to interpret their 2D network, as shown in Fig. 2.9 (c). Using *g* = 220 and $2\bar{2}0$ refection, the two sets of Lomer dislocation array are imaged separately. The two set of Lomer dislocation with $b = \frac{a}{2} < 110 >$ and $b = \frac{a}{2} < 1\bar{1}0 >$ appear as bright lines in Fig. 2.9 (d) and (e), respectively. And the disruptions of the Lomer dislocation array are also visible (as marked by the arrows).

2.3.3 HRTEM

With the microscope, what we would like to do is to transfer all the information from the specimen to the image, this process is known as mapping. There are two problems to overcome and we can never be completely successful in transferring all the information. First, the lens is not perfect so some of the information will be distorted and a point in the specimen will be imaged as a disc. The second issue is that we have to interpret the image using an atomic model for the material. Ideally, this model will include a full description of atomic potential and the bonding of the atoms, but we don't know that either [11, 20].

The above mentioned smearing effect is often referred to as the point spread function (PSF). This can be described based on the transfer of spatial frequencies, *u* in Fourier space as follows (Eq. 2.2) where *G(u)* corresponds to the Fourier transform of a disk in the image, *F(u)* the Fourier transform of the point in the sample and *H(u)* the Fourier transform of the PSF.

$$G(u) = H(u)F(u) \qquad (2.2)$$

The PSF can in turn be expressed as the product of the aperture function, *A(u)*, the envelope function, *E(u)* and the aberration function, *B(u)* (Eq. 2.3). An aperture effectively reduces the size of the beam

and prevents part of it from being fully transferred. The envelope function is an intrinsic property of the lenses similar to *A(u)* as the beam is attenuated when passing through the lenses. The aberration function corresponds to the distortion of the beam caused by the imperfect lenses and can be expressed as eq. 2.4.

$$H(u) = A(u)E(u)B(u) \qquad (2.3)$$

$$B(u) = e^{-i\chi(u)} \qquad (2.4)$$

The function $\chi(u)$ (Eq. 2.5) is in turn dependent on defocus, Δf, wavelength, λ, and the spherical aberration constant, C_s. When expressed as $sin\chi(u)$ vs u it is referred to as the contrast transfer function (CTF) and can be used to study the degree of useful information transferred by the microscope.

$$\chi(u) = \pi\Delta f\lambda u^2 + \tfrac{1}{2}\pi C_s\lambda^3 u^4 \qquad (2.5)$$

The phase contrast in the formed image follows the fluctuations of the CTF. The presence of zeros in the CTF means that we have gaps in the output spectrum which do not contribute to the output signal: it's as if these frequencies were filtered out. Obviously, the best transfer function is the one with the fewest zeroes. In 1949, Scherzer put forward that the CTF could be optimized by balancing the effect of spherical aberration against a particular negative value of Δf. This value is known as Scherzer defocus, which occurs at

$$\Delta f = -(\tfrac{4}{3}C_s\lambda)^{\frac{1}{2}} \qquad (2.6)$$

At this defocus all the beams will have nearly constant phase out to the first crossover of the zero axis. Up to this crossover point the CTF has the same phase and the contributing frequencies are easily interpretable. This crossover point is defined as the instrumental resolution limit (as shown in Fig. 2.10) by the reciprocal value of the first crossover value,

$$r = 0.66C_s^{\frac{1}{4}}\lambda^{\frac{3}{4}} \qquad (2.7)$$

This is the best performance that can be expected from a microscope unless we use image processing schemes to extract more information. After the cross-over, oscillations in the CTF make the information at high spatial frequencies difficult to interpret. However, if the CTF is fully known for the instrument used, image reconstructions from focal or tilt series can make use of these

frequencies [24]. All spatial frequencies are then sampled and transferred to the same phase in the CTF to form a reconstructed image. The resolution limit in such an image is in theory the information limit of the microscope as determined by the envelope damping function, as shown in Fig. 2.10. The effect of the envelope is to impose virtual aperture in the back focal plane of the objective lens, regardless of the setting of focus.

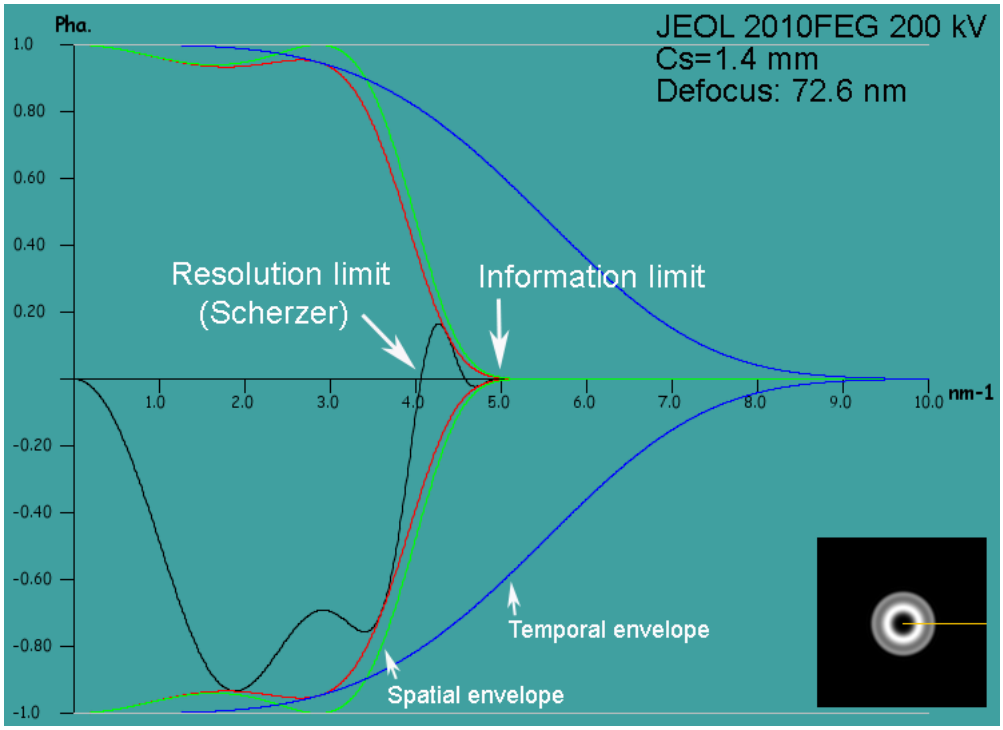

Figure 2.10 The contrast transfer function at Scherzer focus (-72.6 nm) of a 200 kV JEOL 2010FEG microscope with C_s =1.4 mm plotted as sinχ(u) vs the reciprocal spacing u.

The information limit resolution can be expressed as in Eq. 2.8 where Δ depends on the chromatic aberration constant, C_c and the fluctuation in voltage, $\delta V/V$, lens current, $\delta I/I$ and the energy spread of the electron beam, $\delta E/E$ (Eq. 2.9) [25].

$$d_L = \sqrt{\pi\lambda\Delta/2} \tag{2.8}$$

$$\Delta = \sqrt{C_C(\delta V/V)^2 + (2\delta I/I)^2 + (\delta E/E)^2} \tag{2.9}$$

These factors are some of the main instrumental parameters of the TEM-manufacturers and have led to the development of the field-emission gun (FEG), the aberration corrector and the monochromator.

With the FEG the stability of the electron gun was greatly enhanced and in combination with a monochromator reducing the energy spread as well as lens C_s corrector, the information limit has been highly expected [26, 27].

After the practical realization of the C_s corrector [11], an important wealth of materials science questions can now be addressed. Atom column dumbbells can now be imaged correctly. Optimum contrast conditions were found for high resolution imaging with spherical aberration corrected instruments, which are negative C_s imaging conditions [28] – that means negative C_s and over focus – resulting in white atom contrast on dark background (Fig. 2.11). They are especially useful for imaging weakly scattering light atoms in the surrounding of strongly scattering heavy atoms, for the case that when linear imaging theory can be applied [29, 30]. Since then, imaging with variable spherical aberration is a practical reality and single atomic columns with different atomic numbers adjacent to each other can be imaged both in aberration corrected HRTEM and STEM modes [31-35].

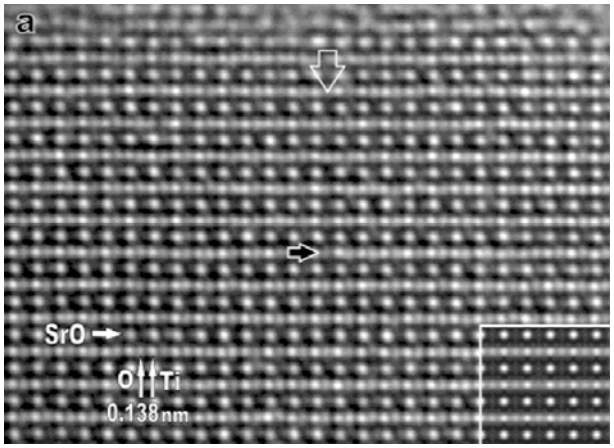

Figure 2.11 The figure shows C_s corrected HRTEM image of $SrTiO_3$ [110] with a negative C_s, the oxygen columns are visible. The inset shows a simulated image with a specimen thickness of a 4 nm, a spherical aberration of -40 µm, and a defocus of 8 nm [30].

After the C_s corrector, a demand for even higher resolution far below 1 Å had emerged. The innovation of the C_c corrector for compensating the second important axial aberration [17], the chromatic aberration, push the spatial resolution down toward to 0.5 Å [18].

2.3.4 Z-contrast imaging or STEM

In STEM, a small diameter, convergent electron probe is scanned over a defined area of the sample. At each spot, the generated signal is simultaneously recorded by selected detectors, building up an image. As shown in Fig. 2.12, three types of detectors are used to obtain STEM images: BF detector, annular dark field (ADF) detector, and high angle ADF (HAADF) detector. The BF detector collects the direct beam from a point on the specimen. The ADF detector is a disk with a hole in its center. The ADF image formation is similar to the DF mode in TEM. The measured contrast mainly results from the electrons diffracted in crystalline areas but is superimposed by incoherent Rutherford scattering. The HAADF is also a disk with a hole, but the disk and the hole are much larger than in the ADF detector. Thus, it detects electrons that are scattered to higher angles and almost only incoherent Rutherford scattering contribution to the image.

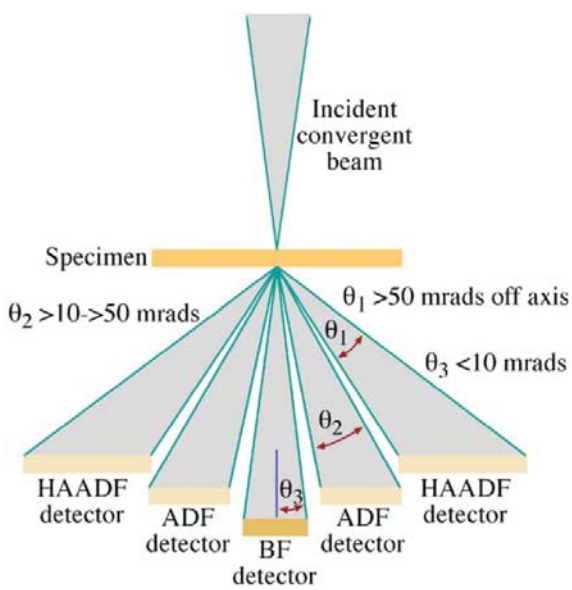

Figure 2.12 Arrangement of the various STEM detectors [20].

The intensity in a HAADF image is given by $I(r) = O(r)*P^2(r)$, where $O(r)$ is the object function and $P^2(r)$ is the resolution function [36]. Hence, in an atomic resolution Z-contrast STEM experiment the resolution achievable is due to the size of the object function, $O(r)$, convoluted with the resolution function, $P^2(r)$, where the latter is the size of the electron beam scanned on the specimen [37]. The use of a field emission gun allows one to obtain small and highly coherent probes. The size of the smallest

electron beam achievable in a STEM is given by $0.43\ C_s^{1/4}\lambda^{3/4}$ [38], where C_s is the spherical aberration coefficient of the objective lens and λ is the electron wavelength. Hence, in the our case, through the objective C_s corrector gives no help to the STEM, the used electron optical conditions still give a probe size of 0.136 nm, as we will show later that the polarity of GaSb dumbbells structure can be identified in the (110) projection. Furthermore, the intensity in a HAADF image is strongly dependent on the atomic number of the chemical species in the atomic columns. In fact, the object function convoluted with the annular detector is given approximately by $O(R) = \beta^2 V^2(R)$ [37, 39], where β is the interaction constant m/h^2, m is the relativistic mass of the electron, and $V(\mathbf{R})$ is the projected potential. Hence, for high scattering angles and thin specimens, the intensity of the spots in the images corresponds to the square of the projected crystal potential of the chemical species inside atomic column. Because of the high scattering angle, the 1*s* columnar state is the main contribution of the HAADF image [40]. With this 1*s* approximation, the HAADF image intensity as integrated on the whole large angle detector, is proportional to Z^2 where Z is the related to the atomic number of the atomic column [41].

In Chapter 4, we use the QSTEM [42] software package to perform the HAADF image simulation. Similar to the HRTEM simulation, the approach-multisilice algorithm was used in this software. The principle of multislice method is to divide a model of the sample in thin slices normal to the incident beam and allow the beam to pass the slices one by one, and the electron wave function ψ after the *n*th slice is given by $\psi_n(x) = [q_n(x)\psi_{n-1}(x)] \otimes pn(x)$, where *qn* and *pn* are the transmission function (the phase grating) and the propagator function for the *n*th slice, respectively, the symbol $\otimes$ represents the convolution operation and the vector x indicates a two-dimension position over the slice.

The QSTEM software package as well as the introduction and tutorial are available on Christoph Koch's webpage [43]. Here we briefly introduce the process of this simulation. The super cells with dislocation are generated by the molecular dynamic simulation. The input model file uses the .cfg format described as a set of <x, y, z> coordinates for the atom position. After loading the model, we can view it in 3D and define the size and orientation of the super cell. Then, define the scan region, set up the probe array, define the slice, and set up the microscopy parameters, as schematically shown in

Fig. 2.13. After that you can save the configuration to a file using “Save config” and click “start simulation” to run the program. An example is presented in Fig. 2.14, the super cell containing up to 8860 atoms. Using the parameters presented in Fig. 2.13, the overall simulation time was 3.9 hours for a 260 x 180 pixels resolution images. The final image was averaged over 30 simulations, which is particularly used for quantitative STEM simulation (usually 5 averages are sufficient [43]).

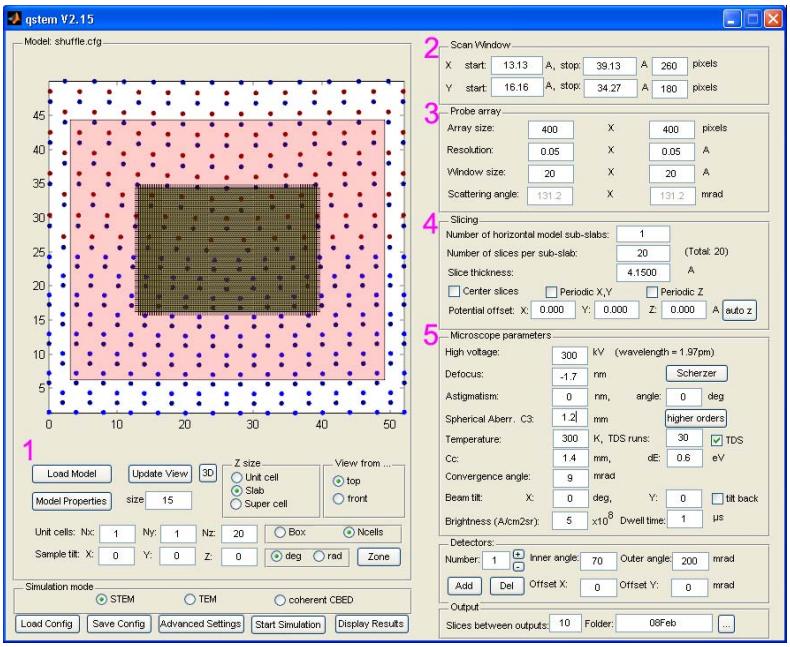

Figure 2.13 The graphical user interface of the QSTEM software, illustration of the simulation procedure and one example of the parameters used in this work.

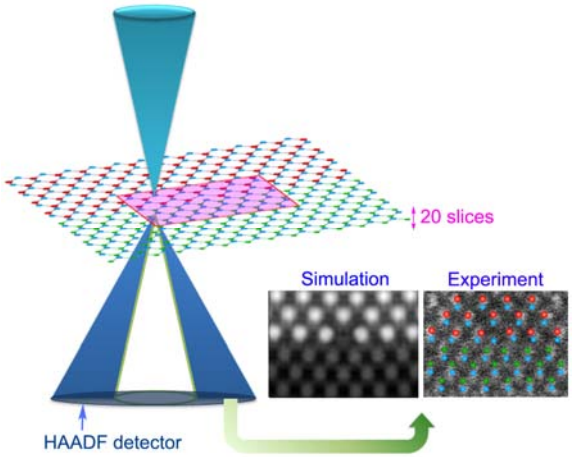

Figure 2.14 Schematic diagram of the HAADF simulation. The corresponding simulated and experimental images of a glide set Lomer dislocation are presented.

2.4 Geometrical phase analysis and dislocation density tensor

Recent advances in digital imaging and image-processing techniques, together with improved point-to-point resolution of microscopes have offered the possibility of locally determining the elastic strain of materials at nanometric scale using HRTEM images. Generally, two different approaches, Peak Finding [44] and Geometrical Phase Analysis (GPA) [45], are used. Both of them are based on the assumption that there is an apparent relationship between the local maxima or minima of the intensity and the local crystal structure [46]. However, this assumption is not always valid. In another word, the lattice fringes in an image may not faithfully coincide with the atomic plane position. It has long been known, for example, that in the case of off-axial imaging, lattice fringes shift due to thickness variation [47] and the measured lattice parameter depends on the gradient of the complex transfer function [48]. Image simulation for axial HRTEM show that the lattice spacings measured in thin multilayers depend on the imaging conditions [49, 50], particularly for non-centrosymmetric structures [51]. Hÿtch and Plamann give some useful rules for minimizing the errors [52]: (1) choosing conditions (thickness and defocus) where the fringe contrast is maximal, this is both to minimize the symmetry-breaking effects and to reduces the gradient of the effective lens transfer function; (2) avoiding regions where the fringe contrast changes rapidly; (3) carry out verification of displacement field using different reflection; (4) carry out the analysis at different defocus values.

To sum up, the peak finding method work in real space, superimposing a 2D reference lattice extrapolated from a non-distorted region of material to the experimental one, built up from the set of intensity maxima in the HRTEM image, and calculating the local discrete displacement field at each node. Then, by derivating the calculated displacement field, the strain field is obtained. Of course, such method is not applicable when the lattice periodicity is disturbed. Whereas, GPA works in Fourier space; it relies on the evaluation and interpretation of the geometric phase component $P_g(r)$ by performing a Fourier transform on a HRTEM image. For perfect crystals, the phase of a Bragg-reflection, described by the reciprocal space vector $\boldsymbol{g}$, is constant across the image. However, for a distorted lattice, small deformation can be seen as local lateral shifts of the lattice fringes and

consequently as small changes in the phase corresponding to ***g***. As this method is adequate for the analysis of images containing defect [53], I used it extensively during this work.

The phase $P_g(r)$ determined by GPA is related to the displacement field by the expression [45, 53]:

$$P_g(r) = -2\pi g \cdot u(r) \tag{2.8}$$

For a two dimensional lattice defined by the vectors g_1 and g_2,

$$P_{g_1}(r) = -2\pi g_1 \cdot u(r) = -2\pi\{g_{1x}u_x(r) + g_{1y}u_y(r)\} \tag{2.9 a}$$

$$P_{g_2}(r) = -2\pi g_2 \cdot u(r) = -2\pi\{g_{2x}u_x(r) + g_{2y}u_y(r)\} \tag{2.9 b}$$

where g_{1x} and g_{1y} are the k_x and k_y components (k being the variable in the reciprocal space) of the vector g_1, and $u_x(r)$ and $u_y(r)$ are the x and y components of the displacement field at position $r=(x, y)$ in the image.

These equations can be written in matrix form:

$$\begin{pmatrix} P_{g_1} \\ P_{g_2} \end{pmatrix} = -2\pi \begin{pmatrix} g_{1x} & g_{2x} \\ g_{2x} & g_{2y} \end{pmatrix} \begin{pmatrix} u_x \\ u_y \end{pmatrix} \tag{2.10}$$

where the relationship between the phase and the displacement field as a function of position in the image is more explicit. Then, the displacement field can be calculated by taking the inverse of the matrix containing the reciprocal lattice vectors:

$$\begin{pmatrix} u_x \\ u_y \end{pmatrix} = -2\pi \begin{pmatrix} g_{1x} & g_{2x} \\ g_{2x} & g_{2y} \end{pmatrix}^{-1} \begin{pmatrix} P_{g_1} \\ P_{g_2} \end{pmatrix} \tag{2.11}$$

From the local lattice displacements, the two-dimensional strain maps can then be calculated by differentiating the displacement field following the standard relations for strain analysis

$$\varepsilon_{xx} = \frac{\partial u_x}{\partial x} \tag{2.12 a}$$

$$\varepsilon_{xy} = \tfrac{1}{2}\left(\frac{\partial u_x}{\partial y} + \frac{\partial u_y}{\partial x}\right) \tag{2.12 b}$$

$$\varepsilon_{yx} = \tfrac{1}{2}\left(\frac{\partial u_y}{\partial x} + \frac{\partial u_x}{\partial y}\right) \tag{2.12 c}$$

$$\varepsilon_{yy} = \frac{\partial u_y}{\partial y} \qquad (2.12\ d)$$

And the lattice distortion field which is given by the gradient of the displacement field can be described by the following matrix

$$e = \begin{pmatrix} e_{xx} & e_{xy} \\ e_{yx} & e_{yy} \end{pmatrix} = \begin{pmatrix} \frac{\partial u_x}{\partial x} & \frac{\partial u_x}{\partial y} \\ \frac{\partial u_y}{\partial x} & \frac{\partial u_y}{\partial y} \end{pmatrix} \qquad (2.13)$$

the local in plane rigid body rotation, ω_{xy} is given by

$$\omega_{xy} = \tfrac{1}{2}\left(\frac{\partial u_y}{\partial x} - \frac{\partial u_x}{\partial y} \right) \qquad (2.14)$$

As suggested by Kret et al. [54] further differentiation of the determined lattice distortion field, one can get the dislocation density tensor (or Nye tensor analysis). It characterizes the strength of infinitesimal dislocation at each point in a continuously dislocated crystal and provides a measurement of the Burgers vector. It takes nonzero value only at dislocation core region [55]. The local Burgers vector is given by the line integral (closed curve around the dislocation) of the lattice distortion tensor [56] as well as the surface integral of the dislocation density tensor [54, 55]: $b = \iint_s a \cdot ds = -\oint_l e \cdot dl$, where surface S is bounded by a closed curve l, α and e are the dislocation density tensor and the lattice distortion tensor, respectively. In 2D, the components of the dislocation density tensor α_{xz} and α_{yz} are extracted from the strain tensor as follows [54]:

$$\alpha_{xz} = -\frac{\partial e_{xy}}{\partial x} + \frac{\partial e_{xx}}{\partial y} \qquad (2.15)$$

$$\alpha_{yz} = -\frac{\partial e_{yy}}{\partial x} + \frac{\partial e_{yx}}{\partial y} \qquad (2.16)$$

In TEM images, as we are working in 2D projection along the z axis, for simplicity we denote the 2D dislocation density tensor as α_x and α_y. In fact, the two in-plane components of the tensor field take zero values over the whole region except at the dislocation core position, where they form local peaks. Such peaks are surrounded by a zero-field within an accuracy of 10^{-6} times the densities reached at the core position [53].

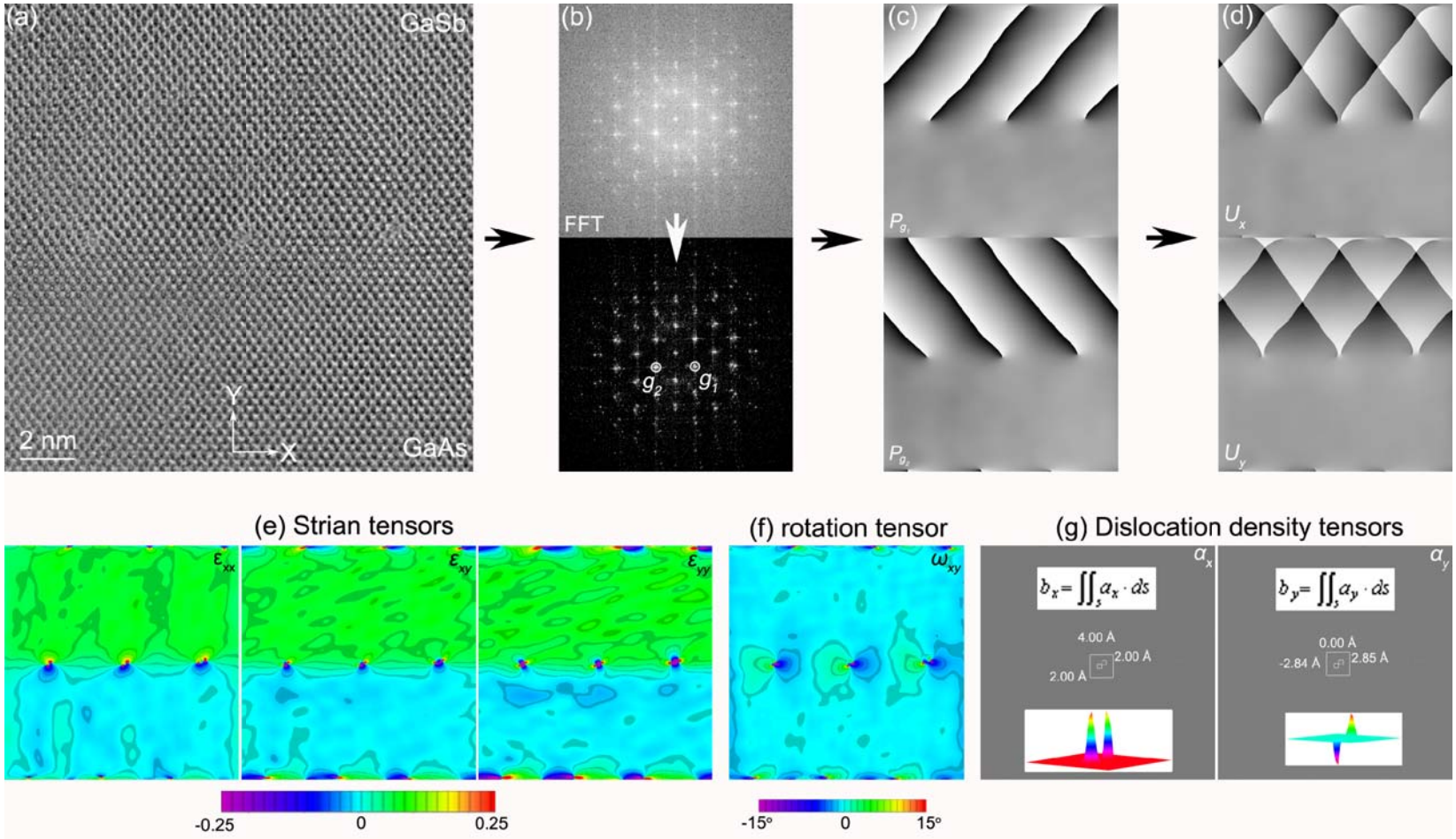

Figure 2.15 Illustration of the GPA procedure using GaSb on GaAs as an example: (a) HRTEM image of the GaSb/GaAs interface with 3 Lomer dislocations. (b) FFT of a and FFT after noise reduction, the red circle marks the selected reciprocal vectors. (c) the phase image for g_1 and g_2. (d) the corresponding displacement field. (e) and (f) the calculated strain tensors and rotation tensor ω_{xy}. (g) the dislocation density tensors and the insets show corresponding 3D map of the dislocation density tensor.

Figure 2.15 illustrate the GPA procedures, using the GaSb/GaAs interface with 3 misfit dislocations. During the image processing, the random noise was reduced by applying a Wiener filter in Fourier space, with fine background estimation. The phase images were obtained by applying Gaussian elliptic mask on (220) and ($2\bar{2}0$) reciprocal vectors. The calculated strain tensors, rotation tensor, and dislocation density tensors are presented in Fig. 2.15 (e), (f), and (g), respectively.

2.5 A summary of the theory of simple dislocations

Given the misfit dislocations formation mechanism as well as their energetic stability will be discuss, the basic knowledge of the dislocations should be recalled. Hence, several concepts and definitions of formalism of dislocations are provided. Then the elasticity theory is applied to describe the distortion, energy, and interaction of the dislocations. A detailed account can be found in "The theory of dislocations" by Hirth and Lothe [56].

2.5.1 Dislocations: edge and screw configurations

The periodicity of the atomic structures is broken if dislocations exist inside, the cores structures of dislocations may be complex for some lattice structures. Here, all of the considerations are clarified and illustrated with the cubic lattice. But the conclusions are suitable to other symmetric lattices. As schematically shown in Fig. 2.16, there are two elemental dislocations: edge and screw dislocations [56, 57].

(a) Edge dislocation

The edge dislocation can be viewed by inserting a half lattice plane into a crystal. The dislocation line corresponds to the position where the half-plane terminates. The Burgers vector b is then perpendicular to the dislocation line ξ.

(b) Screw dislocation

The screw dislocation can be constructed by shearing one part of the crystal with respect to the other one within a half-plane. The dislocation line is the line where the half-plane terminates. Burgers vector *b* is parallel to the dislocation line ξ.

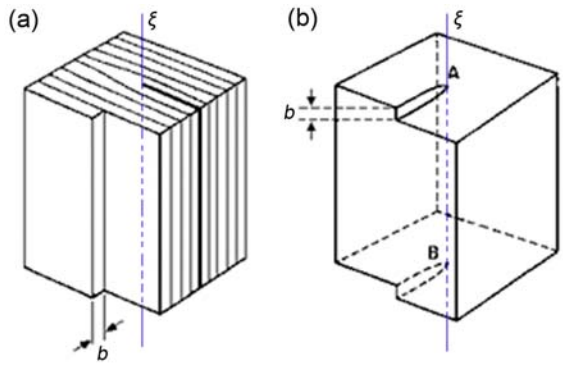

Figure 2.16: Schematic diagrams of edge and screw dislocation in a cubic lattice. The dislocation line ξ and Burgers vectors b are shown.

In addition, there are mixed type dislocations where the angle between the dislocation line and the Burgers vector can be in the range of 0 ~ 90 degrees. The mixed type dislocation can be decomposed into pure edge and screw type components. For simplicity, only the edge and screw type dislocations are discussed here.

2.5.2 Burgers vector

Within a continuum media description of the crystal, let *u(r)* be the displacement field of a small volume element from its original position after arbitrary elastic deformation. In an ideal crystal with an unlimited size, the arbitrary closed integral circuit over *u(r)* will always yield zero. However, for real crystals, structural defects with a line direction *l(r)* may exist, where the displacement *u* is integrated along an arbitrary circuits around the defect results in a non-zero vector:

$$\vec{b} = \oint \frac{\partial u}{\partial s} ds \qquad (2.17)$$

This non-zero vector is the so-called Burgers vector b of the linear defect. The linear defects with $b \neq 0$ are dislocations. Since in a crystal, the atoms periodically arrange following special lattice translation vector, Burges vector can't be arbitrary, but restricted by the lattice structure. If the integration path only encircles the dislocation and runs through other perfect lattices, Burgers vector has to be a linear combination of the lattice translation vector. Alternatively, partial dislocations have Burgers vector with a fraction of lattice translation vectors. Partial dislocations are accompanied by a secondary structural defect such as stacking fault.

2.5.3 The Stress field of a straight dislocation

The long-range elastic strain field of a dislocation can be described by the linear elasticity theory. The corresponding elastic strain energy of an isolated straight dislocation and the interaction force of two straight dislocations will be provided here.

(a) Edge dislocation

As schematically shown in Fig. 2.17 (a), an unstrained isotropic cylinder orientates along z axis, and a shear displacement $u(r)$ is applied above the half-space with $y>0$ along x direction for constructing the edge dislocation. After that, the edge dislocation induces the planar strain into the surrounding medium with the displacement field $u_z = 0$ and $\partial u_i / \partial z = 0$. In such case, the non-zero stress components are

$$\sigma_{xx} = -\frac{\mu|b|}{2\pi(1-\nu)} \frac{y(3x^2 + y^2)}{(x^2 + y^2)^2}, \qquad (2.18\ a)$$

$$\sigma_{yy} = \frac{\mu|b|}{2\pi(1-\nu)} \frac{y(x^2 - y^2)}{(x^2 + y^2)^2}, \qquad (2.18\ b)$$

$$\sigma_{xy} = \frac{\mu|b|}{2\pi(1-\nu)} \frac{x(x^2 - y^2)}{(x^2 + y^2)^2}, \qquad (2.18\ c)$$

$$\sigma_{zz} = \nu\left(\sigma_{xx} + \sigma_{yy}\right) = \frac{\mu|b|\nu}{\pi(1-\nu)}\frac{y}{x^2+y^2} \ . \qquad (2.18\ d)$$

where μ is the shear modulus, ν is the Poison's ratio.

With the stress expressions, the displacements can be derived from Eq. (2.18) by integration and the boundary condition of u_l=0 at y=0:

$$u_x = \frac{|b|}{2\pi}\left[\arctan\frac{y}{x} + \frac{xy}{2(1-\nu)(x^2+y^2)}\right], \qquad (2.19\ a)$$

$$u_y = -\frac{|b|}{2\pi}\left[\frac{1-2\nu}{4(1-\nu)}\ln\left(x^2+y^2\right) + \frac{x^2-y^2}{4(1-\nu)(x^2+y^2)}\right]. \qquad (2.19\ b)$$

(b) Screw dislocation

As schematically illustrated in Fig.2.17 (b), let the dislocation line be along z axis. The elastic field in the dislocated cylinder can be found by direct inspection. First, it is noted that there are no displacements in the x and y directions: $u_x = u_y = 0$

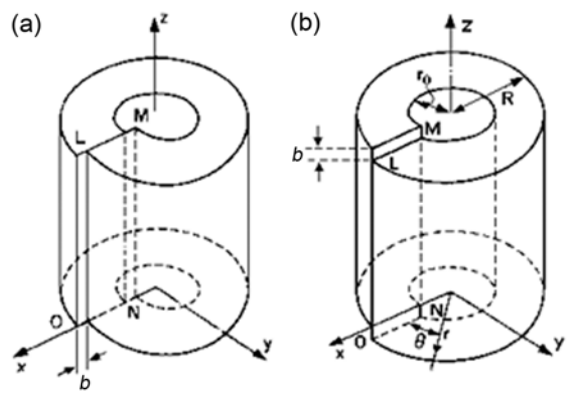

Figure 2.17: Illustrations of the elastic distortion of a cylindrical ring produced by the edge and screw dislocations, respectively.

Secondly, the displacement in the z direction increases uniformly from zero to b as θ increase for 0 to 2π, as shown in Fig. 2.17 (b):

$$u_z = \frac{b\theta}{2\pi} = \frac{b}{2\pi}\arctan\left(\frac{y}{x}\right) \qquad (2.20)$$

The strain field will be

$$\varepsilon_{xz} = \varepsilon_{zx} = -\frac{b}{4\pi}\frac{y}{x^2+y^2} \qquad (2.21\ a)$$

$$\varepsilon_{yz} = \varepsilon_{zy} = \frac{b}{4\pi}\frac{x}{x^2+y^2} \qquad (2.21\ b)$$

The expressions in the cylindrical coordinates are

$$\varepsilon_{\theta z} = \varepsilon_{z\theta} = \frac{|b|}{4\pi}\frac{1}{r}. \qquad (2.\ 22a)$$

According to the Hooke's law for an isotropic medium, the stress components will be

$$\sigma_{\theta z} = \sigma_{z\theta} = \frac{\mu|b|}{2\pi}\frac{1}{r} \qquad (2.22\ a)$$

2.5.4 The strain energy of a dislocation

According to elasticity theory [56], when a unit volume element deforms reversibly by differential strain incensement $d\varepsilon_{ij}$, the stress σ_{ij} acts on the element by $de = \sigma_{ij} d\varepsilon_{ij} = c_{ijkl}\varepsilon_{kl} d\varepsilon_{ij}$, where c_{ijkl} are elastic constants. Integrating this equation we obtain the strain energy density: $e = \frac{1}{2} c_{ijkl}\varepsilon_{ij}\varepsilon_{kl} = \frac{1}{2}\sigma_{ij}\varepsilon_{kl}$. Now, we apply this equation on the simple dislocations.

(a) Edge dislocation

The strain energy density is

$$e_s = \frac{1}{2}\sigma_{ij}\varepsilon_{kl} = \frac{1}{2\pi}\left[\frac{1}{2\mu}\sigma_{xy}^2 + \frac{1}{2E}\left(\sigma_{xx}^2 + \sigma_{yy}^2 - 2\nu\sigma_{xx}\sigma_{yy} - \sigma_{zz}^2\right)\right]. \qquad (2.23)$$

The strain energy per unit length of the edge dislocation in an infinite medium is obtained by integrating the strain energy density in the regions between two coaxial cylinders with radius r_1 and r_2, centered on the dislocation line:

$$E(r_1, r_2) = \int_{r_1}^{r_2}\int_0^{2\pi} e_s(r) 2\pi r dr d\theta = \frac{\mu|b|^2}{4\pi(1-\nu)}\ln\left(\frac{r_2}{r_1}\right), \qquad (2.24)$$

Where r_1 and r_2 are the radius of the inner and outer cylinder, respectively. Obviously, the expression diverges at the limits $r_2 \to \infty$ and $r_1 \to 0$. The former divergence means that the strain field of a dislocation is long-range and the strain energy increases as a function of the medium size. The latter divergence indicates that the continuum elasticity theory breaks down in the dislocation core region and cannot correctly describe the discrete atomic structure. Therefore, the core radius r_c is introduced to characterize the size of the core region. In the region $r \geq r_c$ the continuum elasticity theory is valid to describe the strain field and energy associated with the dislocation. Correspondingly, the core energy E_c is defined as the energy stored inside of the cylinder with the radius r_c. With the introduction of E_c, the strain energy $E(r)$ is linearly dependent on the logarithmic value of the cylinder radius r and the energy per unit length of the dislocation line is expressed as

$$E(r) = \frac{\mu |b|^2}{4\pi(1-\nu)} \ln\left(\frac{r}{r_c}\right) + E_c, \quad r \geq r_c, \tag{2.25}$$

According to Eq. (2.25), the core radius is practically determined as the value from which $E(r)$ linearly varies with $\ln(r)$.

(b) Screw dislocation

This stress field of the screw dislocation is self-stress. The strain energy density is

$$e_s(r) = \frac{1}{2} c_{ijkl}\varepsilon_{ij}\varepsilon_{kl} = \frac{1}{2}\sigma_{ij}\varepsilon_{kl} = \frac{1}{2}\left(\sigma_{\theta z}\varepsilon_{z\theta} + \sigma_{z\theta}\varepsilon_{\theta z}\right) = \frac{\mu |b|^2}{8\pi^2}\frac{1}{r_2}. \tag{2.26}$$

Similar to the edge dislocation, the strain energy per unit length of the screw dislocation between coaxial cylinders centering the dislocation line is

$$E(r_1, r_2) = \int_{r_1}^{r_2} e_s(r) 2\pi r dr = \frac{\mu |b|^2}{4\pi} \ln\left(\frac{r_2}{r_1}\right). \tag{2.27}$$

Comparing with the edge dislocation, $E(r_1, r_2)$ of the screw dislocation is only different by the term $1/(1-\nu)$. As a function of the logarithmic value of the cylinder radius r, the strain $E(r)$ per unit length of the dislocation line is:

$$E(r) = \frac{\mu |b|^2}{4\pi} \ln\left(\frac{r}{r_c}\right) + E_c, \; r \geq r_c. \tag{2.28}$$

(c) Mixed type dislocation

In the linear theory, the results for the screw and edge dislocations can be superimposed to describe a mixed dislocation. Let the angle between the Burgers vector and the dislocation line be β for the mixed dislocation, then the screw component of the vector is projected as $|b|\cos\beta$ and the edge component is $|b|\sin\beta$. The superposition provides the energy of the general straight dislocation:

$$E(r) = k(\beta)\frac{|b|^2}{4\pi} \ln\left(\frac{r}{r_c}\right) + E_c, \; r \geq r_c, \tag{2.29}$$

where $k(\beta)$ is the energy factor, which describes the variation of the strain energy with the distance r, it is defined as:

$$k(\beta) = \mu\left(\cos^2\beta + \frac{\sin^2\beta}{1-\nu}\right). \tag{2.30}$$

2.5.5 Elastic interaction between dislocations

In Chapter 4, we shall need to know the force between the dislocation on growing surface and the one locating at the interface. Therefore, the interaction between dislocations needs to be considered; without going into the details, the dislocation 2 at the surface will be in the stress field generated by the dislocation 1. Then the force on the dislocation 2 in this stress field will be given by [56]

$$f = (b \cdot \sigma_b) \times \xi \tag{2.31}$$

Where b is the Burgers vector of dislocation 2, ξ is unit length of the dislocation along the dislocation line, and σ_b is the stress on the plane normal to the Burgers vector, and on which b points outwards.

2.6 Molecular Dynamic Simulation

Based on classical mechanics and statistical theory, Molecular Dynamics (MD) investigates the static and dynamic properties of systems described by the empirical potentials with the aid of numerical calculation techniques. Although they lack the accuracy of the first principle calculations, the empirical potentials are computationally simple and fast, so that MD can handle much larger systems and longer time span. Usually, the detailed expressions of empirical potentials have an analytical formula and can be uniquely determined by several adjustable parameters. The force on atoms can be directly deduced from these empirical potentials. Let the empirical potential between atoms be $V(r_1, r_2, \cdots, r_N)$, then the interacting force on the i th atom and the corresponding motion equation are expressed as

$$F_i = m_i \frac{d^2 r_i}{dt^2} = -\nabla_i V(r_1, r_2, \cdots, r_N) \qquad (2.32)$$

MD simulation based on empirical potentials cannot provide any information about the electron in structures, but gives the atomic structures and the corresponding thermodynamic properties of the matter; it can also provide a high resolution scan about the time and space for the dynamic process taking place in the systems. Thus MD methods are very useful to investigate the systems with large size and long-time dynamics.

For semiconductors, the most successful approaches to develop many-body empirical potentials are those of Keating [58], Stillinger-Weber [59], and Tersoff [60]. In this thesis, the Stillinger-Weber potential has been adopted. The Stillinger-Weber potential has initially introduced the angular-dependence interaction as the triplet term for the study of the liquid silicon phases [59]. Soon, it has been fitted to a number of chemical elements, including the group IV semiconductors [61, 62] and

their binaries [63] and III-V compounds [64-67]. The total potential is truncated to the two- and three-body terms with the short-range interaction restricted between the first and second nearest neighbors:

$$V(r_1, r_2, \cdots, r_N) = \sum_{i,j(i\langle j)}^{N} v_2(r_i, r_j) + \sum_{i,j,k(i\langle j\langle k)}^{N} v_3(r_i, r_j, r_k), \tag{2.33}$$

where

$$v_2(r_i, r_j) = \varepsilon f_2(r_{ij}/\sigma), \tag{2.34}$$

$$v_3(r_i, r_j, r_k) = \varepsilon f_3(r_i/\sigma, r_j/\sigma, r_k/\sigma) \tag{2.35}$$

And f_2, f_3 are expressed as

$$f_2(r) = \begin{cases} A(B/r^{-p} - r^{-q})\exp[1/(r-a)] & \mathrm{r < a} \\ 0 & \mathrm{r > a} \end{cases}, \tag{2. 36}$$

$$f_3(r_i, r_i, r_k) = h(r_{ij}, r_{jk}, \theta_{ijk}) + h(r_{ji}, r_{ik}, \theta_{jik}) + h(r_{jk}, r_{ik}, \theta_{ikj}) \tag{2.37}$$

$$h(r_{ij}, r_{jk}, \theta_{ijk}) = \lambda \exp[\gamma/(r_{ij} - a) + \gamma/(r_{jk} - a)](\cos\theta_{ijk} + 1/3)^2 \tag{2.38}$$

Here r_{ij} is the distance between i, j atoms and $r_{ij} = |r_j - r_i|$. ε and σ are the energy and length units, respectively. ε is chosen to make f_2 equal to -1, and σ is chosen to make $f_2'(2^{1/6})$ vanish. a represents the cutoff distance and determines the interaction range of the Stillinger-Weber potential. Usually, a is set to some value between the first and second nearest neighbours according to the features of the angular term in the three-body interaction. This potential is consequently limited to the first nearest neighbours (4 for tetrahedral semiconductors). θ_{ijk} is the angle between the r_{ij} and r_{jk} bonds subtended at vertex j atom. A, B, λ, and γ are the bond strength factors.

In this study, we used the parameters of Stillinger-Weber potential reported by Ichimura [64] and Wang et al. [68]. Besides the normal bonds Ga-As, Ga-P, and Ga-Sb, the wrong bonds Ga-Ga, P-P, and Sb-Sb have also been considered. Since there were no proper valid parameters available for the wrong bonds, as already done by Zhou et al. [69], we adopted the parameter of GaAs to replace them. Here we summrize the parameters of stillinger-Weber potention used in this study in Tab. 2.2.

Table 2.2 Parameters of Stillinger-Weber potential used in the simulation [64, 68]

bond	d (Å)	ε (eV)	A	B	δ (Å)	λ
Ga-P	2.36	1.78	7.62333	0.681	2.0642	29.57
Ga-Sb	2.64	1.48	7.91549	0.720	2.2900	32.49
Ga-Ga	2.44	1.63	5.9768	0.5860	2.183	21
As-As	2.50	1.63	6.8553	0.6711	2.183	21

The Lomer misfit dislocation is constructed in a series of supercells with variant size in *xy* plane ((001) plane), 26a x 26a for GaSb and 28a x 28a for GaAs (a: corresponding lattice constant for GaAs and GaSb), respectively, the supercells made up by 20 monolayers GaSb sandwiched between two 20 monolayers GaAs along the *z* direction, they contain 89760 atoms. The relaxation procedures are performed using the quench algorithm [22, 70]. All along the relaxation, a kinetic temperature is calculated at each step and the relaxation is stopped when the system kinetic temperature is lower than 10^{-8} K.

Besides the total energy of the relaxed structure, the MD calculations provide also the total energy projected onto a single atom j, which enables us to calculate the core energy of dislocation. The energy of the single atom j is then defined as the difference between the total energy E_{tot}^{j} and the total energy of the same type of atom in perfect material E_{tot}^{bulk} : $E_{f}^{j} = E_{tot}^{j} - E_{tot}^{bulk}$. E_{tot}^{bulk} is determined in a bulk like super-cell cluster of same shape as the model with the dislocation.

References

[1]A. Y. Cho and J. R. Arthur, Progress in Solid State Chemistry **10, Part 3**, 157 (1975).

[2]M. A. Herman and H. Sitter, *Molecular Beam Epitaxy: Fundamentals and Current Status*, 2nd ed. (Springer-Verlag, 1996).

[3]Wikipedia: http://en.wikipedia.org/wiki/Molecular_beam_epitaxy.

[4] http://www.first-tonomura-pj.net/e/commentary/mechanism/index.html.

[5]R.F.Egerton, *Physical Principles of Electron Microscopy*, 2nd ed. (Springer, 2005).

[6]Wikipedia: http://en.wikipedia.org/wiki/Transmission_electron_microscopy.

[7]M.E.Haine, and V.E.Cosslett, Journal of Pharmaceutical Sciences **50**, 979 (1961).

[8]O. Scherzer, Optik **2**, 114 (1947).

[9]A.V. Crewe, Optik **60**, 271 (1982).

[10]H. Rose, Optik **85**, 19 (1990).

[11]M. Haider, S. Uhlemann, E. Schwan, H. Rose, B. Kabius, and K. Urban, Nature **392**, 768 (1998).

[12]O. L. Krivanek, N. Dellby, A. J. Spence, R. A. Camps, and l. M. Brown, Inst. Phys. Conf. Ser. **153**, 35 (1997).

[13]H. H. Rose, Sci.Technol. Adv. Mater. **9**, 014107 (2008).

[14]U. Dahmen, R. Erni, V. Radmilovic, C. Ksielowski, M.-D. Rossell, and P. Denes, Phil. Trans.R. Soc.A 367, 3798 (2009).

[15]N. Alem, O. V. Yazyev, C. Kisielowski, P. Denes, U. Dahmen, P. Hartel, M. Haider, M. Bischoff, B. Jiang, S. G. Louie, and A. Zettl, Phys. Rev. Lett. **106**, 126102 (2011).

[16]Ernst Ruska Centre for Microscopy, http://www.er-c.org/centre/micfac/frames/titanp.htm.

[17]M. Haider, H. Müller, S. Uhlemann, J. Zach, U. Loebau, and R. Hoeschen, Ultramicroscopy **108**, 167 (2008).

[18]C. Kisielowski, B. Freitag, M. Bischoff, H. van Lin, S. Lazar, G. Knippels, P. Tiemeijer, M. van der Stam, S. von Harrach, M. Stekelenburg, M. Haider, S. Uhlemann, H. Müller, P. Hartel, B. Kabius, D. Miller, I. Petrov, E. a. Olson, T. Donchev, E. a. Kenik, A. r. Lupini, J. Bentley, S. J. Pennycook, I. m. Anderson, A. m. Minor, A. k. Schmid, T. Duden, V. Radmilovic, Q. m. Ramasse, M. Watanabe, R. Erni, E. a. Stach, P. Denes, and U. Dahmen, Microsc. Microanal. **14**, 469 (2008).

[19] W. L. Bragg, Proceedings of the Cambridge Philosophical Society **17**, 43–57 (1914).

[20]D. B. Williams and C. B. Carter, *Transmission Electron Microscopy: a Textbook for Materials Science* (Springer, 1996).

[21]L. A. Tietz, C. Barry Carter, and S. McKernan, Ultramicroscopy **60**, 241(1995).

[22]Y. Wang, P. Ruterana, H. P. Lei, J. Chen, S. Kret, S. El Kazzi, L. Desplanque, and X. Wallart, J. Appl. Phys. **110**, 043509 (2011).

[23]K. W. Urban, Nature Mater. **8**, 260 (2009).

[24]A. I. Kirkland, and R. R. Meyer, Microsc. Microanal. **10**, 401 (2004).

[25]O. Michael A., Ultramicroscopy **47**, 282 (1992).

[26]L. Houben, A. Thust, and K. Urban, Ultramicroscopy **106**, 200 (2006).

[27]U. Dahmen, Microsc. Microanal. **13**, 1150 (2007).

[28]C. L. Jia, M. Lentzen, and K. Urban, Science **299**, 870 (2003).

[29]M. Lentzen, B. Jahnen, C. L. Jia, A. Thust, K. Tillmann, and K. Urban, Ultramicroscopy **92**, 233 (2002).

[30]C.-L. Jia, M. Lentzen, and K. Urban, Microsc. Microanal. **10**, 174 (2004).

[31]K. W. Urban, Science **321**, 506 (2008).

[32]M. Lentzen, Microsc. Microanal. **12**, 191 (2006).

[33]Z. Zhang and U. Kaiser, Ultramicroscopy **109**, 1114 (2009).

[34]M. Bosman, V. J. Keast, J. L. García-Muñoz, A. J. D'Alfonso, S. D. Findlay, and L. J. Allen, Phys. Rev. Lett. **99**, 086102 (2007).

[35]D. A. Muller, L. F. Kourkoutis, M. Murfitt, J. H. Song, H. Y. Hwang, J. Silcox, N. Dellby, and O. L. Krivanek, Science **319**, 1073 (2008).

[36]P. D. Nellist and S. J. Pennycook, J. Microsc. **190**, 159 (1998).

[37]S.J. Pennycook, Advances in Image and Electron Physics **123**, 173 (2002).

[38]O. Scherzer, J. Appl. Phys. **20**, 20 (1949).

[39]S.J.Pennycook and P.D.Nellist, *Scanning Transmission Electron Microscopy: Imaging and Analysis*, (Springer, 2011).

[40]B. F. Buxton, J. E. Loveluck, and J. W. Steeds, Philos. Mag. A **38**, 259 (1978).

[41]E. Carlino and V. Grillo, Phys. Rev. B **71**, 235303 (2005).

[42]C. T. Koch, *Determination of Core Structure Periodicity and Point Defect Density Along Dislocations*, Arizona State University, 2002.

[43]Christoph Koch's Webpage: http://www.christophtkoch.com/stem/index.html.

[44]S. Kret, C. Delamarre, J. Y. Laval, and A. Dubon, Philos. Mag. Lett. **77**, 249 (1998).

[45]M. J. Hÿtch, E. Snoeck, and R. Kilaas, Ultramicroscopy **74**, 131 (1998).

[46]R. Bierwolf, M. Hohenstein, F. Phillipp, O. Brandt, G. E. Crook, and K. Ploog, Ultramicroscopy **49**, 273 (1993).

[47]P. B. Hirsch, *Electron Microscopy of Thin Crystals* (R. E. Krieger Pub. Co., 1977).

[48]J. C. H. Spence, J. M. Cowley, and R. Gronsky, Ultramicroscopy **4**, 429–433 (1979).

[49]T.Walther and C. J. Humphreys, Inst Phys Conf Ser **147**, 103 (1995).

[50] P. Bayle-Guillemaud and J. Thibault, Microsc. Microanal. **8**, 125 (1997).

[51] K. Tillmann, M. Lentzen, and R. Rosenfeld, Ultramicroscopy **83**, 111–128 (2000).

[52] M. J. Hÿtch and T. Plamann, Ultramicroscopy **87**, 199 (2001).

[53] S. Kret, P. Ruterana, A. Rosenauer, and D. Gerthsen, Phys. Status Solidi B **227**, 247 (2001).

[54]S. Kret, PawelDlużewski, P. Dlużewski, and E. Sobczak, J. Phys.: Condens. Matter **12**, 10313 (2000).

[55]J.F. Nye, Acta Meter. **1**, 153 (1953).

[56]J. P. Hirth and J. Lothe, *Theory of Dislocations* (Krieger Pub. Co., 1982).

[57]D. Hull and D. J. Bacon, *Introduction to Dislocations* (Elsevier, 2011).

[58]P. N. Keating, Phys. Rev. **145**, 637 (1966).

[59]F. H. Stillinger and T. A. Weber, Phys. Rev. B **31**, 5262 (1985).

[60]J. Tersoff, Phys. Rev. Lett. **56**, 632 (1986).

[61]K. Ding and H. C. Andersen, Phys. Rev. B **34**, 6987 (1986).

[62]S. Skokov, C. S. Carmer, B. Weiner, and M. Frenklach, Phys. Rev. B **49**, 5662 (1994).

[63]M. Laradji, D. P. Landau, and B. Dünweg, Phys. Rev. B **51**, 4894 (1995).

[64]M. Ichimura, Phys. Status Solidi A **153**, 431 (1996).

[65]D. Maroudas, L. A. Zepeda-Ruiz, and W. H. Weinberg, Surf. Sci. **411**, L865 (1998).

[66]P. Ruterana, B. Barbaray, A. Béré, P. Vermaut, A. Hairie, E. Paumier, G. Nouet, A. Salvador, A. Botchkarev, and H. Morkoç, Phys. Rev. B **59**, 15917 (1999).

[67]A. Béré and A. Serra, Philos. Mag. **86**, 2159 (2006).

[68]Z. Q. Wang and D. Stroud, Phys. Rev. B **42**, 5353 (1990).

[69]X. Zhou, J. Zhao, X. Chen, and W. Lu, Phys. Rev. A **72**, 053203 (2005).

[70]H. Lei, J. Chen, and P. Ruterana, J. Appl. Phys. **108**, 103503 (2010).

Chapter 3

The growth optimization of GaSb on GaAs and GaP substrate

Metamorphic epitaxy of high lattice-mismatch Sb-based materials on GaAs is attracting much attention for potential applications in electronic and optoelectronic devices due to their unique band-structure alignments, small electron effective mass and high electron mobility [1-3]. With the large mismatch (7.8%) between GaSb and GaAs, the critical thickness is expected to be within the range of a few monolayers and the growth mode should theoretically correspond to the 3D Volmer-Weber with formation of relaxed islands [4] which subsequently coalesce to give rise to the epilayer [5]. The classical mechanism of relaxation should be the generation of 60° dislocations at island surface, followed by their glide to the interface and subsequent reaction to form 90° Lomer dislocations which should be the most efficient defects for the strain relief [6, 7]. This growth mode has been largely investigated during the last decades and one of the representatives has been the GaAs/Si with the aim of optoelectronic integration in the Si technology [8]. In these reports, both 90° and 60° misfit dislocations were present at the interfaces subsequent to the island coalescence [9-11]. Afterwards, many parameters govern the crystalline quality of the epitaxial layer, some of them are the island size distribution, their state of relaxation (number and type of underlying misfit dislocations), mutual islands orientation, etc, ... Such parameters are not easily controlled, they are expected to depend on the mismatch between the epitaxial layer and the substrate, the growth conditions (temperature, method, growth kinetics, surfactants). Early reports showed that low strain systems <2% resulted in 60° dislocations, moderate strain (3–4%) in mixed Lomer and 60° dislocations, and high strain >6% in pure Lomer [12]. It has also been shown that the growth temperature strongly determines the type of misfit dislocations which is produced, with GaSb grown at 520 °C giving rise to 90° misfits and 560 °C favoring 60° dislocations [13, 14]. Recently, it was claimed that particular growth conditions can be tuned for the formation of 90° rather than 60° misfit dislocations, which seems to require balancing of strain energy with adatom migration, Sb overpressure, and growth temperature. A

demonstration was provided for a highly periodic array of 90° misfit dislocation based growth of GaSb on GaAs to yield almost completely (~98%) relaxed and low dislocation density in the GaSb layers on GaAs (~$7x10^5cm^{-2}$) [15].

In this chapter, we have made extensive exploration to optimize the growth parameters. A systematical investigation of the relationship between the growth parameters and the misfit dislocations is presented. More specifically, we have grown GaSb on GaAs substrate with different AlSb interlayer thickness to investigate the influence of AlSb interlayer thickness on the threading dislocation density, misfit dislocation, and strain relaxation. Besides the AlSb interlayer, the influence of the substrate surface reconstruction was also investigated. On GaP substrate, we focus on the strain relaxation and misfit dislocations at the initial growth step and a detailed growth optimization process is discussed. Besides the substrate surface treatment, the influence of the growth rate and growth temperature on the strain relaxation of GaSb islands is investigated. The threading dislocation density and strain relaxation in the thick GaSb epitaxy layer (600 nm) is next studied. Finally, an AlSb/InAs hetero-structure was fabricated on GaSb and GaP substrate with a 600 nm thick GaSb buffer layer grown using the optimized growth parameters.

3.1Threading dislocation density and strain relief in GaSb/GaAs versus substrate treatment and AlSb thickness

3.1.1 Introduction

Huang et al recently report that a careful monitoring of the GaAs reconstruction and initial with a Sb rich (2x8) surface construction may lead to direct nucleation of a Lomer dislocations network at the interface and to a two dimensional (2D) almost defect free GaSb layer at 510 ^oC by molecular beam epitaxy (MBE). Interestingly, this low threading dislocation density was claimed to be attained subsequent to a planar growth mode established after only 3 monolayers of GaSb [15]. Using this optimized growth mode, laser

emission in the infrared has been demonstrated [16]. In the same vein, several research groups have reported that the insertion of AlSb interfacial monolayers should be able to improve GaSb layer quality on various substrates, such as Si [17-19] and GaAs [20, 21] with a suggested better relief of the strain for the smallest AlSb thickness [21, 22]. Although these studies are of interest for understanding the role of AlSb buffer, few reports were issued on the atomic structure of the interfaces, and any is hardly available on the strain relaxation at the nanometer scale taking into account the types of the misfit dislocations.

In this section, a detailed investigation of the misfit dislocation structure and interface local strain relaxation under the influence of surface treatment and AlSb interlayer is presented.

3.1.2 Samples

Five samples were chosen for this study. The GaSb layer thickness was 600 nm, the structure of the samples is schematically shown in Fig. 3.1. After smoothing the substrate surface, the As valve was closed and the sample temperature was decreased to 510°C under Sb_2 flux for sample B and D and without any flux for samples A, C, and E. For these latter samples, we waited until the reactor pressure has reached the 10^{-9} Torr range before continuing the growth. For samples C and E, an AlSb layer was inserted between the GaAs buffer and the GaSb layer. The deposition was started by 1 monolayer (ML) Al followed by 3 ML AlSb (sample C) and 16 ML AlSb (sample E). For sample A, 1 ML Ga was deposited before growing the GaSb layer. For sample B, GaSb layer was directly grown on the Sb treated

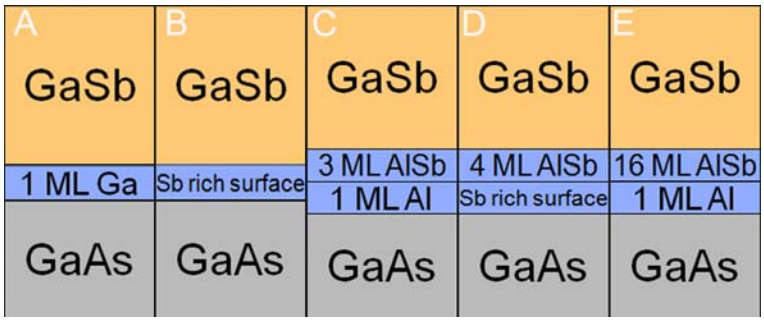

Figure 3.1 Schematic diagrams of the layout of the five investigated samples, the GaSb layers thickness are 600 nm.

GaAs substrate. For sample D, 4 ML AlSb were inserted between the GaAs buffer and GaSb layer. The growth rate was 0.7 ML/s for the antimonide layers; the growth process was monitored by in situ reflection high-energy electron diffraction (RHEED). The Sb_2 exposure during cooling of the GaAs buffer leads to a (2x8) RHEED pattern whereas for the other samples the starting reconstruction was (2x4).

3.1.3 Results

Cross-sectional, plan view and high-resolution TEM investigations were made in order to analyze the interface dislocations, the AlSb interlayers and the resulting GaSb crystalline quality. Fig. 3.2 (a) and (b) show the cross-sectional micrographs of samples C and E, respectively. As can be noticed, threading dislocations are generated at the interface between the GaSb epitaxial layer and GaAs substrate, some of them cross the whole epitaxial layer, whereas others have their lines cut during the sample preparation.

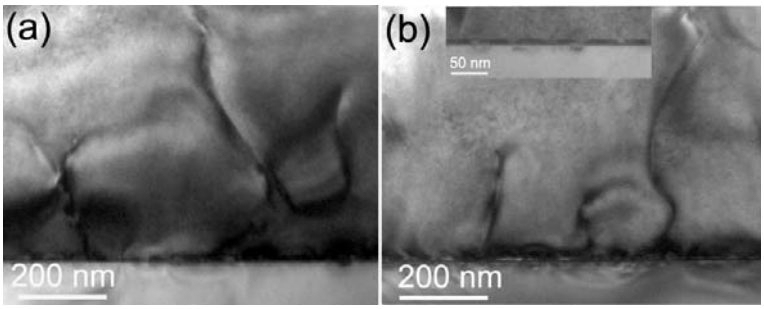

Figure 3.2 Cross-sectional bright-field TEM images of sample C and E. The insert in (b) is a enlarge view of the interface showing the morphology of AlSb buffer.

Such observation cannot be used to state that the dislocation density decreases with the increase of the epitaxial layer thickness. In addition, as the dislocations have a/2 <110> Burgers vectors some of them will be out of contrast in observations carried out in cross sections along <110> type zone axis. Therefore, in order to determine the dislocation density, we have carried out plan view observations along the [001] zone axis. Indeed, it may also be taken into account that a reduction of dislocation density may occur due to interactions and annihilations which take place mostly close to the interface with the substrate where the density is still very high. Another important feature of Fig. 3.2 (b) needs to be pointed out: the

contrast at the interface reveals the morphology of the AlSb interlayer, especially for sample E as shown in the inset of Fig. 3.2 (b) where the layer is clearly delineated and continuous.

Figure 3.3 shows plan-view TEM micrographs of sample B, C, D: the threading dislocations appear as dark dots/lines on the shiny GaSb background. The averaged threading dislocations estimated from more

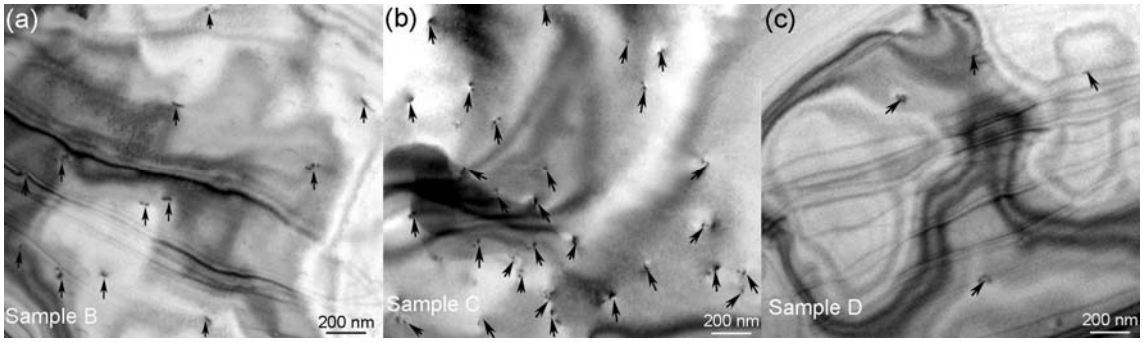

Figure 3.3 Plan-view TEM images of Sample B, C, and D, recorded close to the [001] growth axis.

than 10 images for each sample are summarized in Tab. 3.1, i.e. 7.5×10^8, 2.2×10^8, 8.7×10^8, 6.4×10^7, and 7.1×10^8 threading dislocations/cm^2 for samples A, B, C, D, and E, respectively. Obviously, sample D, for which the 4 ML AlSb growth was initiated on a Sb-rich GaAs surface, exhibits the lowest threading dislocation density and the others almost stay in the same level. An interesting question is if this comes from a particular atomic structure at the interface. Indeed, it has been claimed that the formation of misfit

Table 3. 1 Interface structure data for the investigated sampes.

	Sample A	Sample B	Sample C	Sample D	Sample E
Layers of AlSb (ML)	0	0	3	4	16
TD density (10^8 cm^{-2})	7.5	2.2	8.7	0.64	7.1
60° dislocation	10 %	0	17.4 %	0	5.6 %
Spacing of Lomer (nm)	5.7 ± 0.2	5.5± 0.01	5.3 ± 0.7	5.5 ± 0.1	5.6 ± 0.3
Thickness of interface (nm)	2.12	0.95	2.02	0.70	1.14
Pure Lomer dislocation	64.7 %	93.5 %	68.4 %	100 %	75.8 %

arrays of Lomer dislocations contribute to strongly decrease the threading dislocation densities [3, 15, 22]. In order to check this, we have carried out a detailed HRTEM analysis of these samples; the results are discussed in the next sections.

Fig. 3.4 shows HRTEM images of the (110) interface between the GaSb epitiaxial layer and GaAs substrate for sample A (a) and B (b). In these images, the positions of the interface dislocations have been marked by the additional {111} lattice planes (inclined arrows). As the lattice constant of GaSb is larger than that of the GaAs substrate, the extra half planes of the misfit dislocations are observed in the GaAs substrate. Lomer dislocations and closely spaced 60° dislocation pairs can be seen along the interface. These are the major interfacial defects which accommodate the misfit strain. If we take the interface as the line which is defined by the location of the dislocations (inclined arrows), in sample A, the misfit dislocations are essentially made of 60° dislocation pairs of which one is in the epitaxial layer, the second in the substrate. In contrast, all the extra {111} planes terminate at the interface and Lomer dislocations are the major misfit dislocation at the interface in sample B. To analyze the local strain distribution at the interface, we have used the GPA [26, 27] on the HRTEM images.

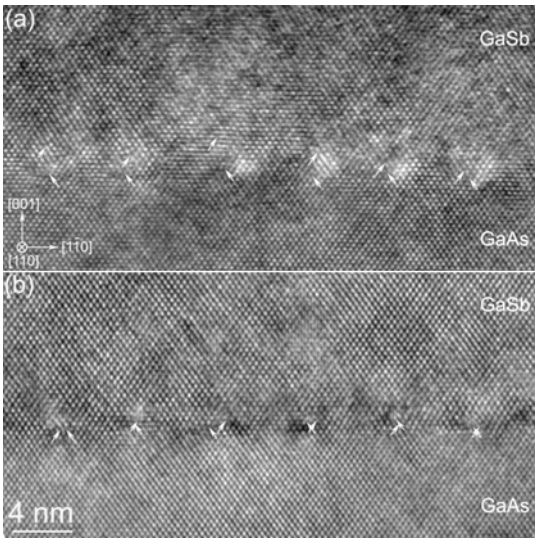

Figure 3.4 Cross-sectional HRTEM images of the GaSb on (001) GaAs with Ga-rich (a) and Sb-rich (b) surface observed along [110] orientation. The inclined arrows indicate the extra {111} planes close to the interface.

Fig. 3.5 shows the ε_{xx} component of the strain field (x axis along the $[1\bar{1}0]$) derived from Fig. 3.4. On these images the dislocation cores are easily located, as they corresponding to the areas where the strain is maximal. Besides the strain distribution, the distance of the split cores in sample A is larger than that in sample B.

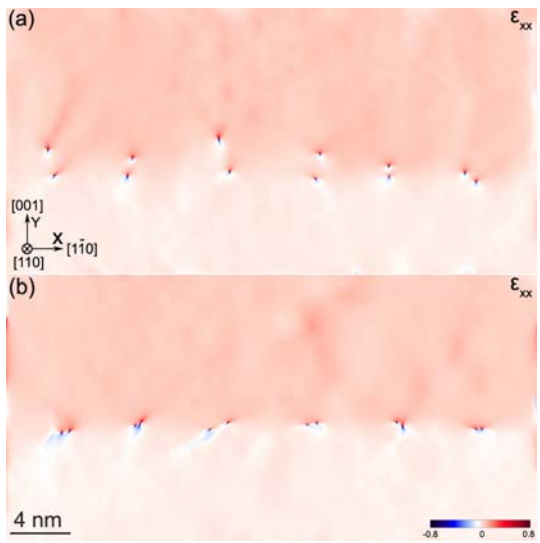

Figure 3. 5 Strain ε_{xx} components corresponding to the Fig. 3.4 HRTEM images. In sample A all the interface misfit dislocation cores are split in two. In sample B, the cores of the Lomer dislocations are compact.

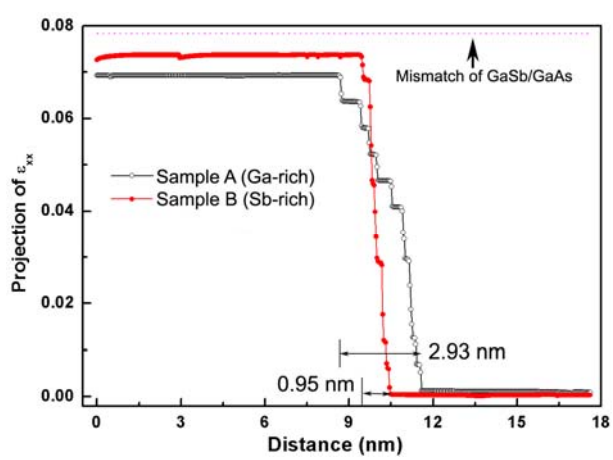

Figure 3. 6 The corresponding projection of the ε_{xx} images on the growth direction, the vertical part of each curve shows the interfacial layer thickness and the max height corresponds to the relaxation level.

To quantify the strain relaxation state, we project the ε_{xx} on the growth direction (y axis). As shown in Fig. 3.6, the value of ε_{xx} in sample B is larger than sample A indicative of a better strain relaxation in sample B. Moreover, the abrupt change in the intensity at the interface region reveals that the thickness of the dislocation cores region is 2.93 nm and 0.95 nm for sample A and B, respectively. This small thickness of the dislocation cores region indicates a sharp interface between the GaSb epitaxial layer and GaAs substrate with Sb-rich surface treatment in sample B.

Fig. 3.7 (a) shows the HRTEM image of the interface between the GaSb epitaxial layer and the GaAs (001) substrates for sample C with 4 MLs AlSb interlayer. It can be noticed that the interface appears not completely flat, through it is better than sample A, moreover one 60° dislocation is also visible. When the growth is initiated on the (2×8) reconstructed Sb-riched GaAs surface, as shown in Fig. 3.7 (b) for sample

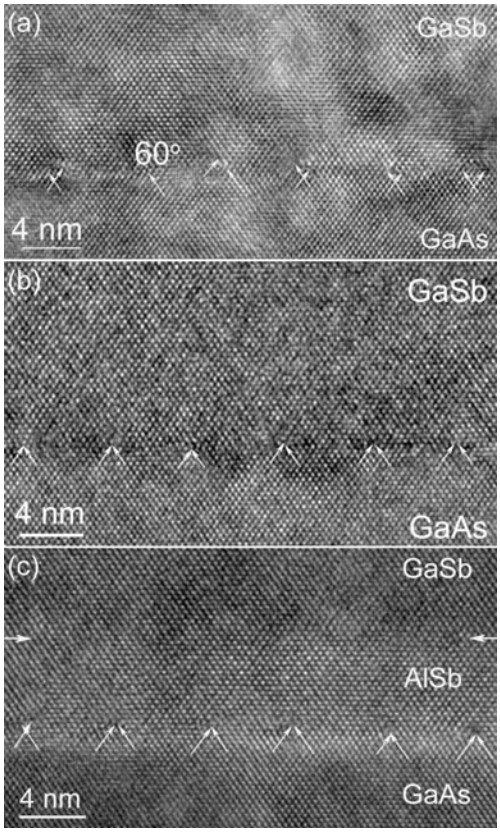

Figure 3. 7 HRTEM images of the buffer layer and GaAs interface along the [110] orientation: (a) Sample C, the Lomer dislocation cores are extended, as well, and a pure 60° dislocation is also visible. (b) Sample D, the dislocations are of Lomer type, with compact cores. (c) Sample E, the AlSb/GaSb interface is shown by horizontal white arrows.

D, the misfit dislocations appears to settle inside the same (001) lattice plan and the interface becomes flat. Moreover, in contrast to the other samples, at this scale, all the {111} additional lattice plane pairs of each interface dislocation are seen to originate from the same points: this is a clear indication that we now have Lomer dislocations. The investigated thickest AlSb interlayer is also interesting; as shown in Fig. 3.7 (c), when the AlSb interlayer thickness is increased to some 16 MLs (5 nm) for sample E, the interface is still flat. However, a close examination of the additional lattice planes shows that the interface dislocations are less compact than in Fig. 3.7 (b). The AlSb layer is now continuous because of the coalescence of the AlSb islands; its limit is marked by the two horizontal white arrows in Fig. 3.7 (c). As could be expected from the small mismatch between AlSb and GaSb, there are no observed misfit dislocations at the top of the AlSb interlayer. A similar behavior of insertion a thick layer AlSb was reported by Kim et al. [21]; although these authors have dealt with even thicker AlSb interlayers (9 and 22 nm), therefore, our observations may be pointing out to a possible degradation of the layer quality starting at smaller AlSb interlayer thickness in comparison with optimized AlSb interlayer thickness. Based on the analysis of several images (with more than 30 pairs of dislocations for each sample), the fraction of the 60° dislocations and the mean spacing of the Lomer dislocations are summarized in Tab. 3.1. The sudden improvement from sample C to D may probably be related to a critical size effect for the AlSb islands [23]. During this initial growth stage, the AlSb deposits into coherent islands at the GaAs surface [21]. It appears that the Sb-rich surface reconstruction promotes a better wetting of AlSb on the GaSb surface. Looking at our statistical results in Tab. 3.1, the higher percentage of 60° misfit dislocations and wide distribution of Lomer dislocation spacing of sample C are in agreement with such a process. The improved GaSb bulk layer quality and interface seems to be related to a larger coverage of GaAs surface by AlSb. The rougher interface and higher percentage of 60° dislocations of sample A and C originated from the larger contact area at GaSb/GaAs hetero-interface. A similar phenomenon was also reported by Kim et al. in GaSb/Si system with an AlSb buffer layer [13]. Conventionally, the 60° dislocations which have their Burgers vector out of the interface plane are considered as possible easy sources for the threading dislocations [24]; the higher percentage of such defects in sample A and C is consistent with the

density of threading dislocations obtained from the plan view observations. However, on growth of a thick AlSb layer, the AlSb islands will have coalesced into a continuous nanometric layer, as has been pointed out above in Fig. 3.2. As shown in Fig. 3.7 (c) the lighter contrast at the GaAs surface corresponds to this AlSb buffer layer (the horizontal arrows indicate the interface of AlSb/GaSb). This is probably equivalent to directly grow an AlSb bulk layer on the GaAs, and the possible surfactant effect for GaSb may not be operating any more.

As summarized in Tab. 3.1, for sample E, the average distance of the interface dislocations almost coincide with the theoretical value of 5.51 nm for the GaSb/GaAs heterostructure, indicative of a relaxed (99.6%) epitaxial layer [25]. Consequently, if it was possible to tune the confinement of the misfit dislocation at the interface and to form a perfectly uniform Lomer dislocation array, this may lead to the

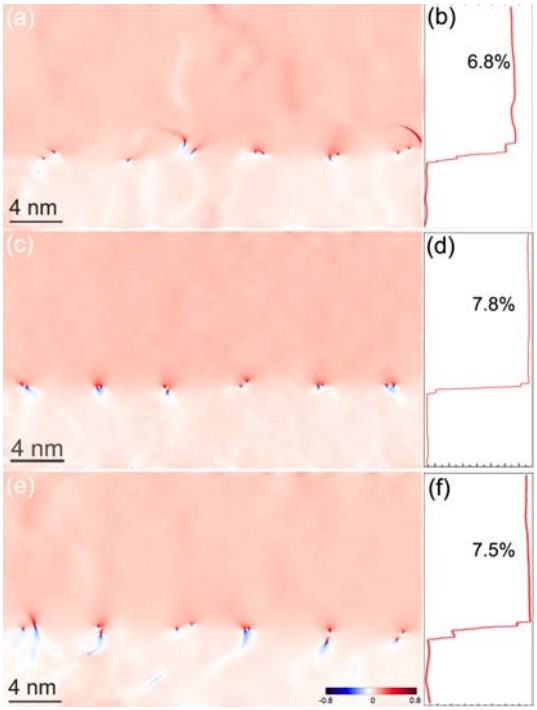

Figure 3.8 Strain components ε_{xx} images corresponding to the Fig. 3.7 HRTEM images, (a) Sample C, the interface is slightly flatter than in sample A, (b)Projection of the images on the growth direction, the broken horizontal line indicates the thickness of the interfacial area. (c) In sample D the cores of the Lomer dislocations are compact. (d)The misfit strain is locally relieved. (e) Sample E, the distance between the pairs of interfacial 60° dislocation is now obvious for all the dislocations, although smaller than in samples A and C. (f) The misfit strain has been relieved up to 96%.

growth with smooth surfaces and a dramatic reduction of the threading dislocations density in the epitaxial layers [17, 21].

Figure 3.8 shows the ε_{xx} component of the strain field (deformation along the [001] growth direction) derived from Fig. 3.7. Like sample A, all the Lomer dislocation cores are split in two in sample C. Now moving to samples D and E, it can be noticed in Fig. 3.8 (c) that the cores of the Lomer dislocations are more compact, and this effect is more underlined in sample D. Moreover, the strain distributions in both images are more uniform, in contrast to the maps of Fig. 3.6 (b) and Fig.3.8 (a). As shown by the curves in Fig. 3.8, the strain state of the three samples is quite different. For sample B, with 3 MLs AlSb, only 6.8% of the misfit that has been locally relieved, and as shown, for sample D, the relaxation of the 7.8% mismatch appears to have been attained, at least locally. The change in the intensity at the interface region reveals that the thickness of the dislocation cores region is 2.02 nm, 0.7 nm, and 1.14 nm for sample C, D, and E, respectively, as summarized in Tab. 3.1.

The fine structure of the interface dislocation can further be analyzed using dislocation density tensor [28, 29]. The dislocation density tensors α_x and α_y are derivate from lattice distortion field by equation 2.15

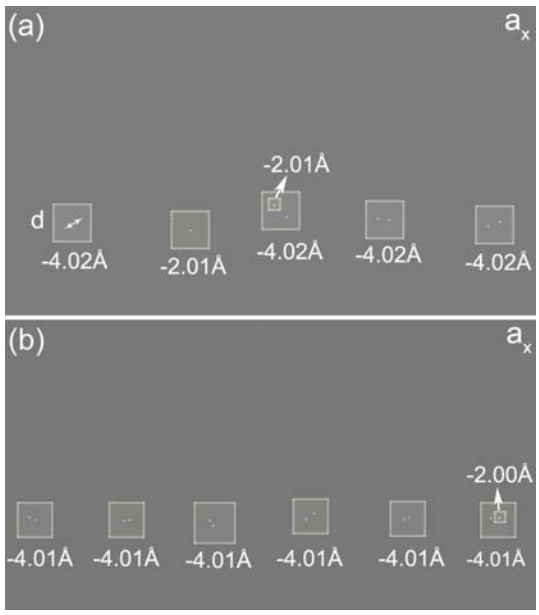

Figure 3.9 The α_x component of the dislocation distribution tensor field, the calculated Burgers vactors have been written in the image: (a) for sample C, (b) Sample D.

and 2.16. Integrating the components of **α** over the dislocation core region, we can obtain the corresponding the Burgers vector component as presented in Fig. 3.9, where it can be seen that the calculated Burgers vector components are very close to the theoretical value for Lomer dislocation (b= a/2 [$\bar{1}$10]= 4.00 Å). Integrating the two dislocation density peaks of the Lomer dislocation separately, we obtain two Burgers vectors corresponding to in-plane components of two 60° dislocations. Therefore, in the analyzed areas, each Lomer dislocation is separated by a nanometer scale distance in two 60° dislocations, as shown by the core positions. The distance between dissociated cores for the Lomer dislocations as determined in many areas (more than 30 pairs of dislocations for each sample) is presented in Fig. 3.10. Obviously, the dislocation cores of sample D are more localized, indeed, the splittings are within 1 nm.

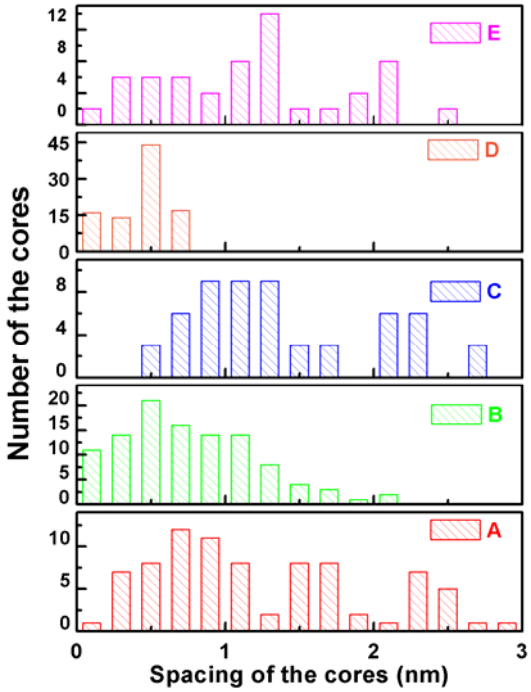

Figure 3.10 Statistical distribution of the distance (d, as schematically shown in Fig 3.9 a) between the 60° dislocation pairs of split Lomer dislocation cores.

For comparison of the 4 samples, we arbitrarily assume the interface dislocation is a Lomer, when the separation distance between the pairs of 60° dislocation is less than 1.5 nm. We then have 64.7%, 93.5 %,

68.4%, 100%, and 75.8% of Lomer dislocations, for sample A, B, C, D, and E, respectively. Of course, this is a simple assumption, and for the 5 samples, all the interface dislocations are split into pairs of 60°; even in sample D, the pairs are indeed the closest but they are not completely merged.

3.1.4 Discussion

From the above local analysis of the strain relief at the interfaces, it is comes out that the AlSb interlayers thickness and the GaAs surface preparation are important parameters in determining the relaxation state of at the GaSb/GaAs interface. In their investigation, Kim et al. [21] have analyzed 1.2 nm, 9.7 nm and 22 nm AlSb interlayer thicknesses. They reported that the smallest roughness and best interface structure was connected with the smallest AlSb interlayer (1.2 nm). This is comparable to our sample C and D. From these samples, besides the AlSb thickness, the surface preparation plays a crucial role. Indeed, comparison of samples A, C and E evidences that the best results starting with an element III-rich GaAs surface are obtained for the thickest AlSb deposit. However, starting the AlSb growth on a Sb-rich GaAs surface (sample D) leads to even better results. This sample exhibits a relief of the local strain to mostly 100%, the interface dislocations as observed are all of Lomer type within our arbitrarily defined distance between the pairs of 60° dislocation pairs. Moreover, the interface thickness of this sample is the smallest, meaning that the strain is highly localized at the interface. One important point needs to be noticed at this stage, looking at the threading dislocation densities, our measured values are, of course, one order of magnitude lower than in the other samples. Indeed, this is still two orders of magnitude higher than the best values reported in such systems [3, 15], which were reported to exhibit substantially low threading dislocation densities (~10^5 cm^{-2}). When AlSb thickness is increased to 16 MLs (5 nm), the interface stays flat but the distance between the 60° pairs of interface dislocations is more fluctuating. So from the above observations, one may conclude that the decrease of the threading dislocations densities inside such highly mismatched compounds is possible to come from the following two procedures: 1. The formation of Lomer dislocations at the interface, 2. The localization of the strain inside the interface plane. The two

processes will possibly be accompanied or lead to the formation of a flat interface. In the above observations, it is seen that flat interfaces within one monolayer are attained for the two samples (D and E). For sample D, the distance between the pairs of 60° dislocation is less than 1 nm, whereas it fluctuates more in samples E, and the interface thickness also degrades.

From the reports on strain relaxation inside epitaxial layers, the glide of 60° dislocations to interface and reaction in pairs to form Lomer dislocations optimally contributes to the relaxation [6]. Inside investigated layers, the formation of non merged 60° dislocations with distances of 0.5-2 nm is observed to be systematic. In fact looking at the reports in the literature, this behavior is probably not limited to our system and/or growth conditions [3, 23]. Of course an important trend may be pointed out from our results: one order of magnitude reduction of threading dislocation density appears to be related to an increased localization of the strain at the interface, as well as, to the smallest splitting of the interface Lomer dislocations.

3.2 Initial stages of GaSb growth on (001) GaP

3.2.1 Introduction

As we reviewed in the first Chapter, besides the lattice mismatch issue, direct expitaxy of antimonides on Si substrate faces another issue: the presence of IDBs or APBs [30] due to the difference in polarity between the epitaxial layer and substrate. Some methods such as using an AlSb nucleation layer [17, 18] as well as miscut Si substrate [31] have proved useful in suppressing APBs. Combining the AlSb nucleation layer (50 nm) and the miscut substrate (5° micut), Huffaker's group have recent obtained defect free ($< 10^{6}$ cm^{-2}) GaSb epitiaxy layer [32] [33]. However, exactly oriented Si substrate is the standard ones in the current Si technology. Recently, APB-free GaP layers on exactly oriented Si substrate have been achieved after 50 nm overgrowth [34]. Such GaP templates could be used for the subsequent growth of antimonides which may be an alternate way for the integration of Sb-based devices

on Si. For this reason, we try to grow GaSb on GaP. As we have noticed in the previous section that the initial growth conditions play a critical role on the structure of the misfit dislocation and strain relaxation. In this section, we pay a careful attention on the misfit dislocation and strain relaxation at the initial growth steps. The influence of the surface preparation, growth rate and temperature on the strain relaxation of the GaSb islands on GaP was investigated

3.2.2 Samples

3 series of samples were designed for the growth parameters optimization, as schematically shown in Fig.3.11. The GaP substrate was deoxided at 650°C under P flux obtained by cracking phosphine (PH_3) throungh a high-temperature injector. Then a 400 nm GaP buffer layer was grown at 610°C to obtain a smooth GaP surface. After substrate smoothing, the substrate showed a sharp (2x4) reflection RHEED pattern and the sample temperature was decreased for the growth of GaSb. First, two samples were grown at 480°C to study the influence of the GaP surface treatment on the relaxation of 10 GaSb MLs. For Ga-rich surface treatment, the substrate was cooled down to 480°C without any flux (the substrate keeping a (2x4) surface reconstruction), then 1 Ga ML was deposited before the opening of the Sb valve with a subsequent growth of 9 GaSb MLs. For Sb-rich surface treatment, after the interruption of the phosphine flux, the substrate was cooled down to 480°C under Sb_2. Then the Ga shutter was opened and 10 GaSb MLs were deposited. After the optimization of the surface treatment, two series of samples were grown to study the influence of the growth rate and the growth temperature on GaSb strain relaxation. For the two series of samples, the Sb flux was fixed at 2.5 ML.s^{-1}, varying the growth rate from 0.1 ML/s to 1.0 ML/s at 480°C, and the growth temperature from 450°C and 530°C at a growth rate of 0.7 ML/s. For all samples, a three-demension Volumer-Weber (VW) growth mode was observed at the initial growth of first ML GaSb and two-dimension RHEED pattens with a (1x3) surface reconstruction starts to appear after 10 ML GaSb.

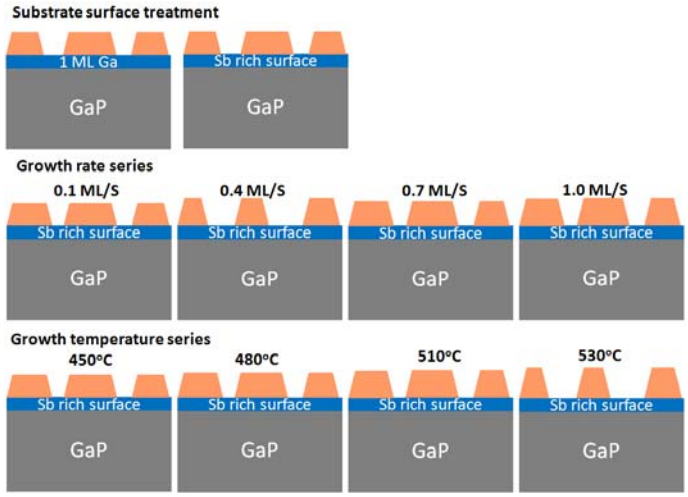

Figure 3.11 Schematic diagrams of the layout of the investigated samples in this section, the GaSb layers thickness are 10 MLs.

3.2.3 Surface treatment

The growth was monitored by the RHEED, where the evolution of the in-plane lattice constant during the growth is deduced from the inter-reticular spacing between the (1 0) and the (-1 0) diffraction streaks. Figure 3.12 display the dynamic variation of the lattice constant during the first 3 ML of GaSb growth. For both Ga-rich and Sb-rich condition, a quick change from the GaP lattice constant (5.4505 Å) to a value close to that of GaSb (6.095 Å) occurs during the first monolayer. However, this relaxation is faster for the samples with Sb-rich surface treatment (about 0.7 ML) than for sample with Ga-rich surface treatment (about 1.6 ML). Moreover, after 3 ML the lattice constant of the sample with Sb-rich surface treatment is a bit larger than the sample Ga-rich surface treatment about 6.1 Å versus 6.05 Å. This suggests a better relaxation for sample with Sb-rich surface treatment.

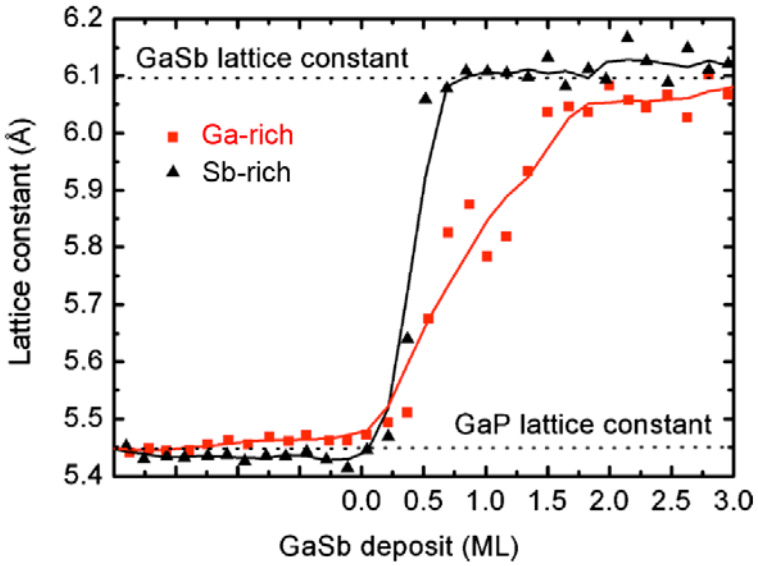

Figure 3.12 Lattice constant evolutions during the first 3 GaSb MLs deposition on a Ga-rich and a Sb-rich GaP surface.

Figure 3.13 shows HRTEM images of the $(1\bar{1}0)$ interface between the GaSb islands and GaP substrate with Ga-rich (a) and Sb-rich (b) surface treatment. In these images, the positions of the interface dislocations have been marked by the additional {111} lattice planes (inclined arrows). Lomer

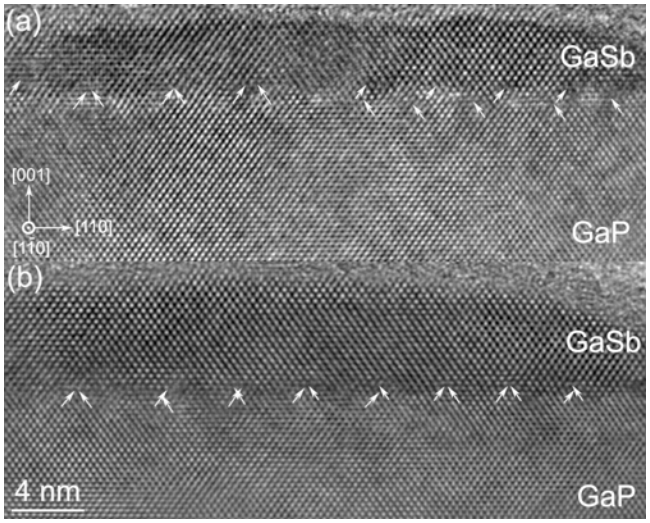

Figure 3.13 Cross-sectional HRTEM images of the GaSb islands on (001) GaP with Ga-rich (a) and Sb-rich (b) surface observed along $[1\bar{1}0]$ orientation. The inclined arrows indicate the extra {111} planes close to the interface.

dislocations, closely spaced 60° dislocation pairs as well as the 60° dislocations can be seen along the interface. As shown in Fig. 3.13 (a), some dislocations glide into the substrate and most of the misfit dislocations are closely spaced 60° dislocation pairs. In contrast, all the extra {111} planes terminate at the interface and Lomer dislocations are the major misfit dislocation at the interface in sample with Sb-rich surface treatment (Fig. 3.12 (b)). Moreover, some 60° dislocations can also be found at the edges of islands in with Ga-rich surface treatment. Given the difference in misfit dislocations between the two samples, one can conclude that the Sb-rich GaP surface promotes the formation of Lomer misfit dislocations, which are more efficient for strain relaxation.

Figure 3.14 (a) and (c) shows the ε_{xx} component of the strain field (x axis along the $[1\bar{1}0]$) derived from Fig. 3.13 (a) and (b), respectively. Beside the strain distribution, the distance of the split cores in the sample with Ga-rich surface treatment is obviously larger than that in sample with Sb-rich surface treatment. To quantify the strain relaxation state, one can project the ε_{xx} on the growth direction (y axis).

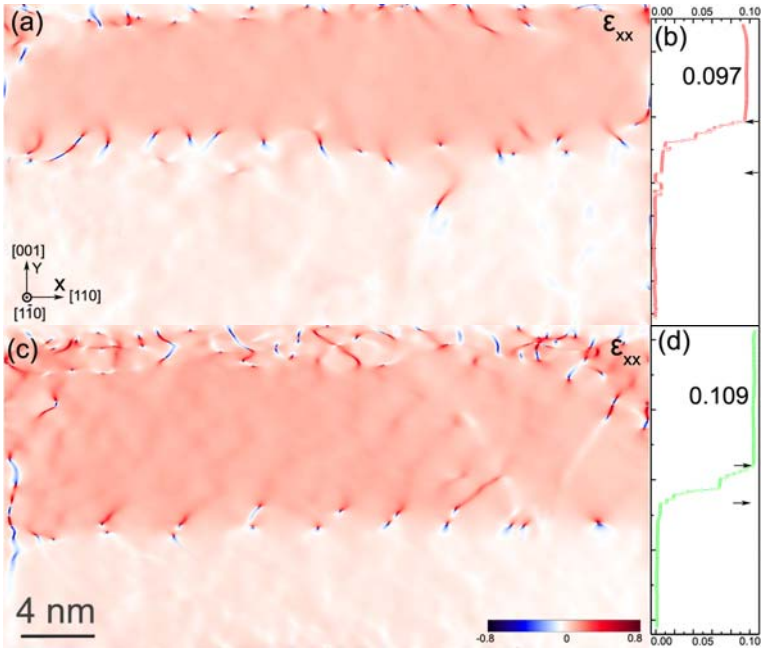

Figure 3.14 Strain ε_{xx} components corresponding to the Fig. 3.13 HRTEM images. (b) and (d) are the corresponding projection of the ε_{xx} images on the growth direction, the broken horizontal line indicates the thickness of the interfacial area.

As shown in Fig. 3.14 (b) and (d), the value of ε_{xx} in the sample with Sb-rich surface treatment is larger than that with Ga-rich treatment. This is consistent with the evolution of the lattice parameters from RHEED measurements as shown in Fig. 3.12. The abrupt change in the intensity at the interface region reveals that the thickness of the dislocation cores region is 1.4 nm and 0.8 nm for sample with Ga-rich and Sb-rich treatment, respectively. The decrease of the dislocation core regions thickness indicates the mismatch strain is more confined at the interface with Sb-rich surface treatment. The above observation are in agreement with the one we discussed in the former section of the growth of GaSb on (001) GaAs. However, in this case, the mismatch is ~ 12% instead of ~ 8% for the GaSb/GaAs system. The Sb-rich surface treatment promotes a Lomer dislocation network, and it is probably a common feature for highly mismatched Sb-based material system. The improvement of the interface quality may be due to that the Sb-rich surface treatment on which adatom site exchange is energetically unfavorable [35, 36] could prohibit the group-V elements intermixing (P/Sb in this instance).

3.2.4 Optimization of the growth rate and growth temperature

As for the influence of growth rate, the average distance of the Lomer dislocation and mean relaxation

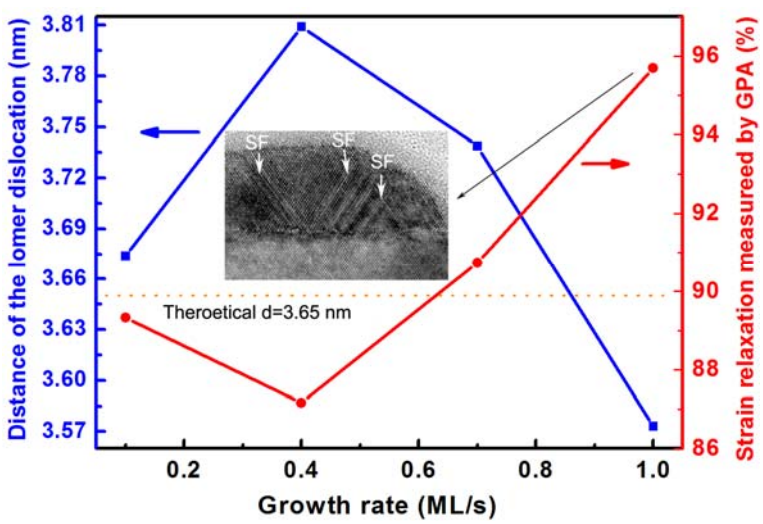

Figure 3.15 The mean spacing of the Lomer dislocation and strain relief of the island as a function of the growth rate. The inset shows a HRTEM image of GaSb island with a growth rate of 1.0 ML/s, the stacking faults (SF) are indicated by the arrows.

state of the GaSb islands in function of growth rate are summarized in Fig. 3.15. The sample grown at 1.0 ML/s exhibits the highest strain relaxation, however at this rate many planar defects (stacking faults, as shown in inset in Fig.3.15) have been observed to form in the epitaxial layer. This is in agreement with the fact that high growth rates enhance surface nucleation along with the formation of high densities of vacancy clusters, which leads to a generation of stacking faults subsequent to their collapse [36]. Therefore, as the stacking faults also contribute to the strain relaxation, the sample shows the highest strain relaxation state, though the mean Lomer dislocations distance deviates from the theoretical (or ideal) value 3.65 nm by assuming the mismatch strain relaxed by Lomer dislocation array ($d=|b|/f$=3.65 nm, where $b=\frac{a}{2}[1\bar{1}0]$ is the Burgers vector of a Lomer dislocation and f is the lattice mismatch between GaSb and GaP). Because of the presence of the stacking faults at 1ML/s, we chose the rate of 0.7 ML/s for subsequent investigations.

Figure 3.16 displays the average distance between the Lomer dislocations at the GaSb/GaP interface and mean relaxation of the GaSb islands as function of growth temperature. The distance between Lomer dislocations decreases when the growth temperature is increased, reaching a value close to the theoretical

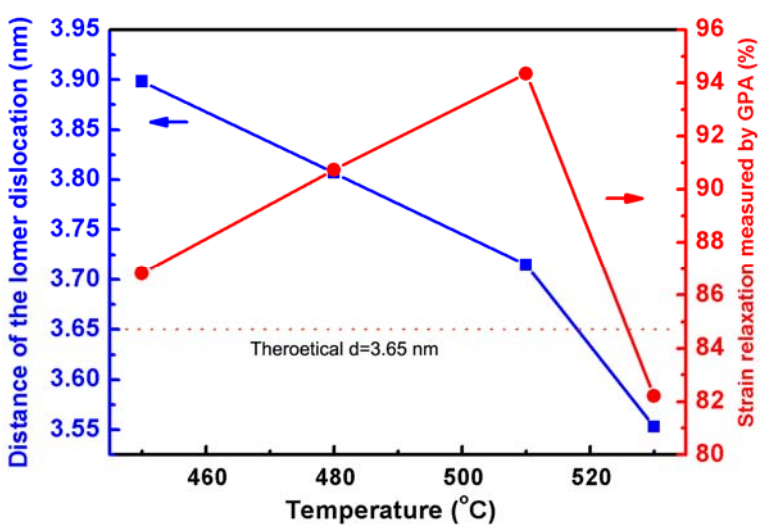

Figure 3.16 The average spacing of the Lomer dislocation and strain relief of the island as a function of the growth temperature. Dotted line indicates the ideal distance of Lomer dislocations at full relaxed GaSb/GaP interface.

one for the sample grown at 510° C. The strain relaxation state derived from HRTEM by GPA confirms this observation: the sample grown at 510° C shows the highest strain relaxation. For the sample growth at 530°C, the mean distance between the Lomer misfit dislocations is smaller than the theoretical (or ideal) value which is due to the formation of 60° dislocations. Huang et al. [15] have also reported that the 60° dislocation tends to form at higher growth temperature (560 ^{o}C) for the GaSb/GaAs system.

3.2.5 The threading dislocation density and strain relaxation in the GaSb template layer

Using the above optimized growth condition (Sb-rich surface treatment, and growth rate of 0.7 ML/s at 510°C), a 600 nm GaSb template layer was grown on the GaP substrate. As can be seen from the cross section weak beam dark field image (Fig. 3.17 (a)), the threading dislocations are generated at the GaSb/GaP interface. In this image, only a few of them propagate to the top layer (horizontal arrow), most of them have their line cut during the sample preparation (vertical arrow) or form closed dislocation loop (inclined arrow). As proposed by Qian et al. [14], the reaction of the threading dislocations leads to TDs density decrease when the epitaxial layer thickness is increased. If we assume the thickness of the TEM

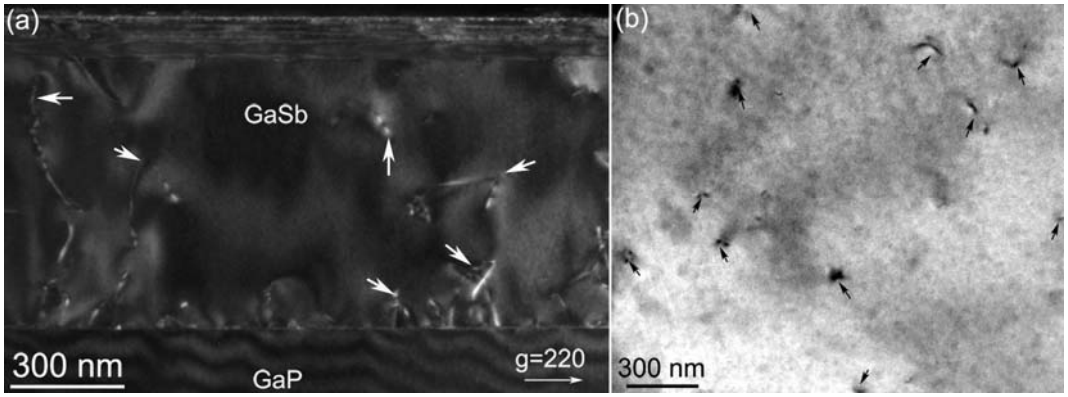

Figure 3.17 (a) Cross-sectional weak beam dark field image of the AlSb/InAs heterstructures on (001) GaP substrate with GaSb buffer layer using optimized growth condition, observed with g= $\bar{2}20$ *zone axis. (b) Plan-view TEM images of 600 nm GaSb on GaP substrate, recorded close to the [001] growth axis. The threading dislocations are marked by the arrows.*

specimen is about 300 nm, for this investigated area we can roughly estimated that the TDs density is 1.9 x 10^8 cm^{-2} (Fig. 3.17 (b)). An accurate measurement of the TDs density was performed in the plan-view TEM observation; the TDs density was determined as 3.6x10^8 cm^{-2} showing the same order of magnitude with the value estimated by the cross-section observation. With this optimized growth condition, we are still 2 orders of magnitude away from the goal of reducing the defects density to 10^6 cm^2.

Figure 3.18 (a) shows the HRTEM image at GaSb/GaP interface observed along $[1\bar{1}0]$ direction. The strain state is presented in Fig. 3.18 (b) and Figure 3.18 (c) shows the projection of the strain profile on the growth direction. The thickness of the dislocation cores region is 0.87 nm, which is less than two unit cells of GaSb. Above the dislocation core region, the apparent strain reaches the value of 11.2%, which is close to the lattice mismatch (11.8%) between GaP and GaSb and implies that the GaSb epitaxial layer has reached a strain relaxation state of 95% at the interface.

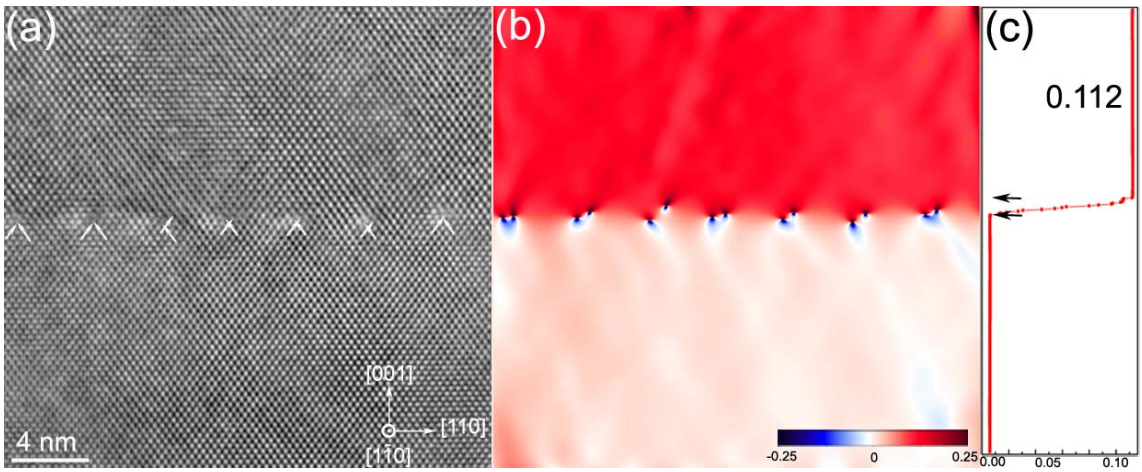

Figure 3.18 HRTEM images (a) and strain mapping (b) of the GaSb layer on GaP. (c) The projection of the strain filed on the growth direction. The thickness of the misfit dislocation core region is indicated by the arrows.

3.3 AlSb/InAs hetero-structures on relaxed GaSb template layer

Following pioneering work of Chang et al. at IBM, first on InAs/GaSb [37], and subsequently on InAs/AlSb [38], Tuttle et al. [39, 40] started, to investigate the properties of InAs/AlSb quantum well systematically. Though 20 years past, as pointed out by Bennet et al. [2] in their recent review that it is

still difficult to achieve a 30000 $cm^2V^{-1}s^{-1}$ at room temperature (RT) using a semi-insulating buffer. Up to now, on GaAs substrate, InAs/AlSb quantum well reaching a RT mobility of 30000 $cm^2V^{-1}s^{-1}$ have been reported using the initial thin AlSb nucleation layer followed by a thick GaSb template layer (generally several micro meters thick) as well as superlattice layer for filtering the defects [39, 41]; on InP substrate which lattice mismatch with InAs is half smaller than GaAs substrate, the RT mobility has reached to 34300 $cm^2V^{-1}s^{-1}$ [40].

In this section, we examine the transport properties of the AlSb/InAs hetero-structures using our optimized GaSb buffer layers. The AlSb/InAs hetero-structures whose structure is schematically shown in Fig. 3.19 are fabricated on the best GaSb buffer layer we obtained (Sample B and D with GaAs as

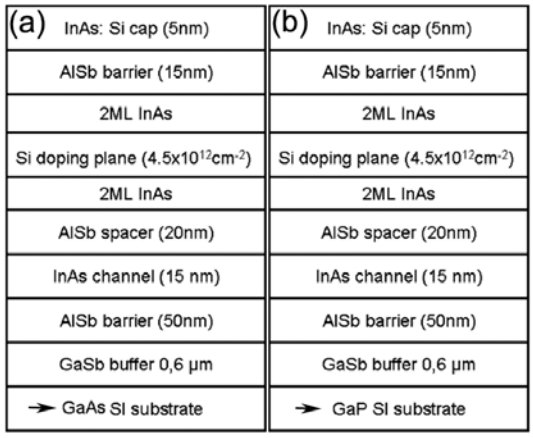

Figure 3.19 The schematic of the AlSb/InAs high electron mobility hetero-structure grown on GaSb buffer layer with GaAs (a) and GaP (b) substrates.

substrate, as well as the one grown on GaP substrate with optimized growth parameters). These hetero-structure exhibits surface roughness of 0.27 nm measured by AFM on 1µm x 1µm. Hall effect measurements using the Van der Pauw configuration show that these hetero-structures have high mobility, as we summarize in Tab.3.2. These transport properties are comparable or even better than the reported on GaAs [39], where the buffer layers were much thicker than ours (several micro meters) and the buffer layers techniques are more complicated than ours. For instance the one we adapted from Tuttle et al. [39], the buffer layers have a thickness of 3 µm consisted of 1 µm GaSb, 2 µm AlSb, and a ten period GaSb

(2.5 nm) /GaSb (2.5 nm) superlattice have a threading dislocation density less than 10^7 cm^{-2}. Although still lower than the reports from Desplanque et al. [42], they used InP substrate which lattice mismatch with InAs is half (one third) smaller than GaAs (GaP) substrate.

Table 3. 2 The summary of the transport properties of the AlSb/InAs hetero-structures, the value of reference devices by Tettle et al. [39]and Desplanque et al. [42] are also listed for comparison.

Devices	TDs density (10^8 cm^{-2})	Electron mobility ($cm^2 V^{-1} s^{-1}$)		Sheet carrier density (10^{12} cm^{-2})	
		300K	77K	300k	77K
On sample B (600 nm GaSb)	2.2	29800	191000	1.8	1.17
On sample D (600 nm GaSb)	0.64	30000	143000	1.8	1.17
On GaP (600 nm GaSb)	3.6	25500	108000	2.0	1.6
Tuttle et al. [39]	< 0.1	25000	230000 (55K)	1.25	0.8
Desplanque et al. [42]	Buffer: 1200 nm GaSb	34300	223000	1.45	1.15
	Buffer: 600nm GaSb	32900	197000	1.5	1.26

3.4 Conclusion

We have shown that Sb-rich surface treatment promotes the formation of Lomer dislocation at the GaSb/GaAs interface; and, this is also valid in epitaxy of GaSb on GaP substrate. The AlSb interlayer improves the interfacial quality and leads to flat interface, the optimization of the interlayer thickness is critical. Sb-rich substrate surface treatment plus 4 MLs AlSb interlayer lead to relaxed GaSb layer on GaAs substrate and reduce the threading dislocation density to 10^7 cm^{-2}. A quantitative measurement of the local Burgers vectors shows that the misfit dislocations at the GaSb/GaAs interface are always 60° dislocations. They are arranged in pairs which are more or less distant. For the samples with the lower threading dislocation density, the average distance between the 60° pairs is smaller, the interface is flatter and the local strain is more relieved.

In the case of GaSb on GaP, Sb-rich surface treatment was found to lead to the best strain relaxation by promoting the formation of Lomer misfit dislocations. The analysis of the strain, versus the growth temperature and rate, predicts an optimal window (Sb rich substrate surface treatment, growth rate of 0.7 ML/s, and growth temperature of 510°C) for the growth a low strain GaSb epitaxial layers.

With these relaxed GaSb buffer layer, a high mobility AlSb/InAs hetero-structure with RT mobility of 30000 $cm^2V^{-1}s^{-1}$ (25500 $cm^2V^{-1}s^{-1}$) on semi-insulating GaAs (GaP) substrate has been achieved though the threading dislocation is in the 10^7 -10^8 cm^{-2} range.

References

[1]I.Vurgaftman, J.R.Meyer, and L.R.Ram-Mohan, J.Appl.Phys. **89**, 5815 (2001).

[2]B.R.Bennett, R.Magno, J.B.Boos, Walter.Kruppa, and M.G.Ancona, Solid-State Electron. **49**, 1875 (2005).

[3]S.Huang, G.Balakrishnan, and D.L.Huffaker, J.Appl.Phys. **105**,103104 (2009).

[4]A. Vila, A. Cornet, J.R. Morante, and P. Ruterana, presented at Microsc. Semiconduct. Mat.1993, in Inst. Phys. Conf. Ser. **134**, 353 (1993).

[5]K.N.Tu, J.W.Mayer, and L.C.Feldman, *Electronic Thin Film Science: For Electrical Engineer and Materials Scientist* (Macmillan, New York, 1992).

[6]P.M.J.Maree, J.C.Barbour, J.F.van der Veen, K.L.Kavanagh, C.W.T.Bulle-Lieuwma, and M.P.A.Viegers, J.Appl.Phys. **62**,4413 (1987).

[7]A. Vila, A. Cornet, J.R. Morante, P. Ruterana, R. Bonnet, and M. Loubradou, presented at Microsc. Semiconduct. Mat.1995, in Inst. Phys. Conf. Ser. **146**, 83 (1995).

[8]A.Georgakilas, P.Panayotatos, J.Stoemenos, J.L.Mourrain, and A.Christou, J. Appl. Phys. **71**, 2679 (1992).

[9]A. Vila, A. Cornet, J. R. Morante, P. Ruterana, M. Loubradou, R. Bonnet, Y. Gonzalez, and L. Gonzalez, Philos. Mag. A. **71**, 85 (1995).

[10]W. Qian, M. Skowronski, R. Kaspi, M.De Graef, and V.P.Dravid, J. Appl. Phys. **81**, 7268 (1997).

[11]A. Vila , A. Cornet, J. R. Morante, P. Ruterana, M. Loubradou, and R. Bonnet, J. Appl. Phys. **79**, 676 (1996).

[12]R. E. Mallard, P. R. Wilshaw, N. J. Mason, P. J. Walker, and G. R. Booker, presented at Microsc. Semiconduct. Mat.1989, in Inst. Phys. Conf. Ser. **100**, 331 (1989).

[13]J.H. Kim, T.Y. Seong, N. J. Mason, and P. J. Walker, J. Electron. Mater. **27**, 466 (1998).

[14]W. Qian, M. Skowronski, and R. Kaspi, J. Electrochem. Soc. **144**, 1430 (1997).

[15]S.H. Huang, G. Balakrishnan, A. Khoshakhlagh, A. Jallipalli, L.R. Dawson, and D.L. Huffaker, Appl.Phys.Lett. **88**,131911 (2006).

[16]J. M. Yarborough, Y.Y. Lai, Y. Kaneda ,J. Hader, J. V. Moloney,T. J. Rotter, G. Balakrishnan, C. Hains, D. Huffaker, S. W. Koch and R. Bedford, Appl. Phys. Lett. **95**, 081112 (2009).

[17]K.Akahane, N. Yamanoto, S.Gozu, A.Ueta, and N.Ohtani, J.Cryst.Growth, **264**, 21 (2004).

[18]Y.H.Kim, J.Y.Lee, Y.G.Noh, M.D.Kim, S.M.Cho, Y.J.Kwon, and J.E.Oh, Appl.Phys.Lett.**88**, 241907 (2006).

[19]Y.H.Kim, Y.K.Noh, M.D.Kim, J.E.Oh, and K.S.Chung, Thin solid films, **518**,2280 (2010).

20S.J.Brown, M.P.Grimshaw, D.A.Ritchie, and G.A.C.Jones, Appl.Phys.Lett.**69**, 1468 (1996).

[21]H.S.Kim, Y.K.Noh, M.D.Kim, Y.J.Kwon, J.E.Oh, Y.H.Kim, J.Y.Lee, S.G.Kim, and K.S.Chung, J.Cryst.Growth, **301-302**, 230 (2007).

[22]S.H.Huang, G.Balakrishnan,M.Mehta, A.Khoshakhlagh, L.R.Dawson, and D.L.Huffaker, Appl.Phys.Lett.**90**,161902 (2007).

[23]B.R. Bennett, P.M. Thibado, M.E. Twigg, E.R. Glaser, R. Magno, B.V. Shanabrook, and L.J. Whitman, J. Vac. Sci. Technol. B**14** , 2195 (1996).

[24]A. Rocher, and E. Snoeck, Mater. Sci. Eng., B **67**, 62 (1999).

[25]M.O.Manasreh, Antimonide Related Strained Layer Heterostructures (Gordon and Breach Science Publishers, Amsterdam, 1997), p. 107.

[26]M.J.Hytch, E.Snoek, and R.Kilaas, Ultramicroscopy, **74**, 131(1998).

[27]S.Kret, P.Ruterana, A.Rosenauer, and D.Gerthsen, Phys. Status Solidi B **227**, 247 (2001).

[28]S.Kret, P.Dluzewski, P.Dluzewski, and E.Sobczak, J.Phys. :Condens. Matter **12**, 10313 (2000).

[29]S. Kret, P. Ruterana, and G. Nouet, J. Phys. :Condens. Matter **12**, 10249 (2000).

[30]H. K. Choi and M. R. Society, Heteroepitaxy on Silicon: Fundamentals, Structure, and Devices: Symposium Held April 5-8, 1988, Reno, Nevada, U.S.A. (Materials Research Society, 1988).

[31]A. Jallipalli, M. N. Kutty, G. Balakrishnan, J. Tatebayashi, N. Nuntawong, S. H. Huang, L. R. Dawson, D. L. Huffaker, Z. Mi, and P. Bhattacharya, Electron. Lett. **43**, (2007).

[32]D. L. Huffaker, G. Balakrishnan, A. Jallipalli, M. N. Kutty, J. Tatebayashi, S. H. Huang, L. R. Dawson, Z. Mi, and P. Bhattacharya, in (IEEE, Nano-Optoelectronics Workshop, 2007. i-NOW'07. International, 2007), pp. 16–17.

[33]D. Huffaker, *Novel monolithic integration of III-Sb materials on Si substrates,* SPIE Newsroom *DOI: 10.1117/2.1200801.1002*, (2008).

[34]I. Németh, B. Kunert, W. Stolz, and K. Volz, J. Cryst. Growth **310**, 1595 (2008).

[35]M.Copel, M.C.Reuter, E.Kaxiras, and R.M.Tromp, Phys. Rev. Lett. **63**, 632 (1989).

[36]E.Z.Liu and C.Y.Wang, Scripta Materialia, **56**, 113 (2007).

[37]L.L.Chang, L.Esaki, Surf.Sci. **98**, 70 (1980).

[38] C.A.Chang, L.L.Chang, E.E.Mendez, M.S.Christie, and L.Esaki, J.Vac.Sci.Technol.B **2**, 214 (1984).

[39] G.Tuttle, H.Kroemer, and J.H.English, J.Appl.Phys. **65**, 5239 (1989).

[40] G.Tuttle, H.Kroemer, and J.H.English, J.Appl.Phys. **67**, 3032 (1990).

[41] H.Kroemer, Physica E **20**, 196 (2004).

[42]L.Desplanque, D.Vignaud, and X.Wallart, J.Cryst.Growth, **301-302**, 194 (2007).

Chapter 4

The formation mechanism of misfit dislocations

4.1. Introduction

When epitaxy of GaSb on GaAs, with the large mismatch (7.8%), the critical thickness is expected to be of a few monolayers, subsequently, misfit dislocations are generated in order to relieve the mismatch strain. The two types of misfit dislocations have a <110> type Burger vector for a perfect dislocation lying on (001) interface in diamond and zinc-blende–type lattices, at 60° or 90° to its dislocation line, namely, 60° or Lomer (90°) dislocation, respectively [1-3]. The 60° dislocation is a mixed type dislocation, with edge and screw components. In this case, only the <110> edge component is involved in the accommodation of the lattice mismatch, whereas the screw component induces a localized twist between the epitaxial layer and substrate [4]. The misfit strain relieved by a Lomer dislocation is twice that by a 60° dislocation, therefore, the formation of Lomer misfit dislocation would provide the optimal strain relaxation. Besides the Lomer dislocations and 60° dislocations, recent reports show that many closely spaced 60° dislocation pairs with intersecting glide planes also form at such interfaces [5, 6].

Regarding the misfit dislocation formation, a number of models have been proposed [1, 5-11]. A conventional mechanism is based on the glide of 60° dislocations from the surface to the interface [1], and with Lomer dislocations resulting from reaction of 60° dislocations from different glide systems. Based on the conventional mechanism, Narayan et al. [5] reported the formation of Lomer dislocations as well as 60° dislocation pairs. An alternative rebound mechanism has been reported by Dregia and Hirth [7, 8] (Fig. 4.1 (1)): in this instance, the gliding 60° dislocation reaching the interface reacts to form a Lomer dislocation and a product dislocation glides away. This model is assumed to be able to lead to regularly spaced Lomer dislocations, most efficient for the relaxation of the interface strain [8]. The formation of Lomer dislocations may also come from the reaction of a Frank partial dislocation and 90° Shockley

partial dislocation as suggested by Y.Chen et al. [9], as shown in Fig. 4.1 (2). More recently, a fourth mechanism has been reported by Huang et al. [10] and Jallipalli et al. [11] to explain the observed reduction of the threading dislocation density in GaSb/GaAs layers by nearly four orders of magnitude from 10^9 to 10^5 cm^{-2}. It was reported that a careful monitoring of the GaAs reconstruction and initial Sb rich growth may lead to direct nucleation of a Lomer dislocations network at the interface and to a two dimensional (2D) almost defect free GaSb layer at 510 ^oC by molecular beam epitaxy (MBE). However, transmission electron microscopy results at 510 ^oC showed only island growth and the authors concluded that the formation of islands may have taken place during the cooling of the sample [12]. Therefore, it is clear that more work is still needed to understand the growth of these highly mismatched systems, and possibly help to improve the quality of the epitaxial layer in a reproducible way.

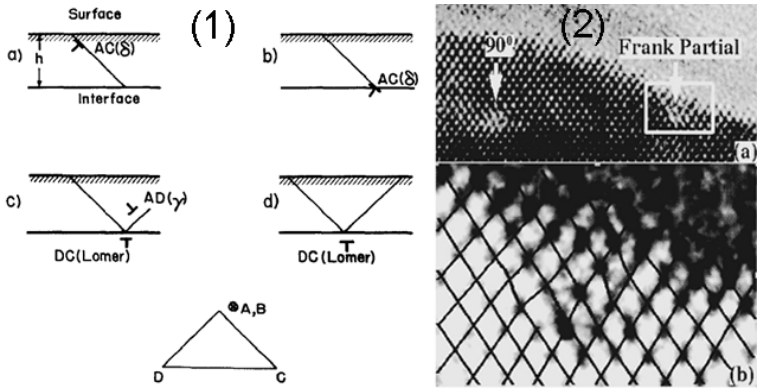

Figure 4. 1 (1)The rebound mechanism: a) dislocation AC nucleation at free surface; b) glide to the interface; c) formation of Lomer DC and product dislocation AD; d) motion of AD to free surface; The sense vector points into the page. (2) The Chen et al. model: a) [110] cross-sectional HRTEM image from an InAs island grown on a GaAs substrate; b) Negative HRTEM image enlarged from the selected area, the atomic position, which appear dark in the negative image, show that a Frank partial dislocation is introduced at the island edge.

To address the misfit dislocation formation mechanism, it is essential to reconstruct the core of the misfit dislocations. Up to now, several research groups have reported the reconstruction of the 60° dislocation and Lomer dislocation cores at CdTe/GaAs [13], GaAs/Si [2, 3, 14], Ge/Si [15], and GaSb/Si [16] interfaces, however the proposed structures have been mainly drawn according to transmission electron

microscopy (TEM) or scanning transmission electron microscopy (STEM) observations. Moreover, the core structure of the complex 60° dislocation pair, which may be taken as a Lomer dislocation, has been hardly reported. Subsequent to the recent developments in TEM [17, 18], high-angle annular dark-field (HAADF) imaging or Z-contrast imaging has been applied to determine the precise location and identity of individual atom and clusters [19, 20], with sub-angstrom resolution.

In this chapter, we have carried out an extensive investigation of the growth of GaSb on GaAs by MBE, by monitoring the substrate surface reconstructions, chemical treatment and growth temperature between 460 ^{o}C and 530 ^{o}C. Within the used growth conditions, although the strain relaxation is better at 510 ^{o}C, the growth mode is three dimensional (3D) and up to 40-50 monolayers (MLs), the film coalescence is not yet complete whereas at lower growth temperature a quasi-2D growth mode occurs. We propose a strain relaxation model which is able to account for the formation of misfit dislocations in high as well as in low lattice mismatched systems. In addition to HRTEM, atomic resolution STEM and molecular dynamic (MD) simulation have been applied to determine the atomic configuration of misfit dislocations. The dislocation density tensor analysis is next used to quantify the Burgers vector of misfit dislocations. This precise measurement reveals the misfit dislocation formation mechanism at highly lattice mismatched GaSb/GaAs interface, which is in good agreement with model we proposed. In addition, the local rotation which may be associated with mixed type dislocation was revealed by the analytical approach of the dislocation density tensor.

4.2 Growth mode dependence of misfit dislocation types and misfit dislocation formation model

4.2.1 Samples

Two series of samples have been grown for this investigation, as shown in Fig. 4.2. After substrate surface smoothing, the Ga and As valves were closed and the sample temperature was decreased to 465

°C, 480 °C, or 510 °C, for the growth of GaSb. As revealed by RHEED, the GaAs surface exhibits a Ga-rich (4x6) reconstruction. After an exposure to Sb flux for 5 seconds, this reconstruction evolves to a diffuse (1x4) one. Then 10 MLs GaSb were deposited for the first series of samples. The growth rate was 0.7 ML/s for the GaSb layers with a Sb flux of 2.5 ML/s, and a (1x3) surface reconstruction appeared during the GaSb deposition. The second series of samples with different epitaxial layer thickness (12, 15, 27, and 40 MLs) grown at 465 °C were also fabricated to investigate dynamic variation of the misfit dislocation and strain relaxation during the growth.

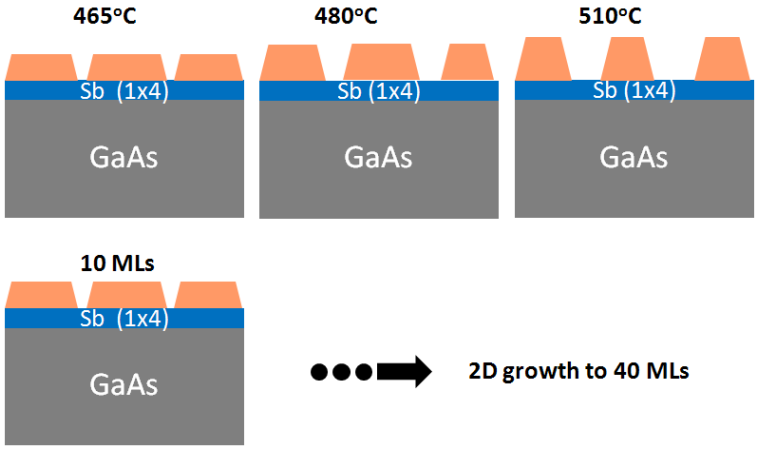

Figure 4. 2 Schematic diagrams of the two series samples involved in this section.

4.2.2 Misfit dislocation types versus growth mode

In order to analyze the surface structure of the samples, we performed weak beam dark filed (WBDF) observation in plan-view geometry. Figure 4.3 (a) and (b) show $(2\bar{2}0)$ WBDF images of the 10 MLs GaSb grown on GaAs at 465 °C and 510 °C, respectively. As can be noticed, at 465 °C, GaSb almost covers the entire GaAs surface indicating a quasi-2D growth mode. In contrast, the randomly distributed islands are indicative a 3D growth mode at 510 °C. The estimated coverage from plan-view images over 1 x 1 μm^2 are 84.1 %, 61.0% and 36.5%, for the samples grown at 465 °C, 480 °C and 510 °C, respectively.

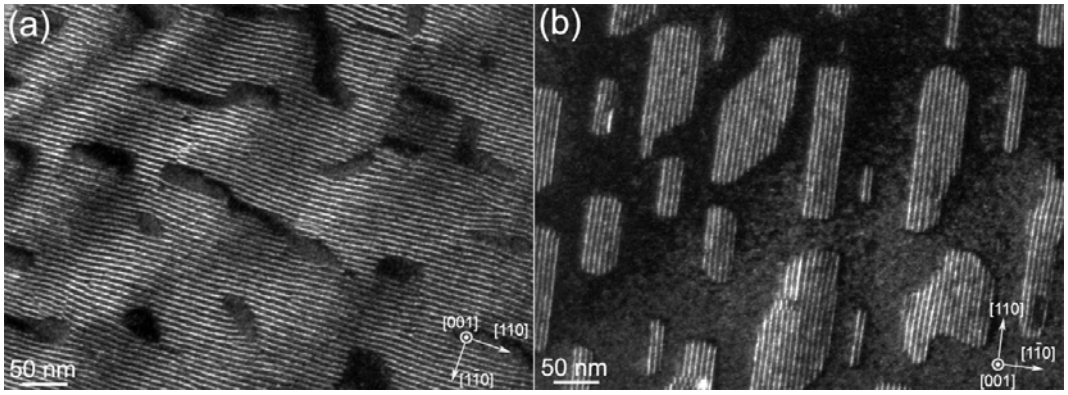

Figure 4. 3 The WBDF images showing the surface coverage of the samples in 2D and 3D growth modes, observed with $g = 2\bar{2}0$.

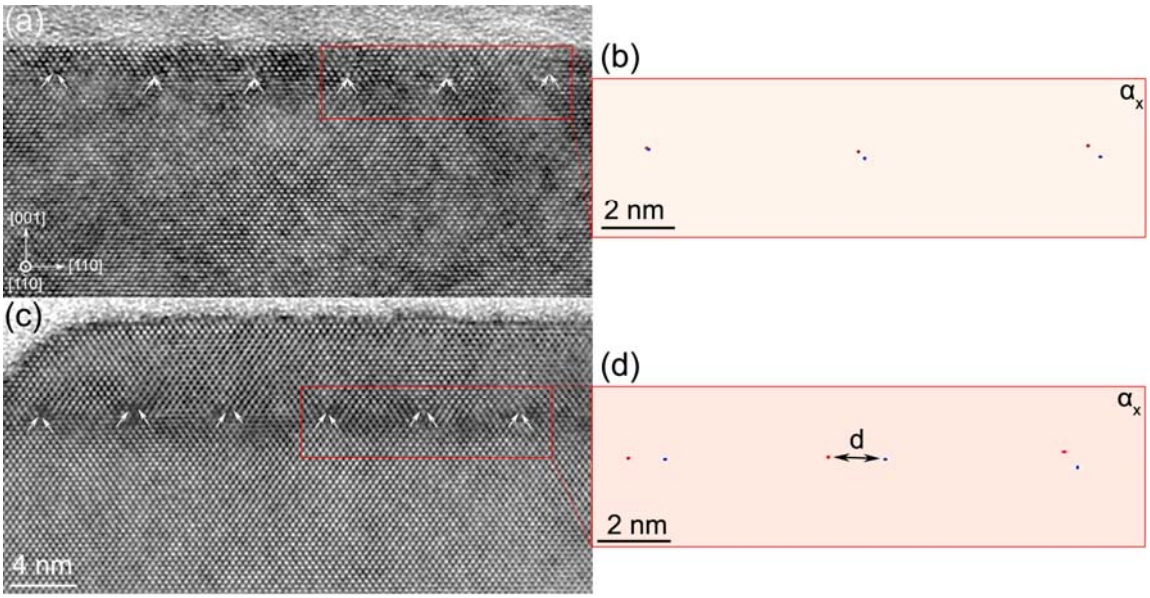

Figure 4. 4 (a) and (c) Cross-sectional HRTEM images of GaSb on GaAs observed along $[1\bar{1}0]$ *orientation. The inclined arrows indicate the extra {111} planes at the interface. (b) and (d) correspond to the* α_x *component of dislocation density tensor image from the highlighted area of HRTEM of (a) and (c) by GPA.*

Figure 4.4 shows the HRTEM images of the 10 MLs GaSb grown on GaAs at 465° C and 510° C observed along $[1\bar{1}0]$ direction. At 465° C the average GaSb thickness is 3.1 nm, whereas it is 6.3 nm at 510° C, with the same amount of GaSb deposited on the substrate.

Figure 4.4 (b) and (d) show the α_x component of the dislocation tensor field derived from the highlighted area of Fig. 4.4 (a) and (c), respectively. Using this dislocation density tensor image, we can not only get the edge component of the misfit dislocation Burgers vector by integrating the in-plane component over the dislocation core region [6, 21]. As can be seen in Fig. 4.4, the cores of the misfit dislocations in 2D growth mode (Fig. 4.3 a) are more compact than those in 3D growth mode (Fig. 4.4 (c)). The distances between these cores pair have been determined in many areas (more than 50 pairs of dislocation for each sample), the results are presented in Fig. 4.5. The spacing of the cores pair are highly related to the growth mode. In the samples with 10, 15, and 27 MLs grown at 465°C (2D growth mode), most of the

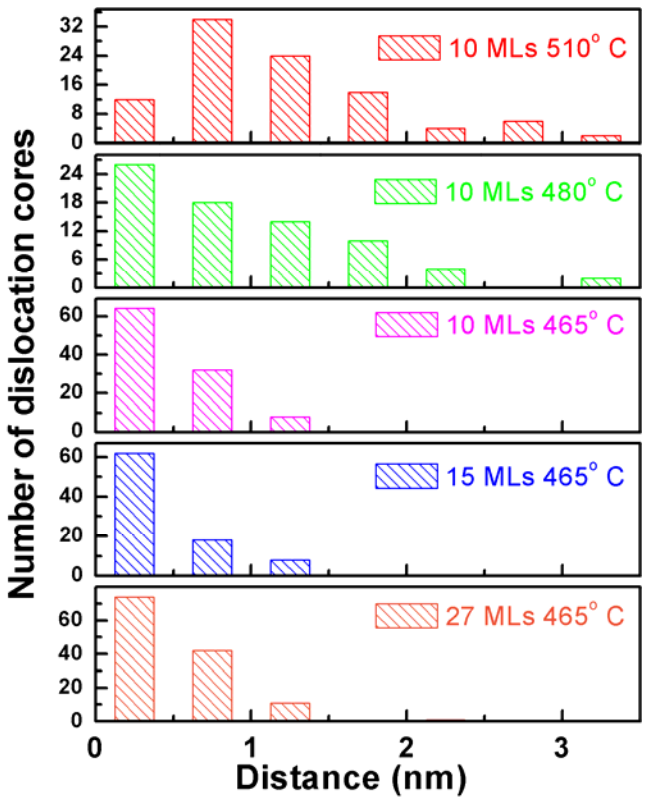

Figure 4. 5 The distance (d, as shown in inset of Fig. 4.4(b)) between the interface 60° dislocation pair versus the growth conditions.

misfit dislocations are Lomer type. At higher growth temperature (3D growth mode), both Lomer dislocations and closely spaced 60° dislocation pairs are observed. The latter are characterized by two additional intersecting lattice planes and a core separation larger than 1 nm.

4.2.3 Misfit dislocation formation model

During the initial growth, in the 2D growth mode, the epitaxial layer is highly strained. When the GaSb layer reaches the critical thickness (2-3 MLs) a first set of 60° dislocation is generated as half loops, which glide toward the interface and form misfit segments, as schematic shown in Fig. 4.6 (a). Subsequently, the second set of 60° dislocation nucleates and also glides to the interface. If the incoming 60° dislocations have opposite screw components (b_{1s}= -b_{2s}), they will react with those already at the interface and form 90° (or Lomer) dislocations, otherwise, they are likely to give rise to closely spaced 60° pairs as their parallel screw components (b_{1s}= b_{2s}) prohibit their recombination. Unlike the 2D growth

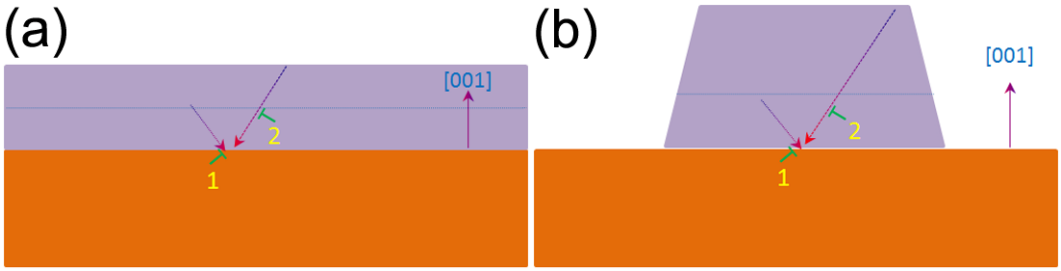

Figure 4. 6 The schematic formation mechanism of the misfit dislocations in 2D (a) and 3D (b) growth modes. The dotted horizontal line shows the critical thickness (d_c) for the formation of the first set of misfit dislocation; given in 2D growth mismatch strain accumulated in the continuum layer is faster than in the 3D islands, the d_c in 2D growth is expected smaller than in 3D growth.

mode the mismatch strain is directly relaxed via the formation of misfit dislocations, in the 3D growth, the initial strain is relaxed via the formation of coherent 3D islands after the growth of 1 or 2 MLs [22] and then via the misfit dislocations after the island reaches a critical size. In the 3D islands the free surfaces are larger, the elastic energy is lower in comparison with a continue layer of the same thickness [23]. In addition, an island may also change its shape in order to reduce the strain energy and continue to increase its height, even after the first misfit dislocation formation [24]. Therefore, the

distance between the second and first set of dislocations in the 3D island is expected to be larger than in 2D continuously forming layer, as schematically shown in Fig. 4.6 (a) and (b).

In order to estimate the quantitative interaction between the two sets of 60° dislocations, we choose the interface set dislocations at the origin of the coordinates, and the second set of 60° dislocation which is

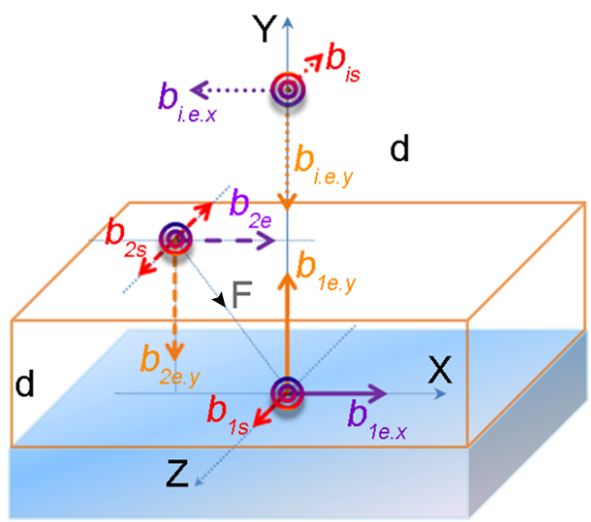

Figure 4. 7 The schematic arrangement of the 60° dislocations components. b_{1s}, $b_{1e.x}$, $b_{1e.y}$, b_{2s}, $b_{2e.x}$, and $b_{2e.y}$ being the screw, edge components of the first and second dislocations, respectively. $b_{i.s}$, $b_{i.e.x}$, and $b_{i.e.y}$ are the screw and edge components of the image dislocation.

nucleating on the free surface at height *d*, as shown in Fig. 4.7. Using the theory of straight dislocation [25], the mixed 60° dislocation can be treated as three dislocations: two pure edge dislocations with Burgers vector along [110] and [001] directions, a screw dislocation with Burgers vector along $[1\bar{1}0]$. In order to satisfy the boundary condition at the free surface, an image 60° dislocation with opposite sign ($b_{i.e.x}$=-$b_{e.x}$, $b_{i.e.y}$=-$b_{e.y}$ and $b_{i.s}$=-b_s) at the mirror position is also taken into account. As schematically shown in Fig. 4.7 (a), the dislocation being generated at the surface is submitted to the stress field generated by the dislocation already present at the interface as well as to that of the image dislocation outside the layer. Then within this stress field, the force on the surface dislocation could be calculated. The details of this calculation can be found in Appendix I.

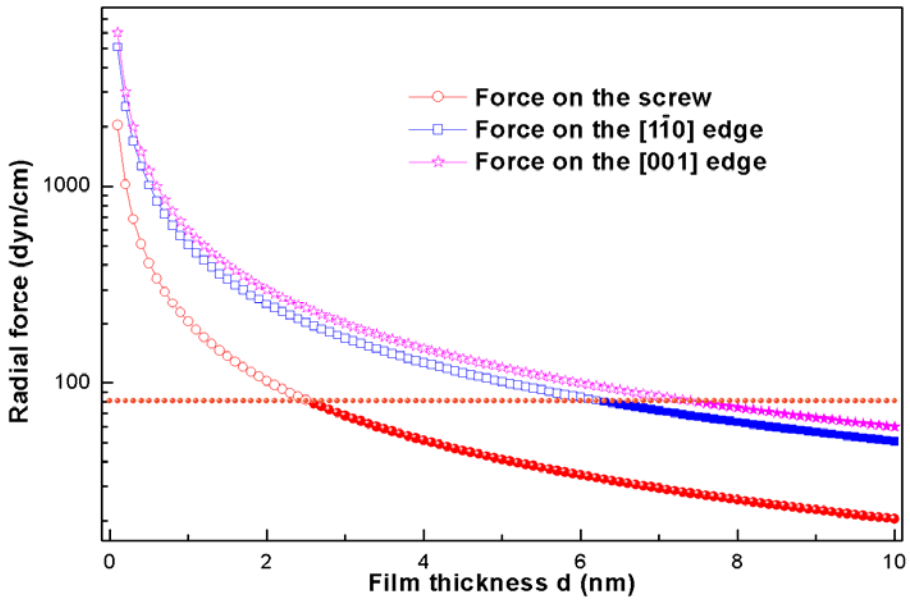

Figure 4. 8 The amplitude of the radial force (direction as shown in Fig.4.7 (a)) on 3 components (x axis edge component, y axis edge component, and z axis screw component) of the surface 60° dislocation as the function of the epitaxial layer thickness d.

Figure 4.8 shows the amplitude of the force as a function of the epitaxial layer thickness *d*. The force on the edge component of the incoming dislocation is about 2.74 times ($f_{e.y}/f_{e.x}$=1.186, $f_{e.x}/f_s$=2.473) larger than that on the screw component. The amplitude of the force can now be compared with the surface tension of GaSb indicated by the dotted line, for which we obtain 81 dyn/cm from references [26] and [27] by averaging (4x3) calculated surface reconstructions to yield an overall (1x3) symmetry for the Sb-rich surface. Assuming the atoms on the surface to be highly mobile, the edge component of the surface dislocation is determined by the first one (the interface dislocation). This explains why for the closely spaced 60° dislocation pair the glide plane is intersecting at the interface region (the cores distance is small see Fig. 4.5). Since for the screw component of the 60° dislocation forming at the surface, the interaction is weak, therefore, the control of its orientation is expected to highly depend on the distance between the two dislocations. Indeed, if the surface tension, which is also acting on the generated dislocation, is taken into account, it may be assumed that when the two forces are comparable, the direction of the screw component can be determined by the interface 60° dislocation. Therefore, when the

layer thickness or the island height increases further, this force becomes smaller than the surface tension. As a consequence, the Burgers vector of the screw component of the incoming 60° dislocation will depend on the surface geometry and tend to be randomly parallel or anti-parallel. As shown in Fig. 4.6, this is probably a major difference between the 2D and 3D growth modes, which could lead to the discrepancy in the generated configurations of corresponding misfit dislocations.

It is necessary to assess the above observations and the proposed mechanism in the light of those available in the literature for the formation of the interface misfit dislocations in III-V zinc-blende semiconductors. An important observation from our HRTEM data analysis is the systematic presence of the 60° dislocation pairs at the interface, which attests that the two dislocations have been gliding towards the interface and have not been able to recombine due to their parallel screw components. Therefore, it may be noticed that such a configuration may not result from a spontaneous formation of the Lomer dislocation network as has been proposed in recent reports [10, 12]. In our growth conditions, no stacking faults have been observed, so the involvement of partial Shockley dislocations in the formation of the Lomer interface dislocations may not apply in our case [9].

An additional observation is shown in Fig. 4.9, keeping the 2D growth mode, we have increased the thickness of GaSb until 40 MLs, as can be noticed, there is an improvement of the strain relaxation state (blue open square) and average distance of Lomer dislocations (red open circle) as the function of the GaSb thickness. This decrease of the distance of the Lomer dislocations indicates that the formed Lomer dislocations could be redistributed slightly by glide along the interface, in order to minimize the strain energy. As mentioned in Ref. [8], the advantage of the rebound model for the misfit dislocation formation is that it leads to regularly spaced Lomer dislocations which perfectly relieve the misfit strain. Therefore, the evolution of the average distance between the Lomer dislocations and the presence of 60° pairs which are pointed out here may not be easy to take into account such a model. In agreement with Ref. [1] and [5], it may also be stated that the pure glide model, with the 60° dislocations which meet at the interface is not completely satisfactory as it may only lead to a random distribution (in type and distances)

of the interface dislocations. In the above observations the surface also appears to play an important role for the interface misfit relaxation. In the 2D growth mode of highly mismatched GaSb/GaAs system, the change in Lomer dislocation distance with the number of deposited MLs is a strong indication that the strain relaxation is a dynamic process.

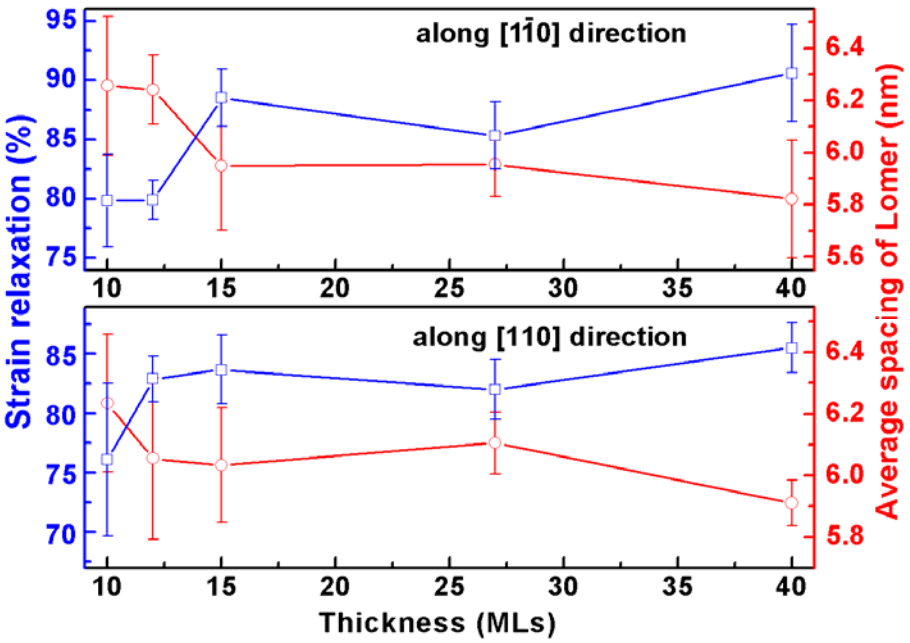

Figure 4. 9 The strain relaxation (blue open square) and average distance of Lomer dislocations (red open circle) as a function of epitaxial layer thickness in 2D growth mode.

Now, it is possible to compare our results to the early reports which showed that low strain systems (<2%) resulted in 60° dislocations, moderate strain (3–4%) in mixed Lomer and 60° dislocations, and high strain >6% in pure Lomer [28]. Taking into account the role of the surface, the proposed mechanism also applies for the small lattice mismatched systems where the misfit dislocations network is dominated by the 60° dislocations [29]. Indeed, due to the small mismatch, the strain energy in the epitaxial layer is small and the critical thickness for the generation of misfit dislocations is large. Thus, the interaction between the 60° dislocations at the interface and at the surface is weak, which means that the influence on the Burgers vector of the surface 60° dislocation is negligible.

4.3 The atomic configuration of the misfit dislocation and their formation mechanism

4.3.1 Samples

In this section, 3 Sb rich (2x4), (2x8), or (1x4) surfaces reconstructions of GaAs were involved as schematically shown in Fig. 4.10. Then on each of these surfaces, 10 monolayers (MLs) GaSb were deposited at 485°C. The growth rate was 0.7 ML/s for the GaSb layers with a Sb flux of 2.5 ML/s. The Z contrast HAADF images were acquired using a FEI Titan 80-300 Cubed Microscopy equipped with a objective spherical aberration (C_s) corrector operated at 300 kV, along [110] and $[1\bar{1}0]$ zone axis. The convergence semi-angle of the electron probe was 9 mrad, and the collection semi-angle for the HAADF imaging was 70 to 200 mrad. The C_s in STEM mode is 1.2 mm, thus the probe resolution is 1.36 Å which is below the distance of Ga-Sb dumbbell (1.52 Å) along [001].

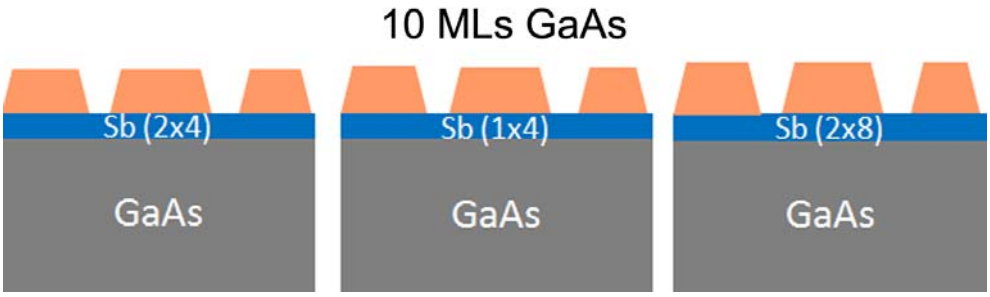

Figure 4. 10 The diagrams of the sample involved in this section.

4.3.2 The atomic configuration of the misfit dislocation

Figure 4.11 shows a HAADF-STEM image of the GaSb epitaxial layer on GaAs substrate with (2x4) surface reconstruction observed along the [110] zone axis. In this image the bright and dark region correspond to the GaSb and GaAs, respectively, due to their different atomic number (Z). As can be seen that the interface is flat at atomic level and all the misfit dislocations cores locate at the GaSb/GaAs

interface. The atomic-level flat interface indicates that the intermixing of the group V element (As/Sb here) was prohibited by the surface preparation.

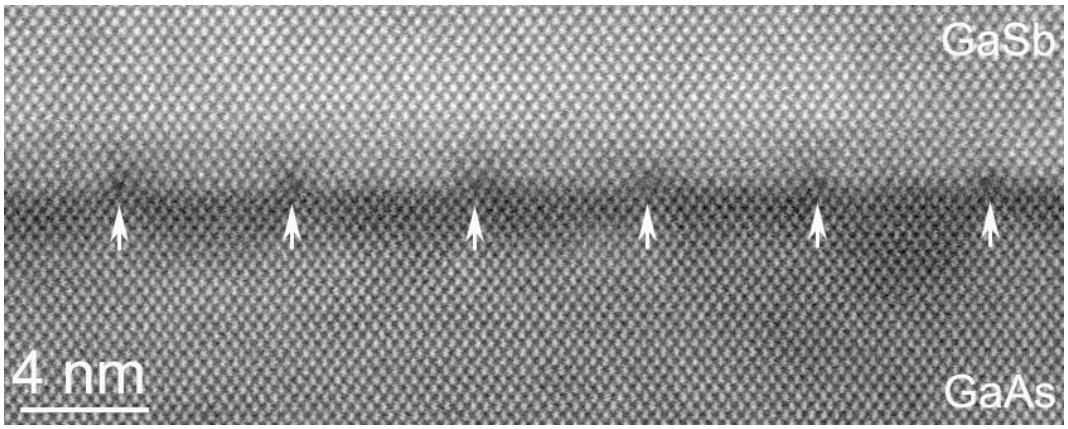

Figure 4.11 HAADF-STEM image of GaSb epitaxial film on GaAs observed along [110] zone axis, misfit dislocations are marked by the arrows.

Figure 4.12 shows higher magnification HAADF image at the dislocation core region. Since the image intensity in HAADF image is approximately proportional to the square of the atomic number (Z) in 1s approximation [30, 31], the bright spots in the epitaxial layer correspond to Sb atomic columns, as can be seen in the line intensity profile in Fig. 4.12 (c).

Superimposing the atomic model of the Lomer dislocation core, which is generated by MD simulation, reveals that dislocation 2 is a shuffle set Lomer dislocation characterized by a 5/7-atom ring configuration [32, 33]. Unlike dislocation 2, the higher image intensity in dislocation 1 core center indicates an atomic column inside, as shown in Fig. 4.12 (d). By inspecting the adjacent dumbbells, it can be inferred that the core atomic column is Ga. The presence of a single atom column in dislocation 1 core center yields a glide set Lomer dislocation core with an 8-atom ring configuration [32] [33]. Fig.4.12 (b) shows an area with a 60° dislocation pair, in contrast to the Lomer dislocation, as can be noticed that the two additional {111} planes do not terminate in one atomic ring.

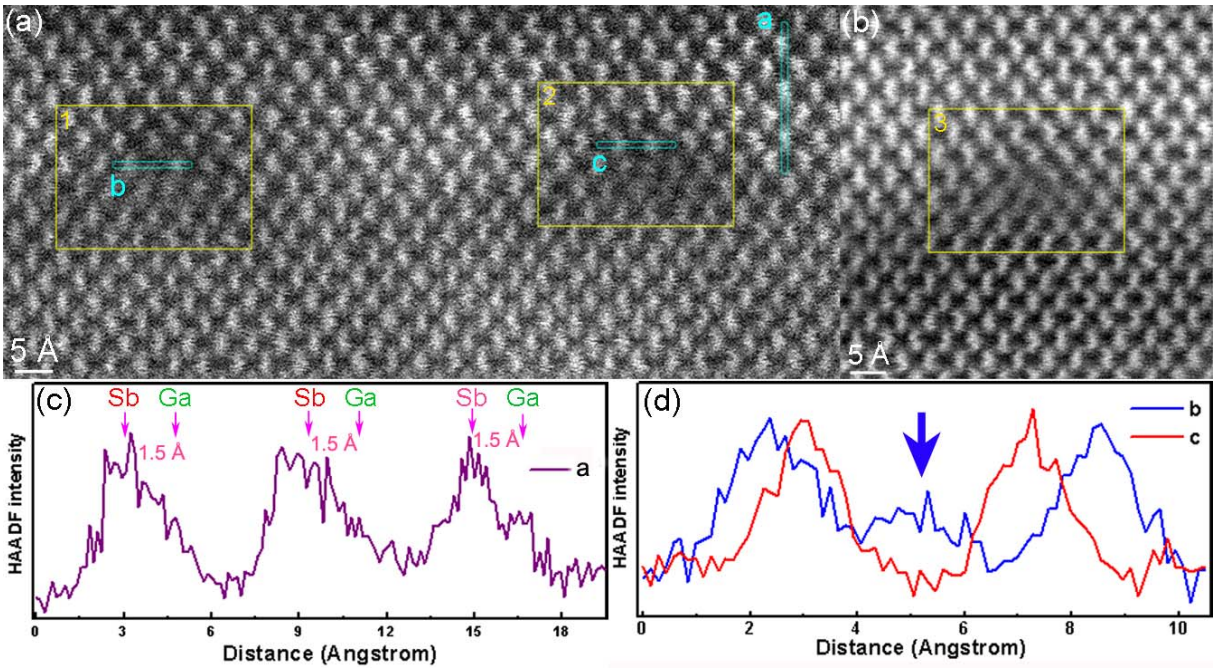

Figure 4.12 (a) and (b) High resolution HAADF-STEM images of GaSb epitaxial film on GaAs with (2x4) surface reconstruction; the zone axis is along the [110] GaAs. (c) and (d) the image intensity profiles along the atomic planes indicated by the line a, b and c, respectively.

Figure 4.13 (a), (b), and (c) show the simulated HAADF images of the corresponding atomic models obtained by MD simulation with a thickness of 10 nm, using the QSTEM software [34] for the C_s=1.2 mm of our non probe corrected microscope. The detailed procedure and parameters of this image simulation are given in Chapter 2. The simulated images reproduce the atomic distortion in the dislocation core region and exhibit good agreement with the experimental HAADF images, which confirms the proposed core configurations. As shown in Fig. 4.13 (d), a line intensity profile (the profile is acquired on the image with larger scanning area, not shown here) along [001] enables us to identify the Sb and Ga atomic columns. Acquiring the line profiles (Fig. 4.13 (e)) across the dislocation 1 and 2 on the simulated images as shown in Fig. 4.13 (a) and (b), exhibits similar results as the experimental one (Fig. 4.12 (d)) indicating that the glide and shuffle set dislocations could be identified in our working conditions. Fig. 4.13 (f), (g) and (h) display the highlighted dislocation core area superimposed with glide and shuffle sets

of the Lomer dislocation and 60° dislocation pair atomic model, respectively. On 30 analyzed dislocations, the shuffle set Lomer dislocation with As atomic column core presents 26 times (86.7 %). Then, two glide set type Lomer dislocations (6.7 %) with Ga atomic column core as well as two 60° dislocation pairs (6.7 %) have also been observed at this interface.

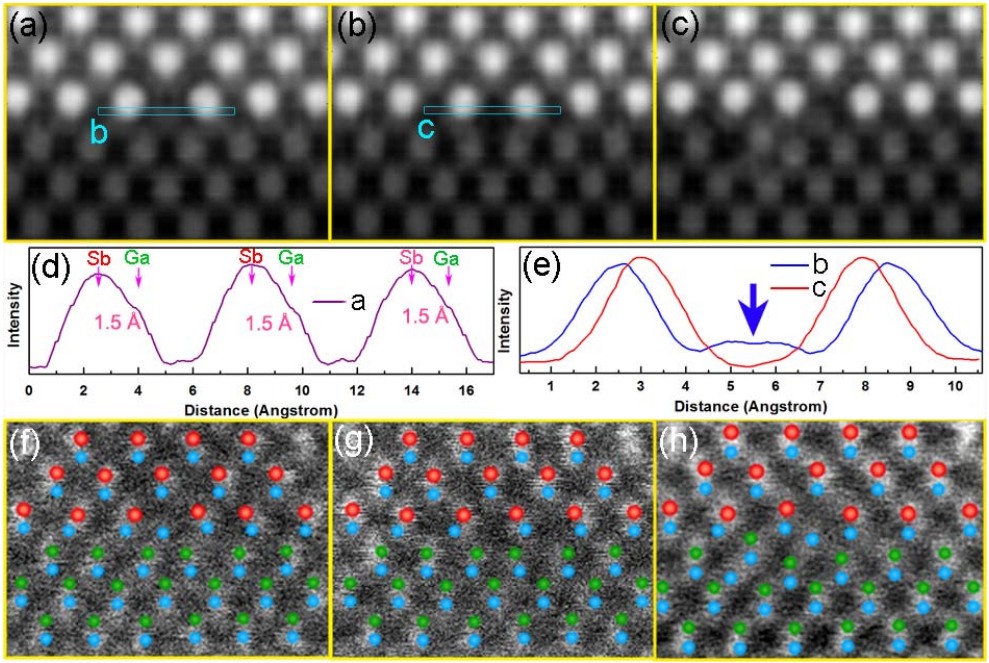

Figure 4.13 (a), (b), and (c) show the simulated HAADF images. (d) the image intensity profile along [001] atomic columns on a larger area (similar to the line a in Fig.4.12(a)). (e) the line intensity profiles across the simulated dislocation cores indicated by lines b and c. Figure 4.13 (f), (g) and (h) show the experimental images superimposed with the atomic models, glide set (1), shuffle set (2) Lomer dislocations, and 60° dislocations pair (3), respectively.

4.3.3The configuration stability of the misfit dislocation

The relative stability of the Lomer dislocations core has been investigated by molecular dynamic simulation. The relaxation of the GaSb/GaAs hetero-structure was performed by MD simulation using the Stillinger-Weber potential [32, 35]. The details of the computational procedure as well as the parameters of Stillinger-Weber potential have been given in Chapter 2. During the calculation, 6 possible Lomer

dislocations were taken into consideration. After relaxation, the atomic structures of these Lomer dislocations at core region are surmised in Fig. 4.14.

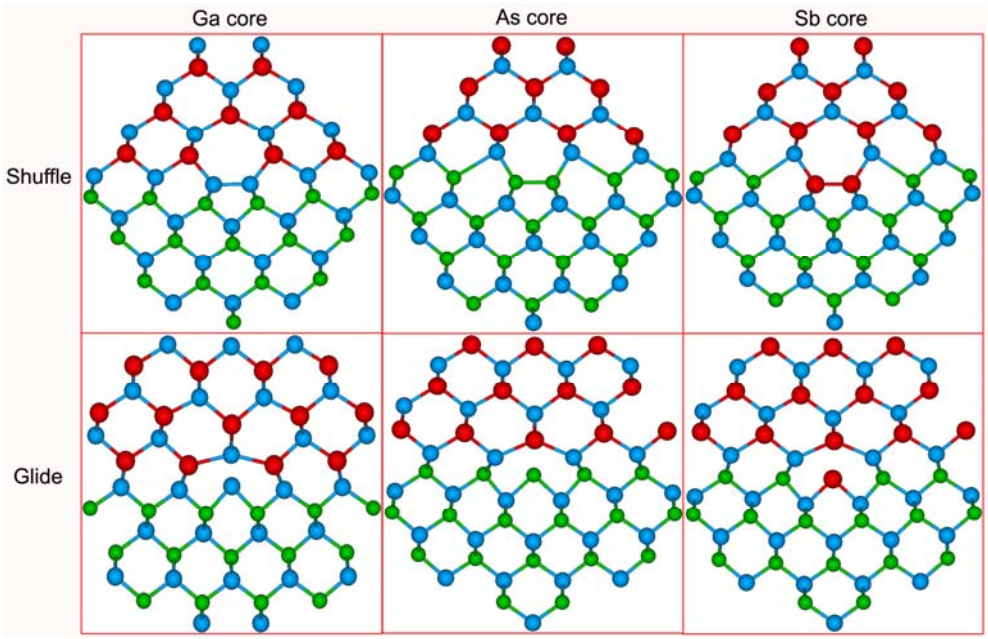

Figure 4.14 Relaxed atomic structure of the Shuffle and Glide dislocations cores with different core atom. Red, green, and blue balls represent Sb, As, and Ga atoms, respectively.

Following Hirth and Lothe [25], the energy per unit length of a dislocation is calculated in a cylinder of radius R, as $E(R) = \frac{G|b|^2}{4\pi(1-\nu)} \ln\left(\frac{R}{R_c}\right) + E_c$, ($R \geq R_c$), where G is the shear modulus, ν is the poison's ratio, b is the burgers vector, R_c is the core radius, and E_c the core energy per unit length. Besides the atomic configuration of the interface, as mentioned in the previous paragraph, the MD calculation also provides the system total energy projection on a single atom j (E_j). Summing over all the atoms in a cylinder of radius R and length L oriented along the dislocation line (as schematically shown in inset of Fig. 4.15), one obtains the energy per unit length of a dislocation as $E\ (R) = \frac{1}{L} \sum_{c(R,L)} E_j$.

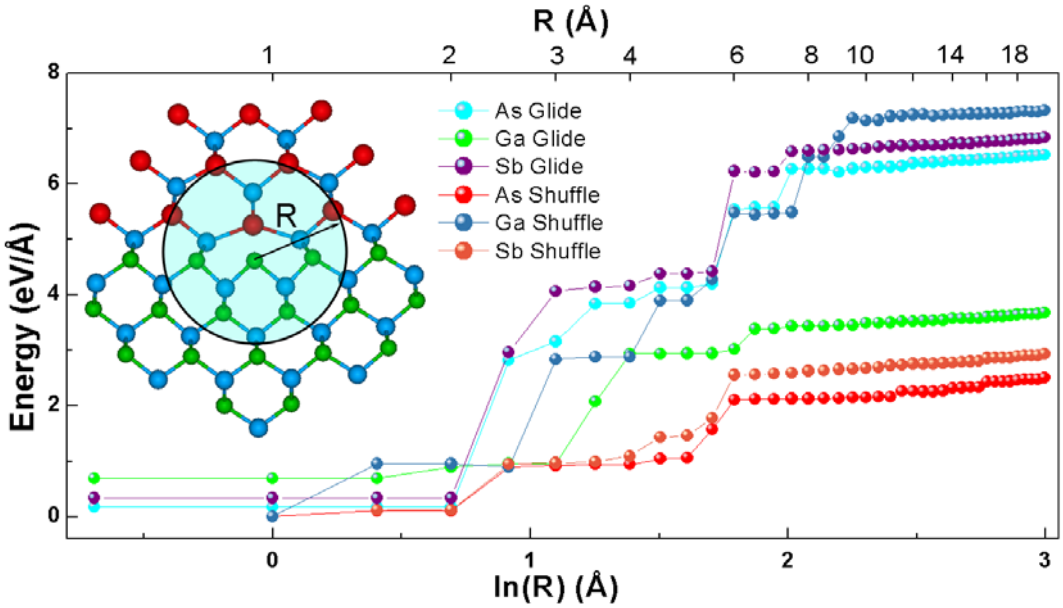

Figure 4.15 The energy per unit length (eV/Å), $E_f(R)$ for the different Lomer dislocations plotted as a function of distance from the dislocation core center. The energy is evaluated for a cylinder of radius R around the dislocation core, as schematically shown by the inset. The calculated core energy (E_c), core radii (R_c), and shear modulus (G) of the Lomer dislocations are summarized in Table 4.1.

Figure 4.15 shows the energy per unit length for the different Lomer dislocations atomic configurations plotted as a function of distance from the core center. Using a linear fit, the core radius R_c, core energy E_c and shear modulus G are extracted and summarized in Table 4.1, they correspond to the position when the linear behavior breaks down. As shown in Fig. 4.15, the As shuffle set core Lomer dislocation has the lowest core energy of the calculated atomic configurations. This indicates that the As shuffle set core Lomer dislocation is the most stable configuration. These results are in agreement with the above STEM observations.

Table 4. 1 The calculated core energy (E_c), core radii (R_c), and shear modulus (G) of the Lomer dislocations.

	As Glide	Ga Glide	Sb Glide	As Shuffle	Ga Shuffle	Sb Shuffle
R_c (Å)	7.5	6.5	7.5	6	9	6
E_c (eV/Å)	6.2	3.4	6.6	2.0	7.1	2.5
G (GPa)	26.2	22.6	25.1	33.0	26.3	28.5

Another issue I would like to mention here is the validation of this cylinder method. This cylinder method are based the elasticity theory, as we shown in chapter 2. In our case the dislocations locate at interface where the elasticity theory maybe not valid. However, all the extracted shear modulus is localized in a reasonable region (the shear modulus of GaSb and GaAs are 24.1 GPa and 32.5 Gpa, respectively). These may more or less indicates that the cylinder method is valid in our case.

4.3.4 The Burgers vector of the misfit dislocation and their formation mechanism

In order to determine the misfit dislocation formation mechanism and to quantify the Burgers vector of the dislocations, we performed dislocation density tensor analysis. The image processing procedure for the dislocation density tensor has been discussed in Chapter 2. Fig. 4.16 (a) and (b) show the α_x and α_y components of the dislocation density tensor of a shuffle set Lomer dislocation presented in Fig. 4.16 (a). The bright / dark dots present the maximum deformation area and mark the origin of each extra {111} plane. The corresponding 3D representative of dislocation density tensors at core region are inset into the Fig. 4.16 (a) and (b), respectively. The distance between the two peaks is less than 1 Å, and the calculated α_x components are very close to the theoretical value for Lomer dislocation ($b = \frac{a}{2}[1\bar{1}0]$ = 4.0 Å). Integrating the α_y component in the dislocation core region yields zero; this is consistent with the nature of the Lomer dislocation which is a pure edge dislocation with Burgers vector at 90° to its dislocation line [36]. Integrating the two peaks of the Lomer dislocation separately, in a_x component we obtain two Burgers vectors corresponding to α_x components of two 60° dislocations (2.0 Å); in α_y component, the two Burgers vectors have equal amplitude (2.85 Å) but opposite directions. It can be noticed that for each separate core the α_y component is 1.4 times larger than the a_x component, as one would expect from the geometrical projection, but in contrast to an earlier work which reported that the α_y should be equal to the α_x [4].

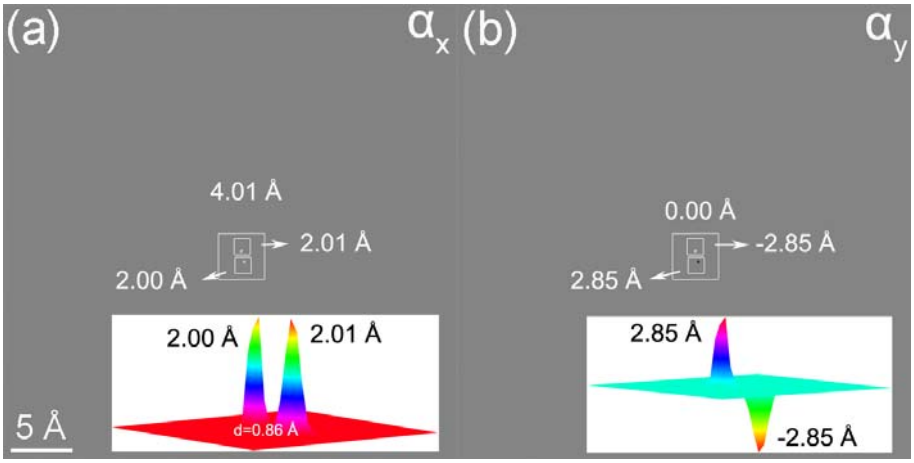

Figure 4.16 Dislocation density tensor components α_x (a) and α_y (b) of the Lomer dislocation from Fig. 4.12 (a); the insets show corresponding 3D representative of the dislocation density tensor α_x and α_y components in the dislocation core region, d is the distance between the two peaks.

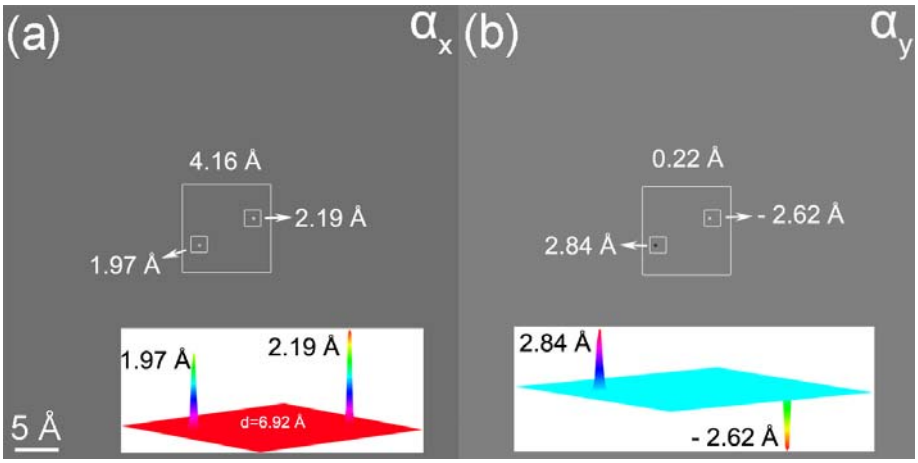

Figure 4.17 Dislocation density tensor components α_x (c) and α_y (d) of the 60° dislocation pair from Fig. 4.12 (b); the insets show corresponding 3D representative of the dislocation density tensor α_x and α_y components in the dislocation core region, d is the distance between the two peaks.

As done above for the Lomer dislocation, we have performed the Burgers vectors analysis on a 60° dislocations pair. Fig. 4.17 (a) and (b) show the dislocation density tensor images of a 60° dislocation pairs from Fig. 4.12 (b) in 2D and 3D view. The two 60° dislocation cores are separated by a distance of 7 Å. In this case and in contrast to the Lomer dislocation, the a_x and a_y components of 60° dislocations pair

are 4.2 and 0.2 Å, which means that besides the $[1\bar{1}0]$ edge component, we have a small residual edge component along [001] direction.

From the HAADF observation, it can be pointed out that one may confuse a 60° dislocations pair with a Lomer dislocation, especially when the two 60° dislocation cores are so close. In both case, one has two intersecting {111} planes and drawing the Burgers vector circuit, the 60° dislocations pair will give the same Burgers vector as a Lomer dislocation. However, with the help of the dislocation density tensor analysis, the Burgers vector can be measured precisely and a 60° dislocations pair clearly distinguished from a Lomer dislocation. Similar analyses have been carried out on the samples grown subsequent to (2x8) and (1x4) surface reconstructions. Though, they have different ratios for each type of misfit dislocation, they are all characterized by the same feature: each dislocation exhibits two local peaks in the density tensor (as shown in Fig. 4.16), which is a clear indication that they are generated by the same formation mechanism.

From the above observations, it is clear that a general mechanism should take into account the formation of 60° dislocations pairs at the interface. It can be concluded that in this material system, the relaxation of the misfit strain proceed predominantly by the glide of 60° dislocations from the layer surface. Subsequently, if the two reacting 60° dislocations have opposite screw components, they will react into a Lomer dislocation (as shown in Fig. 4.18 (b)); otherwise, they are likely to give rise to a 60° dislocations pair as their parallel screw components prohibit their combination (as shown in Fig. 4.18 (c)). This conclusion is in good agreement with our proposed misfit dislocation formation model. This analytical approach of the dislocation density tensor provides another dimensional proof of our misfit dislocation formation model.

Due to the 7 % of 60° dislocation pair, the mismatch strain in the epitaxial layer is no fully relieved (the measured residual strain by GPA is 5.3 %). Moreover, according to Narayan et al. [5] the 60° dislocations pair may not recombine to form a Lomer dislocation even by post annealing, in contrast they are likely to

split and form stacking faults in the epitaxial layer, as well as probably threading dislocations in the worst cases.

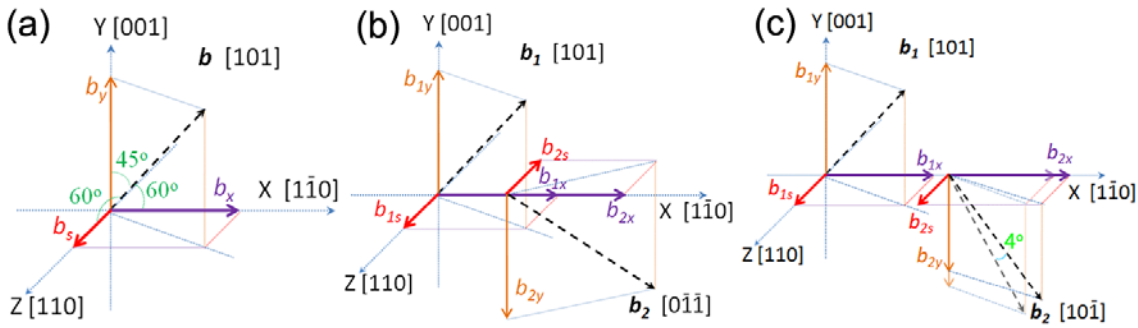

Figure 4.18 The schematic geometry diagrams of a 60° dislocation (a) and of the reaction two 60° dislocations in Cartesian coordinate system: the Lomer dislocation (b), and the 60° dislocations pair (c). Here, b indicate the Burgers vector, b_{is}, b_{ix} and b_{iy} represent the screw, x direction and y direction edge components of dislocation i, respectively. In Fig. (c) the corresponding shade lines indicate the perfect oriented 60° dislocation, 4° is the angle between the rotated 60° dislocation and a perfect oriented 60° dislocation.

By comparing the measured Burgers vectors with theoretical ones, we are able to determine the local rotation due to the 60° dislocation pair. For instance, in the 60° dislocation pair of Fig. 4.17, the left side 60° dislocation is perfectly oriented with a_x and a_y components almost equal to the ideal ones, i.e. 1. 97 Å and 2.84 Å, respectively. However, the right side 60° dislocation whose a_x and a_y components are 2.19 Å and 2.62 Å, yields a screw component of 2.08 Å. By comparison with an ideal 60° dislocation whose Burgers vector lies along $[10\bar{1}]$ direction, the right side 60° dislocation deviates 4° from the $[10\bar{1}]$ direction, as schematically shown in Fig. 4.18 (c).

4.4 Conclusion

The obove investigation shows that a 2D growth promotes Lomer dislocations with compact cores, whereas 60° dislocations and closely spaced 60° pairs predominantly form during 3D growth. We propose a misfit dislocation formation model where the 60° dislocations glide from the surface and react at the

interface. There is a competition between the interaction of the two 60° dislocations and the surface tension which governs the direction of screw component of the surface 60° dislocation and thereby determine the type of the final misfit dislocation. What is more, the model accounts for the misfit dislocations types that will be generated during the hetero-epitaxy of high and low mismatched III-V semiconductors in the zinc-blende structure.

The atomic configuration of the misfit dislocations was investigated by the STEM-HAADF, the analysis shows that the shuffle set Lomer dislocation with a core made of two As atomic columns is the predominant misfit dislocation at the GaSb/GaAs interface in agreement with MD simulations.

Reference

[1]P. M. J. Marée, J. C. Barbour, J. F. van der Veen, K. L. Kavanagh, C. W. T. Bulle-Lieuwma, and M. P. A. Viegers, J. Appl. Phys. **62**, 4413 (1987).

[2]A. Vilà, A. Cornet, J. R. Morante, M. Loubradou, R. Bonnet, Y. González, L. González, and P. Ruterana, Philos. Mag. A **71**, 85 (1995).

[3]A. Vilà, A. Cornet, J. R. Morante, P. Ruterana, M. Loubradou, and R. Bonnet, J. Appl. Phys. **79**, 676 (1996).

[4]A. Rocher and E. Snoeck, Mater. Sci. Eng.: B **67**, 62 (1999).

[5]J. Narayan and S. Oktyabrsky, J. Appl. Phys. **92**, 7122 (2002).

[6]Y. Wang, P. Ruterana, L. Desplanque, S. El Kazzi, and X. Wallart, J. Appl. Phys. **109**, 023509 (2011).

[7]S. A. Dregia and J. P. Hirth, J. Appl. Phys. **69**, 2169 (1991).

[8]C.H. Henager Jr. and R.G. Hoagland, Scripta Materialia **50**, 701 (2004).

[9]Y. Chen, X. W. Lin, Z. Liliental-Weber, J. Washburn, J. F. Klem, and J. Y. Tsao, Appl. Phys. Lett. **68**, 111 (1996).

[10]S. Huang, G. Balakrishnan, and D. L. Huffaker, J. Appl. Phys. **105**, 103104 (2009).

[11]A. Jallipalli, G. Balakrishnan, S. H. Huang, T. J. Rotter, K. Nunna, B. L. Liang, L. R. Dawson, and D. L. Huffaker, Nanoscale Res. Lett. **4**, 1458 (2009).

[12]S. Huang, *Microscopy Study of Extreme Lattice Mismatched Heteroepitaxy Using Interfacial Misfit Arrays*, The University of New Mexico, 2007.

[13]A. J. McGibbon, S. J. Pennycook, and J. E. Angelo, Science **269**, 519(1995).

[14]S. Lopatin, S. J. Pennycook, J. Narayan, and G. Duscher, Appl. Phys. Lett. **81**, 2728 (2002).

[15]J. N. Stirman, P. A. Crozier, D. J. Smith, F. Phillipp, G. Brill, and S. Sivananthan, Appl. Phys. Lett. **84**, 2530 (2004).

[16]S. H. Vajargah, M. Couillard, K. Cui, S. G. Tavakoli, B. Robinson, R. N. Kleiman, J. S. Preston, and G. A. Botton, Appl. Phys. Lett. **98**, 082113 (2011).

[17]M. Haider, S. Uhlemann, E. Schwan, H. Rose, B. Kabius, and K. Urban, Nature **392**, 768 (1998).

[18] S. J. Pennycook and L. A. Boatner, Nature **336**, 565 (1988).

[19]P.M. Voyles, D.A. Muller, J. L. Grazul, P. H. Citrin, and H.-J. L. Gossmann, Nature **416**, 826 (2002).

[20]M. Couillard, G. Radtke, A. P. Knights, and G. A. Botton, Phys. Rev. Lett. **107**, 186104 (2011).

[21]S. Kret, PawelDlużewski, P. Dlużewski, and E. Sobczak, J. Phys.: Conden. Matter **12**, 10313 (2000).

[22]B.A. Joyce, D.D. Vvedensky, A.R. Avery, J.G. Belk, H.T. Dobbs, and T.S. Jones, Appl. Surf. Sci. **130–132**, 357 (1998).

[23]C. W. Snyder, J. F. Mansfield, and B. G. Orr, Phys. Rev. B **46**, 9551 (1992).

[24]F. K. LeGoues, M. C. Reuter, J. Tersoff, M. Hammar, and R. M. Tromp, Phys. Rev. Lett. **73**, 300 (1994).

[25]J. P. Hirth and J. Lothe, *Theory of Dislocations* (Krieger Pub. Co., 1982).

[26]J. Houze, S. Kim, S.-G. Kim, S. C. Erwin, and L. J. Whitman, Phys. Rev. B **76**, 205303 (2007).

[27]C. Hogan, R. Magri, and R. Del Sole, Phys. Rev. Lett. **104**, 157402 (2010).

[28]R. E. Mallard and Wilshaw P R, Mason N J, Walker P J and Booker G R, Inst. Phys. Conf. Ser. **100**, 331 (1989).

[29]K. H. Chang, P. K. Bhattacharya, and R. Gibala, J. Appl. Phys. **66**, 2993 (1989).

[30]S.J. Pennycook, Advances in Image and Electron Physics **123**, 173 (2002).

[31]E. Carlino and V. Grillo, Phys. Rev. B **71**, 235303 (2005).

[32]Y. Wang, P. Ruterana, H. P. Lei, J. Chen, S. Kret, S. El Kazzi, L. Desplanque, and X. Wallart, J. Appl. Phys. **110**, 043509 (2011).

[33]Hornstra J, Journal of Physics and Chemistry of Solids **5**, 129 (1958).

[34]C. T. Koch, *Determination of Core Structure Periodicity and Point Defect Density Along Dislocations*, Arizona State University, 2002.

[35]F. H. Stillinger and T. A. Weber, Phys. Rev. B **31**, 5262–5271 (1985).

[36]D. Hull and D. J. Bacon, *Introduction to Dislocations* (Elsevier, 2011).

Chapter 5

General Conclusion and Perspective

5.1 Conclusion

In this work, we investigated the impact of initial growth parameters, such as surface treatment, AlSb interlayer, growth rate and growth temperature, … on the strain relaxation and misfit dislocation of GaSb. As a result, a misfit dislocation formation model was proposed and validated by a detailed analysis of misfit dislocation configurations and dislocation density tensors.

The main results that have been obtained are:

1. We have demonstrated that Sb-rich surface treatment promotes the formation of Lomer dislocation at the GaSb/GaAs interface; as well as in the epitaxy of GaSb on GaP.

2. The AlSb interlayer improves the interfacial quality and brings about flat interface. Combining the Sb-rich substrate surface treatment and 4MLs AlSb interlayer we have obtained relaxed GaSb layers (100 %) on GaAs and reduced the threading dislocation density to 10^7 cm^{-2}.

3. The analysis of the strain relaxation and the spacing of the misfit dislocations as a function of growth temperature and rate, predicts an optimal window for epitaxy of relaxed (95 %) GaSb epitaxial layers on GaP substrate.

4. With these optimized growth parameters, high mobility AlSb/InAs hetero-structures on GaAs and GaP substrates with a 600 nm thick GaSb buffer layer has been achieved.

5. We experimentally observed that a 2D growth mode leads to the formation of Lomer dislocations, whereas 3D growth mode results in 60° dislocation pairs. The interaction of 60° dislocations and the surface tension determine the type of the generated dislocations.

6. The core structure of the misfit dislocations was investigated by atomic resolution STEM HAADF as well as image simulation. The arsenic core shuffle set Lomer dislocation is found to be the dominant misfit dislocation.

7. The relative stability of the Lomer dislocations core has been investigated by the MD simulation. Shuffle set (5/7 - atoms core) Lomer dislocation with two Arsenic atoms in the center has the lowest core energy, which coincides with the experimental results.

8. The dislocation density tensor analysis proves that, in GaSb/GaAs interface the dominant mechanism underlying the formation of misfit dislocation is the glide and reaction of 60° dislocations. On the other hand, the analytical approach of the dislocation density tensor points out a new approach to determine the local rotation of the mixed type dislocations.

5.2 Perspective

1. As suggested by our dislocation formation model, three factors (growth temperature, substrate surface reconstruction, and surface tension) may be critical in the growth of high quality GaSb epitaxial layer: to begin with, we know that higher growth temperature leads to better strain relaxation; however, it results in the 3D growth mode. Therefore an optimized substrate surface reconstruction is needed so that one can balance the influence of growth temperature on the strain relaxation and growth mode. Then the surface tension should also be taken into consideration.

2. The second concern is the source of the threading dislocations. As has been reported [1, 2], there are two types of imperfections in the misfit dislocation network, as shown in Fig. 5.1: (1) the mismatch (shift) of the Lomer dislocation array (red arrows) and (2) an additional Lomer dislocation (green arrows). The shift of the Lomer network has been attributed to: (a) the interaction of a 60° dislocation with the network of the Lomer dislocations [2, 3]; (b) the presence of the monoatomic surface steps or demisteps at the

interface [4, 5]. The additional Lomer dislocation (or the termination of a Lomer dislocation at interface) means that this Lomer dislocation turned to a threading dislocation inside the epitaxial layer. Though its dislocation line may rapidly bend to {111} plane, its Burgers vector remains as a/2 <110>. Indeed, we have observed two types of threading dislocation, as shown in Fig. 5.2. We can identify that dislocation 1 (white circle) is a mixed type dislocation, and dislocation 2 (black circle) is an edge type dislocation. Similarly, Hojo et al. [6] recently reported the observation of two kinds of threading dislocations (one is pure edge type and the other is mixed-type) in CeO_2 thin film which also has cubic structure. We believe that they are connected with the imperfections of the misfit dislocations network as pointed out in the work of Rocher et al. [7]. As, this is just a preliminary result, more detailed work on determining the core structure of the threading dislocation would be welcome.

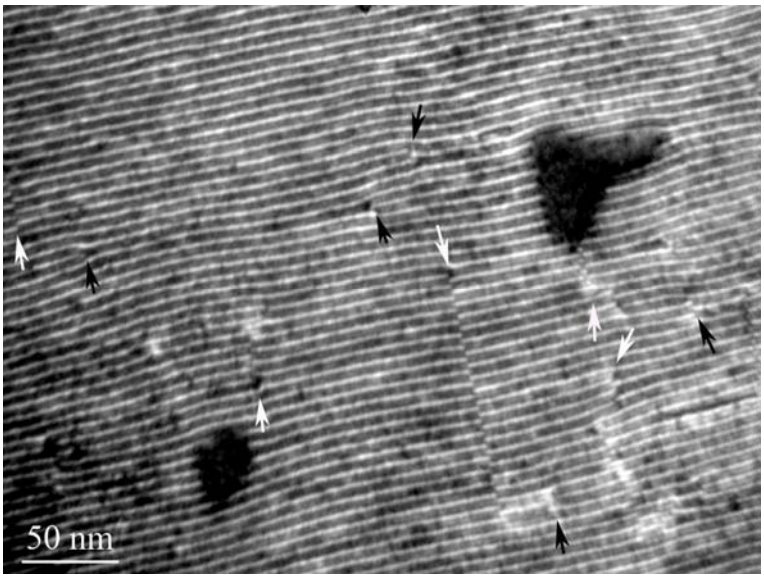

Figure 5. 1 The WBDF image of 27 ML GaSb on GaAs, two types of imperfection of the Lomer dislocation network are marked by the arrows: the shift (or mismatch) of the Lomer dislocations (red arrow) and the addition Lomer dislocation (green arrow).

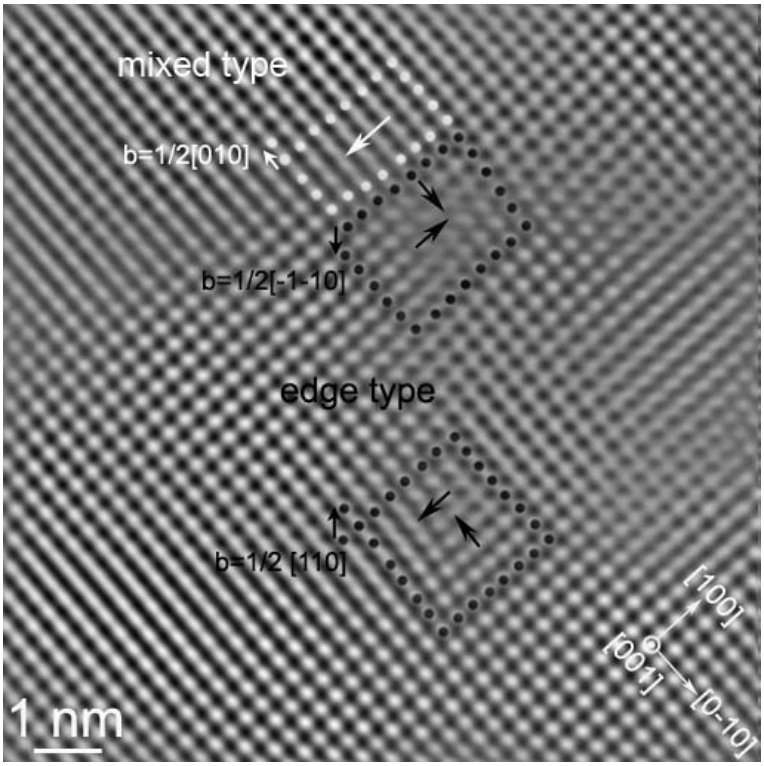

Figure 5. 2 The plan-view HRTEM image of GaSb with threading dislocations.

3. Regarding the MD simulation, at least one point is still unclear. As schematically shown in Fig. 5.3, the two sets of Lomer dislocation are periodically distributed at the interface, and each shuffle (glide) set Lomer dislocation is surrounded by 4 glide (shuffle) set Lomer dislocations. With this configuration, for the hetero-structure in the cross section we can only observe one set Lomer dislocation along one of the <110> direction and the other set is out of contrast. However, in the experimental observation we didn't see this configuration (both glide and shuffle set Lomer dislocations can be observed at [110] interface, Fig. 4.12). It should be interesting to reveal the reason of this discrepancy between the experimental observation and the simulation.

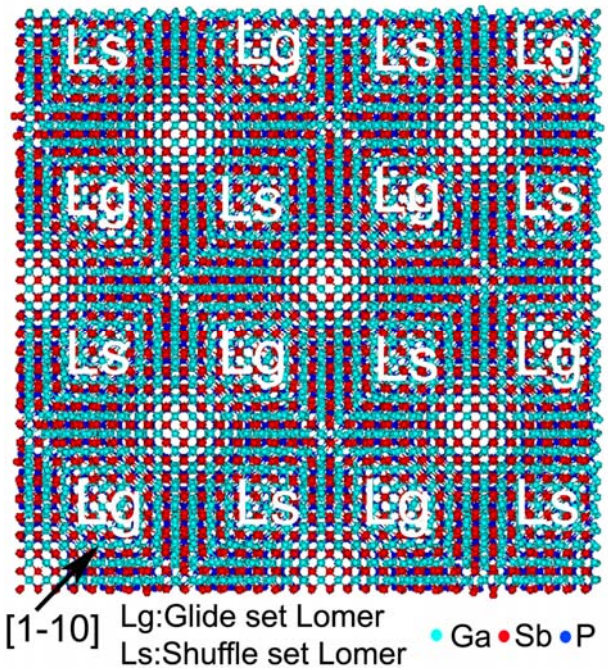

Figure 5. 3 The [001] projection of the GaSb(32a x32a)/GaP(36a x 36a) heterostructure shows the configuration of Lomer at the interface.

4. Is it reasonable to believe that all the mismatch strain can be confined in the interface for high mismatch systems? This work started with the assumption that the IMF proposal of the Huffaker's group needed to be systematically investigated with the aim of finding a reproducible growth process of hetero-structure with a minimum density of defects. With our proposed mechanism, it may not be possible to directly form the dislocation network at the interfaces. Indeed, as can be seen in Fig. 5.4, from Huffaker's group [7], their plan view micrograph of their "IMF" layers exhibit a high density of defects (threading dislocations). However, the declared low TD density (8.5 x 10^5 cm^{-2}) was obtained in 100 nm thick layers (Table 1.3). Therefore a good suggestion should be to continue this work by further investigating the TD density reduction versus the growth condition and layer thickness.

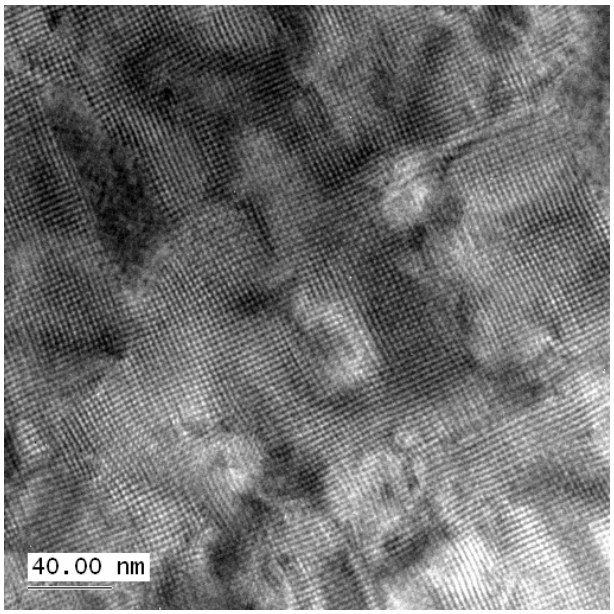

Figure 5.4 The moiré fringes of 54 ML GaSb on GaAs with IMF growth from Huang's PhD thesis [7].

References

[1]J. M. Kang, M. Nouaoura, L. Lassabatère, and A. Rocher, J. Cryst. Growth **143**, 115 (1994).

[2]A. Rocher and J. M. Kang, Microscopy of semiconducting Materials **146**, 135 (1995).

[3]J. G. Zhu and C. B. Carter, Philos. Mag. A **62**, 319 (1990).

[4]A. Rocher, M.-N. Charasse, B. Bartenlian, and J. Chazelas, Le Journal De Physique Colloques **51**, C1–915 (1990).

[5]P. Komninou, J. Stoemenos, G. P. Dimitrakopulos, and T. Karakostas, J. Appl. Phys. **75**, 143 (1994).

[6]H. Hojo, E. Tochigi, T. Mizoguchi, H. Ohta, N. Shibata, B. Feng, and Y. Ikuhara, Appl. Phys. Lett. **98**, 153104 (2011).

[7]S. Huang, *Microscopy Study of Extreme Lattice Mismatched Heteroepitaxy Using Interfacial Misfit Arrays*, The University of New Mexico, 2007.

Appendix I

As schematically shown in Fig. 1 (a), the dislocation being generated at the surface is submitted to the stress field generated by the dislocation already present at the interface as well as to that of the image dislocation outside the layer as given by Eq. 1:

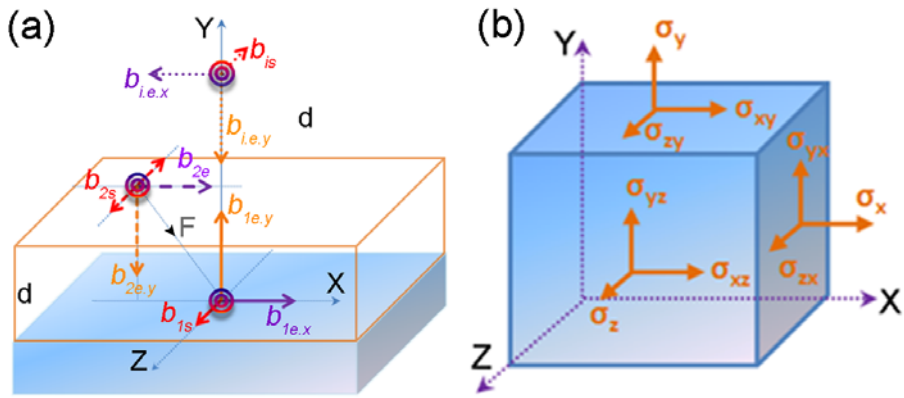

Figure 1 (a) The schematic arrangement of the 60° dislocations components. b_{1s}, $b_{1e.x}$, $b_{1e.y}$, b_{2s}, $b_{2e.x}$, and $b_{2e.y}$ being the screw, edge components of the first and second dislocations, respectively. $b_{i.s}$, $b_{i.e.x}$, and $b_{i.e.y}$ are the screw and edge components of the image dislocation. (b) The Stress components on the surface of a cube.

$$\sigma = \begin{pmatrix} {}^x\sigma_x & {}^x\sigma_{xy} & 0 \\ {}^x\sigma_{yx} & {}^x\sigma_y & 0 \\ 0 & 0 & {}^x\sigma_z \end{pmatrix}_{x.edge} + \begin{pmatrix} {}^y\sigma_x & {}^y\sigma_{xy} & 0 \\ {}^y\sigma_{yx} & {}^y\sigma_y & 0 \\ 0 & 0 & {}^y\sigma_z \end{pmatrix}_{y.edge} + \begin{pmatrix} 0 & 0 & {}^z\sigma_{xz} \\ 0 & 0 & {}^z\sigma_{yz} \\ {}^z\sigma_{zx} & {}^z\sigma_{zy} & 0 \end{pmatrix}_{screw}$$
$$+ \begin{pmatrix} {}^x\sigma'_x & {}^x\sigma'_{xy} & 0 \\ {}^x\sigma'_{yx} & {}^x\sigma'_y & 0 \\ 0 & 0 & {}^x\sigma'_z \end{pmatrix}_{image\ x.edge} + \begin{pmatrix} {}^y\sigma'_x & {}^y\sigma'_{xy} & 0 \\ {}^y\sigma'_{yx} & {}^y\sigma'_y & 0 \\ 0 & 0 & {}^y\sigma'_z \end{pmatrix}_{image\ y.edge} + \begin{pmatrix} 0 & 0 & {}^z\sigma'_{xz} \\ 0 & 0 & {}^z\sigma'_{yz} \\ {}^z\sigma'_{zx} & {}^z\sigma'_{zy} & 0 \end{pmatrix}_{image\ screw} \quad (1)$$

The six terms are the contribution of edge and screw components of the first dislocation, and edge and screw components of the image dislocation, respectively. And the stress field from the *x* axis edge component of the interface dislocation is given by Eq. (2 a):

$$
\begin{aligned}
{}^{x}\sigma_{x} &= \tau_o b_{e.x} \frac{y(3x^2+y^2)}{(x^2+y^2)^2} \\
{}^{x}\sigma_{y} &= -\tau_o b_{e.x} \frac{y(x^2-y^2)}{(x^2+y^2)^2} \\
{}^{x}\sigma_{xy} &= \tau_o b_{e.x} \frac{x(x^2-y^2)}{(x^2+y^2)^2} \\
{}^{x}\sigma_{z} &= \nu({}^{x}\sigma_{x}+{}^{x}\sigma_{y}) = \tau_o b_{e.x} \nu \frac{y(2x^2+y^2)}{(x^2+y^2)^2}
\end{aligned}
\qquad (2\text{ a})
$$

the stress field from the *y* axis edge component of the first dislocation is

$$
\begin{aligned}
{}^{y}\sigma_{x} &= -\tau_o b_{e.y} \frac{x(y^2-x^2)}{(y^2+x^2)^2} \\
{}^{y}\sigma_{y} &= \tau_o b_{e.y} \frac{x(3y^2+x^2)}{(y^2+x^2)^2} \\
{}^{y}\sigma_{xy} &= \tau_o b_{e.y} \frac{y(y^2-x^2)}{(y^2+x^2)^2} \\
{}^{y}\sigma_{z} &= \nu({}^{y}\sigma_{x}+{}^{y}\sigma_{y}) = \tau_o b_{e.y} \nu \frac{x(2y^2+x^2)}{(y^2+x^2)^2}
\end{aligned}
\qquad (2\text{ b})
$$

the stress field from the screw component of the first dislocation is

$$
\begin{aligned}
{}^{z}\sigma_{xz} &= -\frac{Gb_s}{2\pi}\frac{y}{x^2+y^2} \\
{}^{z}\sigma_{yz} &= \frac{Gb_s}{2\pi}\frac{x}{x^2+y^2}
\end{aligned}
\qquad (2\text{ c})
$$

the stress field from the *x* axis edge component of the image dislocation is

$$
\begin{aligned}
{}^{x}\sigma'_{x} &= \tau_o b_{i.e} \frac{(y-2d)[3x^2+(y-2d)^2]}{[x^2+(y-2d)^2]^2} \\
{}^{x}\sigma'_{y} &= -\tau_o b_{i.e} \frac{(y-2d)[x^2-(y-2d)^2]}{[x^2+(y-2d)^2]^2} \\
{}^{x}\sigma'_{xy} &= \tau_o b_{i.e} \frac{x[x^2-(y-2d)^2]}{[x^2+(y-2d)^2]^2} \\
{}^{x}\sigma'_{z} &= \nu({}^{x}\sigma'_{x}+{}^{x}\sigma'_{y}) = \tau_o b_{i.e} \nu \frac{(y-2d)[2x^2+(y-2d)^2]}{[x^2+(y-2d)^2]^2}
\end{aligned}
\qquad (2\text{ d})
$$

the stress field from the *y* axis edge component of the image dislocation is

$$
\begin{aligned}
{}^{y}\sigma'_{x} &= -\tau_o b_{i.e.y} \frac{x[(y-2d)^2 - x^2]}{[(y-2d)^2 + x^2]^2} \\
{}^{y}\sigma'_{y} &= \tau_o b_{i.e.y} \frac{x[3(y-2d)^2 + x^2]}{[(y-2d)^2 + x^2]^2} \\
{}^{y}\sigma'_{xy} &= \tau_o b_{i.e.y} \frac{(y-2d)[(y-2d)^2 - x^2]}{[(y-2d)^2 + x^2]^2} \\
{}^{y}\sigma'_{z} &= \nu({}^{y}\sigma'_{x} + {}^{y}\sigma'_{y}) = \tau_o b_{i.e.y} \nu \frac{x[2(y-2d)^2 + x^2]}{[(y-2d)^2 + x^2]^2}
\end{aligned}
\qquad (2\text{ e})
$$

and the stress field from its screw component is

$$
\begin{aligned}
{}^{z}\sigma'_{xz} &= -\frac{Gb_{i.s}}{2\pi} \frac{y-2d}{x^2 + (y-2d)^2} \\
{}^{z}\sigma'_{yz} &= \frac{Gb_{i.s}}{2\pi} \frac{x}{x^2 + (y-2d)^2}
\end{aligned}
\qquad (2\text{ f})
$$

where τ_o =G/2π(1-ν), G is the shear modulus, ν is the Poison's ratio.

We assume that the second 60° dislocation is on the free surface, and the thin film thickness is d, and that the second 60° dislocation has the same edge component as the first one, whereas the screw component is anti-parallel with that of the first 60° dislocation.

The force on the second dislocation in this stress field will be given by

$$f = (b \cdot \sigma_b) \times \xi \qquad (3)$$

where b is the Burgers vector, ξ is unit length of the dislocation along the dislocation line, and σ_b is the stress on the plane normal to the Burgers vector, and on which *b* points outwards [1].

We first calculate the force on the second 60° dislocation edge component, as the ξ_e is along z axis and the Burgers vector is along the x axis, the σ_b on the plane normal to the Burgers vector will be ${}^{x}\sigma_{x}$, ${}^{x}\sigma_{yx}$, ${}^{y}\sigma_{x}$, ${}^{y}\sigma_{yx}$, ${}^{z}\sigma_{zx}$, ${}^{x}\sigma'_{x}$, ${}^{x}\sigma'_{yx}$, ${}^{y}\sigma'_{x}$, ${}^{y}\sigma'_{yx}$ and ${}^{z}\sigma'_{zx}$. Then the force (per unit length of the dislocation) on the edge component can be expressed as:

$$
\begin{aligned}
f_{e.x} &= (b_{e.x} \cdot \sigma_b) \times \xi_e \\
&= |b_e|({}^x\sigma_x + {}^x\sigma_{yx} + {}^y\sigma_x + {}^y\sigma_{yx} + {}^x\sigma'_x + {}^x\sigma'_{yx} + {}^y\sigma'_x + {}^y\sigma'_{yx} + {}^z\sigma_{zx} + {}^z\sigma'_{zx}) \times \xi_e \qquad (4) \\
&= |b_e|({}^x\sigma_x + {}^y\sigma_x + {}^x\sigma'_x + {}^y\sigma'_x) \times \xi_e + |b_e|({}^x\sigma_{yx} + {}^y\sigma_{yx} + {}^x\sigma'_{yx} + {}^y\sigma'_{yx}) \times \xi_e
\end{aligned}
$$

Combining Eq. (2a), (2b), (2d), (2e) and (4) gives

$$
\begin{aligned}
f_{e.x} = |b_{e.x}|\{&\tau_o b_{e.x} \frac{y(3x^2+y^2)}{(x^2+y^2)^2} + \tau_o b_{i.e.x} \frac{(y-2d)[3x^2+(y-2d)^2]}{[x^2+(y-2d)^2]^2} \\
&- \tau_o b_{e.y} \frac{x(y^2-x^2)}{(y^2+x^2)^2} - \tau_o b_{i.e.y} \frac{x[(y-2d)^2-x^2]}{[(y-2d)^2+x^2]^2}\}u_y \\
&+ |b_{e.x}|\{\tau_o b_{e.x} \frac{x(x^2-y^2)}{(x^2+y^2)^2} + \tau_o b_{i.e.x} \frac{x[x^2-(y-2d)^2]}{[x^2+(y-2d)^2]^2} \qquad (5) \\
&+ \tau_o b_{e.y} \frac{y(y^2-x^2)}{(y^2+x^2)^2} + \tau_o b_{i.e.y} \frac{(y-2d)[(y-2d)^2-x^2]}{[(y-2d)^2+x^2]^2}\}u_x \\
= 2|b_{e.x}|\{&\tau_o b_{e.x} \frac{d(3x^2+d^2)}{(x^2+d^2)^2} u_y + \tau_o b_{e.y} \frac{d(d^2-x^2)}{(d^2+x^2)^2} u_x\}
\end{aligned}
$$

the force on the y axis edge component, the ξ_e is along z axis and burger vector is along z axis, the σ_b will be ${}^x\sigma_y$, ${}^x\sigma_{xy}$, ${}^y\sigma_y$, ${}^y\sigma_{xy}$, ${}^z\sigma_{zy}$, ${}^x\sigma'_y$, ${}^x\sigma'_{xy}$, ${}^y\sigma'_y$, ${}^y\sigma'_{xy}$ and ${}^z\sigma'_{zy}$. Then the force (per unit length of the dislocation) on the edge component can be expressed as:

$$
\begin{aligned}
f_{e.y} &= (b_{e.y} \cdot \sigma_b) \times \xi_e \\
&= |b_{e.y}|({}^x\sigma_y + {}^x\sigma_{xy} + {}^y\sigma_y + {}^y\sigma_{xy} + {}^x\sigma'_y + {}^x\sigma'_{xy} + {}^y\sigma'_y + {}^y\sigma'_{xy} + {}^z\sigma_{zy} + {}^z\sigma'_{zy}) \times \xi_e \qquad (6) \\
&= |b_{e.y}|({}^x\sigma_y + {}^y\sigma_y + {}^x\sigma'_y + {}^y\sigma'_y) \times \xi_e + |b_e|({}^x\sigma_{xy} + {}^y\sigma_{xy} + {}^x\sigma'_{xy} + {}^y\sigma'_{xy}) \times \xi_e
\end{aligned}
$$

Combining Eq. (2a), (2b), (2d), (2e), and (6) gives

$$
\begin{aligned}
f_{e.y} = |b_{e.y}|\{&-\tau_o b_{e.x} \frac{y(x^2-y^2)}{(x^2+y^2)^2} - \tau_o b_{i.e.x} \frac{(y-2d)[x^2-(y-2d)^2]}{[x^2+(y-2d)^2]^2} \\
&+ \tau_o b_{e.y} \frac{x(3y^2+x^2)}{(y^2+x^2)^2} + \tau_o b_{i.e.y} \frac{x[3(y-2d)^2+x^2]}{[(y-2d)^2+x^2]^2}\}u_x \\
&+ |b_{e.y}|\{\tau_o b_{e.x} \frac{x(x^2-y^2)}{(x^2+y^2)^2} + \tau_o b_{i.e.x} \frac{x[x^2-(y-2d)^2]}{[x^2+(y-2d)^2]^2} \qquad (7) \\
&+ \tau_o b_{e.y} \frac{y(y^2-x^2)}{(y^2+x^2)^2} + \tau_o b_{i.e.y} \frac{(y-2d)[(y-2d)^2-x^2]}{[(y-2d)^2+x^2]^2}\}u_y \\
= 2|b_{e.y}|\{&-\tau_o b_{e.x} \frac{d(x^2-d^2)}{(x^2+d^2)^2} u_x + \tau_o b_{e.y} \frac{d(d^2-x^2)}{(d^2+x^2)^2} u_y\}
\end{aligned}
$$

And the force on the screw component, the ξ_s is along z axis and burger vector of the screw component is along z axis, the σ_b will be σ_{xz}, σ_{yz}, σ_z, σ'_{xz}, σ'_{yz}, and σ'_z. The force (per unit length of the dislocation) on the screw component can be expressed as:

$$\begin{aligned} f_s &= |b_s|\sigma_b \times \xi_s \\ &= |b_s|(\sigma_{xz} + \sigma_{yz} + \sigma'_{xz} + \sigma'_{yz} + \sigma_z + \sigma'_z) \times \xi_s \qquad (8) \\ &= |b_s|(\sigma_{xz} + \sigma'_{xz}) \times \xi_s + |b_s|(\sigma_{yz} + \sigma'_{yz}) \times \xi_s \end{aligned}$$

Combining Eq. (4.2 b), (4.2 c) and (4.6) gives

$$f_s = |b_s|(\frac{Gb_s}{2\pi}\frac{y}{x^2+y^2} + \frac{Gb_{i.s}}{2\pi}\frac{y-2d}{x^2+(y-2d)^2})u_y + |b_s|[-\frac{Gb_s}{2\pi}\frac{x}{x^2+y^2} - \frac{Gb_{i.s}}{2\pi}\frac{x}{x^2+(y-2d)^2}]u_x \quad (9)$$

For FCC structure, the dislocation slip along {111} plane at α =54.736^o to the interface (or surface) plane, we consider the simplest situation: y=d and $x = d \cdot \cot\alpha$. Then the Eq. (5) and (7) yield

$$f_{e.x} = \frac{2b_{e.x}\tau_o d}{(x^2+d^2)^2}[b_{e.x}(3x^2+d^2)u_y + b_{e.y}(d^2-x^2)u_x\} = \frac{2b^2{}_{e.x}\tau_o d^3}{(x^2+d^2)^2}(2.5u_y + 0.707u_x) \qquad (10)$$

$$f_{e.y} = \frac{2b_{e.y}\tau_o d}{(x^2+d^2)^2}[b_{e.y}(d^2+x^2)u_y - b_{e.x}(x^2-d^2)u_x\} = \frac{2b^2{}_{e.x}\tau_o d^3}{(x^2+d^2)^2}(3u_y + 0.707u_x) \qquad (11)$$

$$f_s = 2b_s{}^2\frac{G}{2\pi}\cdot\frac{d}{(d\cot\alpha)^2+d^2}u_y = \frac{Gb_s{}^2}{\pi}\cdot\frac{1}{\cot^2\alpha+1}\cdot\frac{1}{d}u_y \qquad (12)$$

For GaSb, we take G=2.41x10^{10} N/m^2 and ν =0.31 [2], then

$$f_{e.x} = \frac{506.15}{d}dyn/cm, \quad f_{e.y} = \frac{600.29}{d}dyn/cm, \quad f_s = \frac{204.67}{d}dyn/cm,$$

where the unit of d is nm.

References

[1]J. P. Hirth and J. Lothe, *Theory of Dislocations* (Krieger Pub. Co., 1982).

[2]S. Adachi, *Properties of Group-IV, III-V and II-VI Semiconductors*, 1st ed. (Wiley, 2005).

Appendix II

(1) Publications

1. **Y. Wang**, P.Ruterana, S.Kret, J.Chen,L.Desplanque,S.El Kazzi, X.Wallart. Mechanism of formation of the misfit dislocations at the cubic materials interfaces, *Appl. Phys. Lett.* (Proof corrected)
2. **Y. Wang**, P.Ruterana, L.Desplanque,S.El Kazzi, X.Wallart. Growth mode dependence of misfit dislocation configuration at lattice mismatched III-V semiconductor interfaces, *Europhys. Lett.* 97, 68011(2012)
3. **Y. Wang**, P.Ruterana, H.P.Lei, J.Chen, S.Kret, S.El Kazzi, L.Desplanque, X.Wallart. Investigation of the anisotropic strain relaxation in GaSb island on GaP, *J.Appl.Phys.*110, 043509 (2011)
4. **Y. Wang**, P.Ruterana, L.Desplanque, S.El Kazzi, X.Wallart, Strain relief at GaSb/GaAs interface versus substrate surface treatment and AlSb interlayers thickness, *J.Appl.Phys.*109, 023509 (2011)
5. **Y. Wang**, H.Wang, C.Ye, J.Zhang, H.B.Wang, Y.Jiang, Interfacial reaction and electrical properties of HfO_2 film gate dielectric prepared by pulse laser deposition in nitrogen-Role of rapid thermal annealing and gate electrode, *ACS App. Mater. Interfaces* 3, 3813 (2011)
6. **Y. Wang**, P.Ruterana, L.Desplanque, S.El Kazzi, X.Wallart. Transmission electron microscopy of misfit dislocation and strain relaxation in lattice mismatched III-V heterostructures versus substrate surface treatment, *MRS Proceedings*, mrss11-1324-d13-04, 1324 (2011)
7. L.Desplanque, S.El Kazzi, J.L.Codron **Y.Wang**, P.Ruterana, G. Moschetti, J.V.Grahn, X.Wallart, AlSb nucleation induced anisotropic electron mobility in AlSb/InAs heterostructure on GaAs, *Appl. Phys. Lett.* 100, 262103(2012)
8. S.El Kazzi, L.Desplanque, X.Wallart, **Y.Wang**, P.Ruterana, X.Wallart, Interplay between Sb flux and growth temperature during the formation of GaSb islands on GaP, *J.Appl.Phys.*111, 123506 (2012)
9. S.El Kazzi, L.Desplanque, C.Coinon, **Y.Wang**, P.Ruterana, X.Wallart. Compliance at the GaSb/GaP interface by misfit dislocations array, *Adv.Mat.Res.* 32, 85 (2011)
10. S.El Kazzi, L.Desplanque, C.Coinon, **Y.Wang**, P.Ruterana, X.Wallart. GaSb/GaP compliant interface for high electron mobility AlSb/InAs heterostructures on (001)GaP, *Appl. Phys. Lett.* 97, 192111(2010)
11. A.Olivier, N.Wichmann, J.J.Mo, A.Noudeviwa, Y.Roelens, L.Desplanque, X.Wallart, F.Danneville, G.Dambrine, J.Sanit-Martin, M.Shi, **Y. Wang**, M.P.Chauvat, P.Ruterana, H.Maher, Fabrication and characterization of 200 nm self-aligned In0.53Ga0.47As MOSFET *Indium Phosphide & Related Materials (IPRM)* DOI:10.1109/ICIPRM.2010.5515926
12. **Y. Wang**, H.Wang, J.Zhang, H.B.Wang, C.Ye, Y.Jiang, Q.Wang. Crystallization and interface control of HfO_2 films prepared by pulse laser deposition using in situ ionized nitrogen, *Appl. Phys. Lett.* 95, 032905(2009)
13. C.Ye, **Y. Wang**, J.Zhang, J.Q.Zhang, H.Wang, and Y.Jiang, Evidence of interface conversion and electrical characteristics improvement of ultra-thin HfTiO films upon rapid thermal annealing, *Appl. Phys. Lett.* 99, 182904 (2011)
14. C.Ye, **Y. Wang**, Y.Ye, J.Zhang, G.H.Li. Preparation and photoluminescence of undoped $ZnTiO_3$ thin films, *J.Appl.Phys.*106, 033520(2009)
15. H.Wang, **Y. Wang**, C. Ye, J. Feng, B.Y. Wang, H.B.Wang, Q. Li, Y. Jiang. Interface control and leakage current conduction mechanism in HfO_2 films prepared by pulsed laser deposition, *Appl. Phys. Lett.* 93, 202904(2008)
16. H.Wang, **Y. Wang**, J. Feng, C. Ye, B.Y. Wang, Q. Li, Y. Jiang, A.P. Huang, Z.S. Xiao. Structure and electrical properties of HfO_2 high-k films prepared by pulsed laser deposition on Si(100), *Appl. Phys. A.* 93, 681(2008)

17. J.X.Duan, H.Wang, H.B.Wang, J.Zhang,S.Wu, **Y. Wang**, Mn-doped ZnO nanotubes: from facile solution synthesis to room temperature ferromagnetism, *CrystEngComm* 14,1330 (2012)
18. M.Dong, H.Wang, C.Ye, L.Shen, **Y. Wang**, J.Zhang, Y.Ye, Structure and electrical properties of sputtered ZrO_2/TiO_2 bilayer composite dielectrics upon annealing in nitrogen, *Nanoscale Res.Lett.* 7, 31 (2012)
19. M.Dong, H.Wang, L.Shen,Y.Ye, C.Ye,**Y. Wang**, J.Zhang, Y.Jiang, Dielectric property and electrical conduction mechanism of ZrO_2-TiO_2 composite thin films, *J.Mater.Sci.:Mater. Electron.* 23, 174 (2012)
20. H.B.Wang, H.Wang,J.Zhang,F.J.Yang,**Y. Wang**,J.Wang,M.J.Zhou,Q.Li, Formation and magnetic properties of a large-scale FePt nanoparticale monolayer on silicon substrate, *Physica Scripta,* T139, 014071 (2010)
21. C.Ye, H.Wang,J.Zhang,Y.Ye,**Y. Wang**, B.Y.Wang, Y.Jin, Composition dependence of band alignment and dielectric constant for $Hf_{1-x}Ti_xO_2$ thin films on Si (100), *J.Appl.Phys.*107,104103(2010)
22. B.Y.Wang, H.Wang, C.Ye, **Y. Wang**, Y.Ye, W.F.Wang, Effect of a silicon nitride buffer layer on the electrical properties of tantalum pentoxide films, *Microelectronic Engineering,* **87**, 597(2010)
23. H.B.Wang,M.J.Zhou,F.J.Yang,J.Wang,Y.Jiang,**Y. Wang**,H.Wao,Monolayer assembly and fixation of FePt nanoparticles: microstructure and magnetic properties, *Chem.Mater.* 21,404(2009)
24. H.Wang, Z.P.Zhang, X.N.Wang, Q.Mo, **Y. Wang**, J.H.Zhu, H.B.Wang, F.J.Yang, Y.Jiang，Selective Growth of Vertical- aligned ZnO Nanorod Arrays on Si Substrate by Catalyst-free Thermal Evaporation, *Nanoscale Res. Lett.* 3,309(2008)
25. F.J.Yang, H.Wang, J.Zhang, **Y. Wang**, H.B.Wang, J.H.Zhu, Q.Li, Y.Jiang, Influence of silicides formation on microstructure and magnetic properties, *J.Phys.D.* 41, 235003(2008)

(2) Conferences

1. **Y. Wang**, P.Ruterana,S.Kret, J. Chen, L.Desplanque,S.El Kazzi, X.Wallart. The atomic structure and formation mechanism of misfit dislocations by HAADF investigation, PICO 2012, Julich, Germany, 1st March 2012 (**Poster**)
2. **Y. Wang**, P.Ruterana, H.P.Lei, J.Chen, S.Kret, S.El Kazzi, L.Desplanque, X.Wallart. TEM and molecular dynamics simulation investigation of the anisotropic strain relaxation in GaSb islands on GaP, EMRS 2011 Spring conference, Nice, France, 10th May 2011 (**Poster**)
3. **Y. Wang**, P.Ruterana, L.Desplanque, S.El Kazzi, X.Wallart. Misfit dislocation and strain relaxation at GaSb/GaAs interface versus substrate surface treatment, Symposium D, MRS 2011 Spring conference San Francisco, 27th April 2011 (**Oral**)
3. **Y. Wang**, P.Ruterana, L.Desplanque, S.El Kazzi, X.Wallart. TEM analysis of the dislocation mechanism in III-V Heterostructures grown by molecular beam epitaxy, Symposium RR, MRS 2011 Spring conference, San Francisco, 26th April 2011 (**Oral**)
4. **Y. Wang**, P.Ruterana, L.Desplanque, S.El Kazzi, X.Wallart. The structure of dislocations in metamorphic III-V heterostructures grown by MBE, EMRS 2010 Spring meeting, Symposium Q, Strasbourg, France, 8th June 2010 (**Poster**)
5. S.El Kazzi, L.Desplanque, C.Coinon, **Y. Wang**, P.Ruterana, X.Wallart. Influence of Sb overpressure on the anisotropic transport properties of InAs/AlSb heterostructures grown on highly mismatched substrates, MRS 2012 Spring conference San Francisco, 26th April 2012 (**Oral**)
6. S.El Kazzi, L.Desplanque, C.Coinon, **Y. Wang**, P.Ruterana, X.Wallart. Strain relaxation of GaSb islands on GaP and GaAs substrates for high mobility AlSb/InAs heterostructurese, The 20th European workshop on Hetrostructure Technology, Lille, November 2011(**Oral**)
7. L.Desplanque, S.El Kazzi, C.Coinon, **Y. Wang**, P.Ruterana, X.Wallart. Lattice mismatch accommodation at GaSb/GaAs and GaSb/GaP interfaces, 16th European Molecular Beam Epitaxy Workshop, Grenoble, France, 20th -23rd March 2011 (**Oral**)

8. S.El Kazzi, L.Desplanque, C.Coinon, **Y. Wang**, P.Ruterana, X.Wallart. Strain relaxation by misfit dislocation array at the GaSb/GaP, 16th International conference on Molecular Beam Epitaxy, Berlin, Germany 22nd -27th August 2010(**Oral**)

(3) Seminars

1. **Y. Wang**, Characterization of core structure and Burgers vector of GaSb/GaAs misfit dislocation by HAADF-STEM and molecular dynamic simulation, Electron Microscopy Group, University of Erlangen-Nürnberg, Erlangen, Germany, 2nd April 2012
2. **Y. Wang**, The atomic structure and formation mechanism of misfit dislocations at GaSb/GaAs interface, CEMES-CNRS, Toulouse, France, 10th May 2012
3. **Y. Wang**, TEM analysis of misfit dislocation and strain relaxation at III-V heterostructure interfaces, Plasma & Coating Physics Division, Linköping University, Linköping, Sewden, 24th May 2012

Dislocation et relaxation des contraintes aux interfaces entre semiconducteurs III-V à large différence de paramètres de maille

Résumé :

Au cours de ce travail, nous avons procédé à une analyse extensive des dislocations d'interface et de la relaxation des contraintes dans les couches épitaxiales de GaSb sur GaAs (ou GaP) par microscopie électronique en transmission. Sur le substrat de GaAs, nous avons étudié le rôle de l'épaisseur de couches intermédiaires AlSb et le traitement de surface du substrat sur la relaxation des contraintes et la densité de dislocations émergeantes de la couche GaSb. Pareillement, nous avons étudié les effets des paramètres de croissance, tels que, le traitement de surface du substrat, la vitesse et la température de croissance sur la relaxation des contraintes des premières monocouches de GaSb sur la GaP. Avec ces paramètres de croissance optimisés, nous avons pu réaliser une couche de GaSb tampon (600 nm) et des hétéro-structures AlSb/InAs avec une mobilité température ambiante de 30000 $cm^2V^{-1}s^{-1}$ et 25500 $cm^2V^{-1}s^{-1}$ sur la GaAs et GaP, respectivement. De plus nous avons mis en évidence, une dépendance du type de dislocation d'interface au mode de croissance: une croissance 2D de GaSb favorise la génération de dislocations de Lomer; alors que des dislocations 60° et des paires de 60° sont principalement générées en mode de croissance 3D. Nous avons aussi déterminé de façon quantitative le mécanisme général de formation des dislocations d'interface: l'interaction d'une dislocation 60° qui se forme en surface et glisse sous interaction avec celle qui se trouve déjà dans l'interface, mais aussi la tension de surface, permettent de déterminer la direction de son vecteur de Burger et donc la configuration de la dislocation résultante à l'interface. Les structures des dislocations et leur stabilité ont été étudiées par HAADF avec résolution atomique et modélisation par dynamique moléculaire. L'étude quantitative des vecteurs de Burger par analyse fine des images a confirmé le mécanisme de formation des dislocations d'interface en accord avec notre modèle.
Mots clés: dislocations dans les semiconducteurs; relaxation des contraintes; microscope électronique à transmission; épitaxie par faisceaux moléculaires; composés semiconducteurs

Misfit dislocation and strain relaxation at large lattice mismatched III-V semiconductor interfaces

Abstract:

In this work, we have carried out an extensive TEM investigation of misfit dislocations and strain relaxation in Sb-based III-V epitaxial layers on the GaAs and GaP substrates. On GaAs, we have investigated the influence of AlSb interlayer thickness and substrate surface treatment on the strain relaxation and threading dislocation density inside GaSb layers. Similarly, we studied the growth parameters, such as substrate surface treatment, growth rate, and growth temperature on the strain relaxation of 10 MLs GaSb on GaP. With the optimized GaSb buffer layers (600 nm), high mobility AlSb/InAs hetero-structures with room temperature mobility of 30000 $cm^2V^{-1}s^{-1}$ (25500 $cm^2V^{-1}s^{-1}$) on GaAs (GaP) substrates have been achieved. A growth mode dependence of the misfit dislocation has been observed: a 2D growth of GaSb promotes the generation of Lomer dislocations; in contrast 60° dislocations and closely spaced 60° pairs are predominantly generated in 3D growth mode. Consequently, a 60° dislocation glide model in combination with surface effects is able to account for the formation of Lomer, 60°, and 60° dislocation pairs at these hetero-interfaces. The core structures of the misfit dislocations and their stability have been investigated by atomic resolution HAADF and molecular dynamic simulation. The dislocation density tensor analysis was next used to quantify the burgers vector of the misfit dislocations. This precise measurement revealed the misfit dislocation formation mechanism in agreement with our proposed model.

Key words: misfit dislocation; strain relaxation; Transmission electron microscopy; Molecular beam epitaxy; III-V Antimonides semiconductors